Multi-scale and multi-parametric analysis of Late Quaternary event deposits within the active Corinth Rift (Greece)

Gino De Gelder[1,2], Mai Linh Doan[2], Christian Beck[3], Julie Carlut[1], Chloé Seibert[1], Nathalie Feuillet[1], Gareth D.O. Carter[4], Sofia Pechlivanidou[5], Robert L. Gawthorpe[5]

1) Institut de Physique du Globe de Paris, Paris, France.
2) Institut des Sciences de la Terre, Université Grenoble Alpes, France.
3) Institut des Sciences de la Terre, Université Savoie-Mont-Blanc, Le Bourget du Lac. France
4) British Geological Survey, The Lyell Centre, United Kingdom.
5) Department of Earth Science, University of Bergen, Norway.

Keywords : turbidites, homogenites, gravity reworking, microtomography, Corinth Rift; IODP Expedition 381

A major challenge in subaqueous paleoseismology is to understand the relationship between an earthquake/tsunami and a sedimentary event deposit recorded in drillcores. Expedition 381 of the International Ocean Discovery Program was dedicated to understanding the development of the Corinth Rift, Greece. Its drilled cores provide a potentially important resource to better understand depositional mechanisms of sedimentary event deposits within changing open marine to (semi-)isolated environments. To achieve this, we analyse U-channels and spatula samples from the topmost part (0-65 m below seafloor maximum depth) of holes M0078B and M0079A (~0-25 ka), using high-resolution X-Ray microtomography in combination with grain-size, magnetic and XRF measurements. Structures and grain fabric are resolved down to 10 μm in voxel size, characterizing the geometry of the basal surface of turbidite+homogenite sedimentary event deposits, and the internal base-upwards evolution at high-resolution scale. Our analysis suggests these types of deposits are more complex than previously proposed, especially at the transition between the basal coarse turbidite sub-unit and the fine-grained homogenite upper sub-unit, as well as within the homogenite. Combined with the other observations and parameters, X-ray microtomography results are consistent with the interpretation of the Corinth turbidite+homogenite deposits as having predominantly originated from seismic and/or aseismic slope failures followed by tsunami/seiche effects, despite subtle differences according to depositional environment.

1-Introduction

Over previous decades, the discipline of "subaqueous paleoseismology" developed with the aim of contributing efficiently to earthquake hazard assessment (e.g. McCalpin,

2009). This approach needs to build on a tripartite relationship between 1) a sedimentary event deposit 2) an earthquake with or without an associated tsunami wave, and 3) an identified active fault, with possibly a known rupture location. These elements have been analysed, event-by-event, for sedimentary records (either marine or lacustrine) that span as much as tens of thousands of years (e.g. Marco and Agnon, 1995; Rodriguez-Pascua et al., 2000), with correlations established between several different sites (e.g. McHugh et al. 2006; Goldfinger et al., 2007; Gràcia et al., 2010; Polonia et al., 2013, 2017; Ratzov et al., 2015). Establishing relationships between element 3) and the two other elements, requires precise knowledge of a fault system's activity, and of the sedimentary fill adjacent to the fault (e.g. McHugh et al., 2014; Beck et al, 2012, 2015; Vanneste et al., 2018; Van Daele et al., 2019).

In this study we focus on the relationship between elements 1) and 2), to understand better how sedimentary event deposits may be linked to earthquakes and/or tsunami waves. To achieve this, we benefit from the recent drilling and coring surveys conducted in the active Corinth Rift (Greece), within the framework provided by the 2017 International Ocean Discovery Program (IODP) Expedition 381 (McNeill et al., 2019a,b; Fig. 1). During this expedition, three primary holes were drilled at three sites (Fig. 1). Borehole M0078A reached a depth of 610.43 metres below seafloor (m b.s.f.) in water depths of approx. 860 m below sea level (m b.s.l.), borehole M0079A terminated at 704.9 m b.s.f. in water depths of approx. 857 m b.s.l., and borehole M0080A penetrated to 534.1 m b.s.f. in water depths of approx. 349 m b.s.l. An additional short hole was drilled at Site M0078, located approximately 20 m south of borehole M0078A, in order to better capture the sediment-water interface and shallow subsurface stratigraphy. This borehole, M0078B, recovered sediments to a depth of 55.85 m b.s.f.

The Corinth Rift benefits from a large amount of onshore and offshore surveys and monitoring (seismology, GPS kinematics, drilling, geophysical imagery, and numerical modelling) (e.g. Armijo et al, 1996; Rigo et al. 1996; Briole et al, 2000; Collier et al., 2000; Cornet et al., 2004; Pantosti et al., 2004; Koukouvelas et al., 2005; Leeder et al., 2005; Bernard et al. 2006; McNeill et al., 2007; Bell et al., 2009, 2011; Jolivet et al., 2010; Taylor et al., 2011; Pérouse et al. 2012; Pechlivanidou et al., 2019; De Gelder et al., 2019; Fernández-Blanco et al., 2019a,b). They are dedicated to both surface impacts of active tectonics and crustal scale fault-mechanics. Offshore surveys focused on sedimentary reworking phenomena and their possible relationships with active tectonics and seismicity (e.g. Ferentinos et al., 1988; Papatheodorou and Ferentinos, 1997; Papadopoulos, 2003; Lemeille et al., 2004, Moretti et al., 2004; Stefatos et al., 2006; Campos et al., 2013a; Campos, 2014;

Beckers et al., 2017, 2018). Initial development of the Corinth Rift started ~5 Ma (e.g. Gawthorpe et al., 2018), with the modern Corinth Rift forming around 0.6-2 Ma (e.g. Nixon et al., 2016; Gawthorpe et al., 2018; Fernandez-Blanco et al., 2019a). The modern Corinth Rift is essentially a half-graben, with its active bounding faults near the southern margin (Corinth Rift Fault System; Fig. 1). Historical records include ~100 >5.5 Ms earthquakes in the Corinth Rift over the past ~2500 years (Papazachos et al., 2000), with instrumentally recorded earthquakes mostly located in the W and E sections of the rift (focal mechanisms in Fig. 1). Comparison of event deposits and historical earthquakes in the W rift suggest that the basin floor provides the highest potential to record imprints of earthquakes/tsunamis in its sediments, although also non-earthquake triggered landslides may result in sedimentary event deposits (Beckers et al., 2017). The historical paleotsunami record also dates back ~2500 years (e.g. Papadopoulos, 2000), and includes tsunamis from both seismically and non-seismically induced landslides (e.g. Galanopoulos et al., 1964). Several studies have focused on the sedimentary tsunami record in coastal areas (e.g. Kontopoulos and Avramidis, 2003; Kortekaas et al., 2011, Vött et al., 2018), but it was also proposed that tsunamis/seiche waves are (partly) responsible for sedimentary event deposits on the Central Basin floor (Campos et al., 2013a; Beckers et al., 2017).

Effects of Late Quaternary climatic cycles on the bounding topographic relief also impacted the rift sedimentary infilling (Watkins et al., 2019; Pallikarakis et al., 2019). The offshore stratigraphy is strongly influenced by the sills at the western tip of the Gulf of Corinth (Rion sill: ~60 m b.s.l., Fig. 1; and the ~50-55 m b.s.l. Acheloos-Cape Pappas sill further west). Quaternary relative sea-level changes on the order of ~120 m (De Gelder et al., 2020) resulted in marine conditions during interglacial periods like the Holocene, and (semi-)isolated (SI) conditions, resembling a lacustrine setting, during glacial periods (McNeill et al., 2019b). As seismic reflection profiles image the lowstand of the last glacial ~70 m below the present sea-level (Collier et al., 2000), the water depth in the Central Basin floor, where the IODP-381 cores were drilled, varied between ~860 m and ~790 m over the past ~25 ka. In terms of sedimentation, comparison between marine phases of deposition (e.g. interval ~13 ka-present) and (semi-)isolated (SI) phases of deposition (e.g. interval ~70-13 ka) indicate sedimentation rates are generally lower, and bioturbation and organic carbon concentration higher, during marine intervals (Campos et al., 2013a; McNeill et al., 2019a and b).

Previous studies on sediments cored within the Corinth Rift infill, documented the interlayering of numerous "event deposits" – rapidly deposited layers related to earthquakes, tsunamis/seiches, (subaqueous) landslides and/or river floods– within a fine-grained

hemipelagic slow and continuously deposited background sedimentation, both during marine and SI episodes (Campos et al., 2013a, 2014). These event deposits are generally composed of a coarse basal sub-unit and a fine-grained upper one, and often described as "turbidites". Nevertheless, they are not necessarily related to gravity reworking, and a wide range of origins, and of single *vs.* complex depositional mechanisms, has to be considered. To better constrain the origins and mechanisms of these sedimentary event deposits in the Corinth Rift, and check the possible influence of the environment, we investigated the last marine/SI alternation (~25 ka; Fig. 2). We particularly focused on the limit between coarse basal and upper fine-grained sub-units, and used a multi-parametric approach including high-resolution X-Ray tomography, in combination with grainsize, magnetic and XRF measurements.

2-Data acquisition and processing

Observations and measurements discussed in this section are based on 1) part of the observations and analyses performed by the whole IODP Expedition 381 science team in the MARUM (University of Bremen) during the Onshore Science Party (OSP; February 2018; McNeill et al., 2019a), and 2) processing of specific selected post-cruise samples (Fig. 2). Specifically, we sampled 8 U-Channels from the cores of Holes M0078B and M0079A located at sites M0078 and M0079 respectively (Fig. 1) and 8 intervals with spatula samples, half from the most recent marine interval (~13-0 ka) and half from the upper portion of the most recent SI interval (~25-13 ka). In total, these samples comprise 8 event deposits from the marine interval, and 10 from the SI interval.

We illustrate and describe our results using representative U-channels 4 and 6 (Fig. 2), with results from the other U-Channels and spatula samples are presented in the Supplementary Material. Preliminary results of the whole OSP and raw data of IODP Expedition 381 (Expedition Report) are accessible on http://www.ecord.org/expedition381/.

2-1- Non destructive analyses

2-1-1- Volume magnetic susceptibility (**MS**).

To constrain MS within sedimentary event deposits we used two sets of measurements; 1) part of the initial IODP MSCL GEOTEK™ core logging data (MARUM, University of Bremen) recorded on the whole cores at 2 cm resolution, and 2) 0.5 cm resolution measurements made on U-channels using a BARTINGTON™ MS2 contact sensor (ISTerre Laboratory, Savoie-Mont-Blanc University).

2-1-2- X-ray fluorescence (XRF)

To decipher the chemical composition of sedimentary event deposits, also in comparison to the hemipelagic "background" sedimentation, we used two sets of XRF measurements (AVAATEC^{TM} device): 1) whole-core measurements with 5 mm spacing obtained using the XRF-scanner in MARUM (University of Bremen) on the intervals of the undisturbed half of the split cores corresponding to all U-channels, and 2) high resolution profiles (1 mm spacing) performed in EDYTEM Laboratory (Savoie-Mont-Blanc University) on four of the retrieved U-Channels.

As XRF analysis does not provide absolute chemical compositions, but relative activity of concerned elements, we used ratios of selected elements to characterize variations in sediment compositions, following Croudace et al. (2006). We specifically selected 24 ratios from the overview of Rothwell and Croudace (2015) that may indicate changes in 1) biogenic/detrital sedimentation, 2) sedimentary provenance, and grainsize, 3) productivity and post-depositional alteration, and 4) organic content. As most of the source areas for the Gulf of Corinth deposits are carbonate dominated, Ca ratios need to be carefully interpreted. We applied Principal Component Analysis (PCA) to these ratios in order to determine: i) the relative importance of different principal components to the overall variation in XRF values, and ii) the specific XRF ratios responsible for most significant changes within a principal component (Supplementary Fig. 1). We show only these most important elemental ratios within the results section, i.e. those with the highest relative contributions to principal components.

2-1-3- Anisotropy of Magnetic Susceptibility (AMS).

To measure AMS within the U-channels we extracted juxtaposed, 2 cm-side, oriented cubes of sediments and measured those using an AGICO^{TM} MFK1-FA Kappabridge (automatic spinning, 64 orientations per sample) at the Institut de Physique du Globe de Paris. Following the classification of Jelinek (1981) we consider the following parameters: foliation, lineation, shape parameter T, corrected anisotropy degree Pj, inclination of Kmin ellipsoid axis and the declination of Kmax ellipsoid axis.

2-1-4- 2D X-ray images

X-ray images of all U-channels were obtained in EPOC Laboratory (Bordeaux University) using the SCOPIX device and procedure (Migeon et al., 1998).

2-1-5- X-ray microtomography.

High-resolution 3D X-ray imaging was performed on 2 cm-side, oriented cubes (as tests), and on 20 cm-long portions of U-channels. We used an EASYTOM^{TM} XL Nanofocus tomograph located in Grenoble-Alpes University. The source is a tungsten filament producing a source

beam of ~3.5µm in diameter. The receiver is a flat panel of 1840 × 1456 pixels. Helicoidal recording allowed scanning lengths up to 20 cm within a single acquisition in about 5 hours. Reconstruction of the tomographic volume was done with RX-Solution's X-act software. This procedure permitted 3-D imaging of radiodensity within the scanned volume at a 10 µm voxel size. In the latter analysis, we used intensity of gray in the image as a proxy of density, although we note the radiodensity also depends on atomic number. Segmentation of resolved grains provided additional textural properties (grain-size distribution, grain shape and possible preferential orientations). Processing of the scanned images was performed twice with two independent softwares, ImageJ for thresholding and segmenting the grains and the Python scikit-image package for 3D reconstruction.

The high resolution of the microtomography at the 10 µm – scale allows a detailed characterisation of event deposits, albeit only on portions of max. 20 cm. Since X-ray micro-tomography data is sensitive to the density of the material, we used X-ray data in two different ways: (1) by getting a continuous recording of texture, averaging radiodensity along a selected band and (2) by digitally segmenting out the heavy grains embedded within the clayey matrix and characterization of their morphological properties. Heavy grains are segmented slice by slice through thresholding and we performed shape analysis to retrieve their size, orientation, and shape ratio. This analysis allows us to highlight the distribution of these grains with depth.

2-2- Grain-size distribution

Besides measurements dedicated to textural analysis of the grain fabric (§ 3-1-3, 3-1-4, 3-1-5), we made additional observations (optical microscopy) and grain-size measurements on individual samples.

We performed Laser microgranulometry using a MALVERN^{TM} Sizer 2000 laser diffraction particle size analyser (ISTerre Laboratory, Savoie-Mont-Blanc University) on both 1) individual "spatula" samples selected during the IODP Leg 381 OSP (MARUM, University of Bremen), picked at variable spacing of 0.5 to 5 cm, and 2) samples extracted from the U-channels at spacing of 0.5 to 2 cm.

2-3- Chronological control

For the purpose of this study we only require an approximate chronology, for which we follow the general chronostratigraphy deduced from correlation between core data and seismic reflection profiles. Seismic stratigraphy is interpreted in the context of the current

understanding of Late Quaternary sea-level fluctuations and their impact on the Gulf of Corinth. The investigated intervals of this study (Fig. 2) correspond to the last alternation of marine and (semi-)isolated environments. Previous radiocarbon dating and correlation with sea-level curves places the transition between those environments at ~12-13 ka (e.g. McNeill et al., 2019b). Assuming that sedimentation rates between this transition and the underlying marine sub-unit (~70 ka; McNeill et al., 2019b) have been constant, we estimate our oldest U-Channels to be around ~25 ka.

3-Results

Below we present the results of our detailed analyses of the U-channels and spatula samples. Note that additional results are presented as Supplementary Material.

We refer to sedimentary event deposits either as a classical turbidite (**Tu**) or a turbidite+homogenite (**TuHm**). Figure 3 illustrates the two types of event deposits, particularly different in the nature of the transition between a coarse fining-upward lower unit (possibly multiple fining upward sub-units) and a highly homogeneous fine-grained upper unit. The transitions between homogenites and their overlying hemipelagic intervals were defined based on texture (section 3-2) and XRF chemistry (section 3-3); for several event deposits these transitions were also compared with X-ray 3D microtomography data (section 3-5). We use the word "homogenite" only in a descriptive sense: fine-grained layers, lacking visual layering or other features, and apparently sharply separated from a coarser sub-unit. No depositional mechanism is inferred; the interpretation is discussed based on our data and different published investigations in section 4. The word "turbidite" is also used in a descriptive sense. Although the term "hemipelagite" usually concerns marine deposits, in this study we apply it for slowly accumulated background sediments during both marine and "(semi-)isolated" (SI) environments. In the following we use "sub-units" for the different parts within a turbidite (Tu) or a turbidite+homogenite (TuHm) event deposit.

3-1 Layering and composition

The investigated core portions (down to 65 m b.s.f. in borehole M0079A) display a clear layering with alternating dark grey to whitish, essentially fine-grained sediments (silty clay/clayey silt). Minor coarser material (very fine sand to rare medium sand with a clayey-silty matrix) with higher siliciclastic content is present along the whole succession. Individual layers are mm- to tens of cm-thick (*cf.* close ups on Fig. 2), resulting from the intercalation of different types of event deposits within a fine-grained, layered "background" sedimentation

consisting of hemipelagic deposits. Fine-grained facies are calcareous muds in which the carbonate fraction is biogenic or detrital. In the marine interval primary biogenic components mostly consist of nanoplankton and rare planktonic forams, whereas in the SI intervals it mostly consists of bio-induced calcite and diatoms. Detrital grains are mostly calcite for both intervals. The silt- and clay-size clastic fraction comprises calcite, clay minerals, quartz and altered ferromagnesian debris. Aragonite needles also occur, especially in the transition between marine and SI units.

3-2 Grain-size distributions of hemipelagites and homogenites

Given the small amount of samples of turbidites (<5% of all samples), we only focus on the fine-grained layers in this section and Fig. 4. Sampling for grain-size characterization of homogenites and hemipelagites was based on visual observations of the split cores from boreholes M0078B and M0079A. We selected U-channels 1, 2, 5, and 6 within the marine interval, and U-channels 3, 4, 7, and 8 within the SI interval. To characterize each homogenite or hemipelagite sample, we use the D50 (or median) and the D99 that represent the "mean" grain-size and the coarsest grain size fraction, respectively (Fig. 4-A to D), and two grain analysis parameters, sorting and skewness (Fig. 4-E to H). The eight binary cross-plots of these two parameters shown in Figure 4 allow us to investigate: 1) possible differences between hemipelagites and homogenites, and 2) possible influence of the depositional environment (i.e. marine or SI) on both.

Figure 4A-D do not show significant differences neither between the two types of units nor between the two environments; in both cases, hemipelagite values appear slightly more dispersed. Regarding distribution parameters sorting and skewness, all samples depict values between 0.8 and 1.2 for skewness and between 1.7 and 2.5 for sorting, except for a few samples of marine hemipelagites (Fig. 4-E and –G). There are both marine hemipelagite samples that display a very good sorting (< 1.5) and samples that show a weak sorting (> 2.5) and a highly asymmetric distribution. Homogenites do not appear significantly different in marine or SI units. For both environments, homogenite samples appear slightly less dispersed than hemipelagites, and SI homogenites display a similar range of values for sorting and skewness with respect to SI hemipelagites (Fig. 4).

3-3. XRF chemical analysis

Figure 5 summarizes results from all U-channels with separate distributions for hemipelagites, homogenites and turbidites. Supplementary Figure 2 shows additional XRF

counts and Supplementary Figure 3 shows the 24 detailed XRF ratios of all U-channels as a function of depth. We highlight the following main characteristics.

- In terms of biogenic/detrital origin (Fig. 5-a and-c), chosen XRF chemical parameters discriminate the three types of units. Turbidites and homogenites have relatively similar ratios, with the exception of Ca/Fe that is generally lower in homogenites. Homogenites have lower Ca ratios than hemipelagites (Ca/Fe, Ca/Ti, Ca/Sr), indicating a generally higher detrital content. The Ca/Sr ratio in SI conditions (Fig. 5-c) is the only exception, and combined with the decrease in Ti/Sr ratios as well as the overall increase in Sr for the SI U-channels (Suppl. Fig. 2), this suggests that the increased Sr during SI conditions affects hemipelagite composition more than turbidite and homogenite composition.
- In terms of organic content (Fig. 5-b and –d), turbidites, homogenites and hemipelagites have a similar range of values, with the main difference that hemipelagites appear to have mostly a bimodal distribution. The overall lower Br/Cl ratios during SI conditions is in line with the overall Br decrease (Suppl. Fig. 2).
- In terms of sedimentary provenance/grainsize (Fig. 5-e and -g), turbidites show a larger variation with respect to homogenites and hemipelagites, which may be partly due to varied terrigenous sources and/or to larger grain size. Homogenites display a generally narrow range of values, indicating chemical and mineralogical homogeneity with respect to hemipelagites, which generally have a skewed distribution. We note that peak values for Zr/Rb, Ti/Rb and Zr/K in homogenites are slightly lower than hemipelagite peak values during marine conditions, but slightly higher during SI conditions. Given that homogenite values remain relatively constant, this suggests a slight change in the overall mineralogical composition of hemipelagites.
- In terms of productivity and post-depositional alteration (Fig. 5-f and –h), Br/Ti ratios appear slightly higher and more variable during marine conditions for all three types. Concerning S/Ti ratios, homogenites seem to have slightly lower values than those obtained for turbidites and hemipelagites.

Overall these observations show that turbidites, homogenites and hemipelagites have distinct chemical characteristics and that there are some differences in chemical composition between marine and SI depositional environments, particularly within hemipelagites.

3-4. Correlations of geochemical, magnetic and textural parameters

XRF and textural parameters are presented for U-channels 4 and 6 (Figures 6a,b and 7a,b, respectively); the same measurements applied to the other U-channels are available in Supplementary Figure 4, and detailed event deposit description in Supplementary Table 1.

In U-channel 4 (Fig. 6) we observe five different sedimentary event deposits. Event deposits 1 and 5 are classical turbidites (Tu), and event deposits 2, 3 and 4 are turbidite+homogenite deposits (TuHm). Grains are especially coarse for event deposits 2 and 5, with respective D50 values of 30 and 50 μm, which are also the thickest event deposits in this U-channel (5-10 cm). The peak in magnetic susceptibility at the top of event deposit 5 is at the same depth as a cluster of black grains, and thus probably related. AMS foliation is particularly high in the homogenites of event deposits 2 and 4, with the lineation overall low apart from a gradual increase within event deposit 5. In general, the Kmin inclination is close to vertical, indicating relatively flat-lying grains, and the Kmax declination is strongly variable, indicating no strong preferred orientation of grains in the horizontal plane. Looking at the XRF ratios, the Ca/Ti and Ca/Fe ratios are generally lower within sedimentary event deposits, and show sharp changes around transitions with hemipelagic intervals. Zr/Rb is particularly high in turbidites, sharply decreasing upwards within TuHm event deposits 2 and 4, and a more gradual decrease within Tu event deposit 5. The separation between two homogenite intervals (Hm1 and Hm2) in event deposits 2 and 4 is particularly clear from core images and X-rays, and for event deposit 2 this sharp change is also expressed in changing Ca/Ti, Ca/Fe and Fe/Si ratios.

U-channel 6 (Fig. 7) only contains one ~19 cm thick sedimentary event deposit. All selected XRF ratios display highly variable values within the lower turbidite interval between 20.26 and 20.22 m b.s.f., and show similar trends as those of the grain-size variations. The top of the event deposit at 20.06 m b.s.f. is marked by a sharp shift of Ca/Ti, Ca/Fe, Ca/Si, Cu/Rb, and Mn/Ti ratios (Fig. 7 and Suppl. Fig. 4). The visually detected subdivision of the homogeneous mud interval, interpreted as Hm, is confirmed by slight changes of Ca/Ti, Ca/Fe, Ca/Si, Si/Ti, Fe/Rb, and Fe/Ti (Hm1 and Hm2 in Fig. 7), similarly to event deposit 4, but not to event deposit 2 in U-Channel 4 (Fig. 6). The volume magnetic susceptibility is overall low, but higher in the finer-grained intervals than in the coarse base. Magnetic susceptibility roughly follows the same trend as the Fe/Si ratio indicating a likely control of this parameter by the relative proportion of iron oxides. Whereas magnetic susceptibility is constant in Hm1, it shows slightly more variation in Hm2 possibly due to heterogeneities associated with larger grains.

The entire homogenite interval in U-Channel 6 (Fig. 7), displays a higher magnetic foliation with respect to the overlying hemipelagic layer and with respect to the coarse turbidite base. Shape parameter T (oblate ellipsoid distribution), lineation, Kmax declination and Kmin inclination (vertical) do not display clear changes between the different deposit types. When looking at the Hm interval in more detail, we note a change in magnetic foliation around the Hm1/Hm2 separation. Grain-size distribution also underlines this contrast in the D99, but within suspended-load ranges.

3-5. **X-ray micro-tomography data**

3-5-1- Quantitative measurements

Selected portions imaged through X-ray micro-tomography for U-channels 4 and 6 are presented on Figures 6c,d and 7c, respectively with correlation to the detailed XRF profiles. The same measurements applied to U-channels 2 and 8 are available in Supplementary Figure 4. We show the averaged density along a band highlighted with green shading, and the morphological properties of the suspended heavy grains with yellow patches (Figure 6 and 7).

The high porosity associated with the turbiditic base has a stronger effect on the density than the general occurrence of heavier grains, so that the turbiditic base generally has a lower density (average pixel value, Figs 6 and 7) than the underlying hemipelagite. The exception is event deposit 5 in U-Channel 4 in which the entire turbidite interval has a higher density than the underlying hemipelagite. Both homogenite profiles with separate Hm1/Hm2 intervals (event deposits 2 and 4, Fig. 6) have a small offset in density between a slightly heavier Hm1 and lighter Hm2. Also, in U-Channel 4 (event deposit 2, Fig 6d), heavy grains are clearly scarcer above this transition. In the U-Channel 6 event deposit, the base of Hm1 (Fig. 7c) displays faint fluctuation in grey scale.

Figure 6c shows the occurrence and size of heavy grains (see § 3-5) within event deposit 5, fining up gradually, as expected from a dilute turbidite deposit. Similarly, Figure 6d reveals three clear sub-units of coarser laminations with heavy grains at the turbiditic base of event deposit 2 (40.24, 40.235, and 40.21 m b.s.f.). The first and second bottom sub-unit were not resolved by the XRF data, but the microtomography indicates that their grains are similar in nature, both in size distribution and orientation. The third sub-unit within this event deposit at 40.21 m b.s.f. is different in nature, with smaller aspect ratio and finer grains. Grains of this sub-unit are notably different from the previous two sub-units that there is a predominantly horizontal orientation to the grains. This suggests that the third sub-unit is either related to a secondary deposition phase with a different content, was subjected to different energy/flow

dynamics and/or obeyed to a depositional mechanism different from the one responsible for the first two sub-units. The turbidite in U-Channel 6 (Fig. 7c) shows three sub-units with heavier grains (at ~20.255, ~20.237, and ~20.23 m b.s.f.), which are only faintly indicated by the XRF-ratios, but more easily distinguished through microtomography. The lower turbidite sub-unit has a higher aspect ratio and higher concentration of heavy grains than the other two pulses, again indicating a variability between the different sub-units.

3-5-2 Qualitative observations of event deposit structures

X-ray microtomography contributes to our understanding of the origin of the material, the detailed layering, and the texture of sedimentary event deposits, particularly homogenites. Homogenites were previously analysed using core images and magnetic fabric (AMS). Here we benefit from more direct views of the grain fabric using high-resolution 3D microtomography particularly for u-channel portions that contrast in density. Figure 8 shows zoom-ins of sedimentary structures from U-Channels 4 and 6 (additional X-Ray microtomography images for U-Channels 2 and 8 are shown in Supplementary Fig. 5). We show the images without interpretation in Supplementary Fig. 6. Focusing on the basal surface, internal basal structure of the turbidite unit, and the base of the homogenite interval, we highlight several key observations:

- The irregular shape of the base of the turbiditic interval for the thickest observed TuHm event deposits (Fig. 8b), and more subtly the microfractured base of event deposits 2 and 4 of U-Channel 4 (Fig. 8a). In contrast, the single thinner Tu event deposit in U-Channel 4 (Fig, 8a, event deposit 5) displays a smooth planar basal surface. For U-Channel 4 event deposit 2 (Fig. 8a), below the base of the homogenite, we observe a deformed interval involving fine-grained and slightly coarser layers.
- A complex distribution of coarser siliciclastic grains in the turbiditic interval base for the observed TuHm event deposits with multiple turbiditic laminations (Fig. 8). Based upon TuHm event deposits investigated here, this structure appears complex, including several microfractured intervals within the coarser-grained portions of the sedimentary event deposits. These intervals have transitional bases and tops, which also correspond to downward and upward reduction and eventual disappearance of the microfractures. This suggests that microfracturing developed only within sub-units having a favourable rheology (grain-size distribution), even if the forces resulting in microfracturing probably also acted on the finer-grained sub-units.

- The successive occurrence of low-angle cross-bedding in the turbidite of U-Channel 6, particularly clear in middle part of the turbidite (Fig. 8b). We systematically verified the opposite dips in this cross-bedding using 2D views under multiple angles, excluding the possibility that the dips are ripple/dune structures that only appear opposite under certain viewing angles.

4- Discussion

Before attempting to interpret our observations and measurements in terms of depositional mechanism (e.g. bed-load, suspended load, *in situ* reworking, *etc*.) and triggering process (e.g. gravity reworking, ground shaking, tsunami wave, *etc*), we briefly review and summarize previously published nomenclature and interpretations of sedimentary event deposits. In Figure 9, we show a schematic illustration of the main types of event deposits discussed here, without detailed internal subdivisions.

4-1- Turbidites and homogenites: brief reminders

Relationships between sediment-carrying bottom density currents and specific types of sedimentary deposits (i.e. turbidites; Fig. 9a, similar to Fig. 3b) were established half-a-century ago, following *in situ* observations, measurements and laboratory analyses of outcropping deep-water formations. The first model to describe the internal subdivisions of individual turbidite beds was that of the "Bouma sequence" (Bouma, 1962), relating turbidites to gravity-driven flows evolving from fluidized slumps. Later on, several other models were proposed as well (for a review, see Talling et al., 2012). Other types of sedimentary deposits, whose internal structure differs from that of the initial "Bouma sequence", have also been attributed to concentrated, particle-laden, gravity flows (e.g. in Lowe, 1982; Stow, 1992; Stow and Wetzel, 1990). The significance of the initial internal subdivisions of a turbidite *sensu* Bouma sequence has been questioned by several authors, both with regards to the mechanical processes involved (e.g. Talling et al., 2012) and to layers that are unrelated to gravity-driven flows (e.g. Shanmugam, 1997). Importantly, underflow prolongation of a river discharge (hyperpycnal flows) may produce turbidites (Mulder and Syvitski, 1995), but should not be considered as gravity-reworking event (e.g. Arnaud et al., 2002; Beck, 2009).

High resolution surveys, both in marine and lacustrine settings (geophysical imaging and coring), have pointed out another type of reworking deposit consisting of anomalously thick, fine-grained, homogeneous sediment with little or no coarse fraction at the base (Fig. 9b). These "unifites" (Stanley, 1981) or "homogenites" (Kastens and Cita 1981; Cita et al., 1996;

San Pedro et al., 2017) were interpreted as resulting from tsunami wave impacts on the sea floor, and/or from seiches within a confined setting (e.g. Chapron et al., 1999, Mulder et al., 2009). In enclosed basins like the Gulf of Corinth, tsunamis are caused by displacement of the sea/lake floor during earthquakes and/or non-seismically triggered slumping, and a seiche is the harmonic resonance of waves within the basin as the tsunami is reflected and the water oscillates back and forth (e.g. Ichinose et al., 2000). Both tsunamis and seiches affect the entire water column, and increase pore fluid pressure to facilitate erosion and deformation (see discussion in Alsop and Marco, 2012). We are not aware of any criteria to differentiate between seiche and tsunami-induced homogenites in enclosed basins like the Gulf of Corinth. As an alternative scenario to tsunami/seiche induced deposits, slope failure of fine-grained sediments with no or very little coarse fraction may also result in turbidity currents and homogenite deposition. A particular 3D structure is often reported for homogenite deposits: a large thickness, onlapping geometry in all directions, and no visible lateral transition to coarser layers or a mass-transport deposit (no visible" "root").

Additionally, different investigations in marine as well as lacustrine settings, have described both 1) turbidites displaying a sharp transition between the coarse, fining-upward, lower part, and the homogeneous fine-grained upper sub-unit, and 2) incomplete turbidites associated with a homogenite (Siegenthaler et al., 1987; Sturm et al., 1995; Beck et al., 2007) (Fig. 9c, similar to Fig. 3a). Both cases are inferred to represent a unique instantaneous sedimentary event deposit for which the settling of the final fine-grained suspension requires an additional process apart from the final and/or distal damping of a single bottom monophasic turbidity current. Whereas we use the term "Turbidite+Homogenite " (TuHm) for these deposits (as in Campos et al., 2013ab, McHugh et al., 2014), we note that others have referred to similar deposits as turbidites (e.g. Van Daele et al., 2015), megaturbidites (e.g. Polonia et al., 2013) or homogenites with a coarse base (e.g. Moernaut et al., 2017). The link of turbidite+homogenite deposition with slope failure followed by tsunami waves and/or seiches is based on sediment textural analyses (Chapron et al., 1999; Beck et al., 2007; Campos et al., 2013b) and on exceptional post-earthquake *in situ* surveys (Thunell et al., 1999; McHugh et al., 2011; Lorenzoni et al., 2012; Van Daele et al., 2015). Alternatively, if a large amount of re-mobilised fine-grained sediments ends up in suspension following slope failure, tsunamis and/or seiches may not necessarily be involved.

In some cases, evidences of to-and-fro bottom currents have been observed between the two sub-units of TuHm deposits (Fig. 9d; Beck et al, 2007; Campos et al., 2013a;), represented by thin silty laminae at the base of a single homogenite (Chapron et al, 1999).

Apart from single TuHm deposits, multiple TuHm may be separated by little or no hemipelagic interval (Van Daele et al., 2017). For such cases we underline the difference between a unique event deposit with multiple fining-upward sub-units resulting in an amalgamated turbidite (Fig. 9e) and a separate, stacked event deposits occurring with a high frequency (Fig. 9f).

Sharp grain-size breaks within sedimentary event deposits, as in TuHm deposits, have also been described in relation to a bimodal grain-size distribution within a flow (e.g. Kane et al., 2007), reflective flows (e.g. Pickering and Hiscott, 1985), flow separation due to topographic obstacles (Sinclair and Cowie, 2003), vertical flow stratification (Gladstone and Sparks, 2002) and fluctuations in flow capacity (Kneller and McCaffrey, 2003), although none of these cases would result in the characteristic homogeneous fine-grained upper part of the deposit (see models in Stevenson et al., 2014). Alternatively, fluid mud layers can hinder the settling of non-cohesive grains that bypass these layers downslope to form deposits with sand sharply separated from structureless mud, with the mud thickness increasing towards topographic lows (Stevenson et al., 2014). We note that such a model could also result in deposits similar to turbidites+homogenites. Turbidite lofting resulting from suspension clouds in relation to hyperpycnal flows (Zavala et al., 2011), or "dilute plume" river deposition (Hizzett et al., 2018; Hage et al., 2019) could also result in sand-mud couplets with sharp transitions, but are typically more rhythmic in nature and more abundant in plant remains than surge-like gravity reworking deposits (Zavala and Acuri 2016).

4.2 Inferred depositional mechanisms Corinth Rift event deposits

4-2-1 The classical view: from grain-size analysis, AMS and XRF studies

Grainsizes are consistently fining upwards within all studied turbidites, and we emphasize that gradual or sharp changes clearly mark the difference between turbidite and TuHm sedimentary event deposits, respectively (Fig. 4). Similar to previous studies (e.g. Rothwell et al., 2006; Konfirst et al., 2011), we find that Zr/Rb, Si/Al and Fe/Si appear to be useful chemical proxies for grainsize, showing very similar trends to D50/D99 (Figs. 6 and 7; Supplementary Fig. 3). Our XRF results are generally in agreement with those of Campos (2014) for nearby sedimentary core MD01-2477 (Fig. 1), which show Ca/Fe, Ca/Ti and Ca/Si as good indicators of homogenites. As such, although a large part of the catchment in the Corinth Rift is carbonate-dominated (e.g. Gawthorpe et al., 2018; Fig. 1), the overall lower Ca content of the reworked sediments suggests a higher siliclastic detrital content for event beds compared to the more biogenic hemipelagites. Homogenites may represent either

allochtonous material or *in situ* reworking (re-suspension and re-settling) of fine-grained material; the difference in composition between homogenites and hemipelagites favours the former.

Our AMS results are also similar to previous findings (Campos et al., 2013b; Maffione and Morris, 2017) in the sense that homogenites are characterised by high foliation (Figs. 6; 7) and corrected anisotropy degree Pj (Supplementary Fig. 4). For future work on sedimentary event deposits in the IODP-381 cores, the XRF results appear particularly useful given their ability to help distinguish >2 cm thick turbidites and homogenites from hemipelagites (Figs. 5, 6, 7) and their availability at 2 cm resolution for most of borehole M0079A (McNeill et al., 2019a).

In addition to confirming previous findings using classical parameters, as mentioned above, our detailed microtomographic analysis highlights two novel observations. Firstly, lower Tu sub-units with bedding that is complex, multilayered, coarse and overall normal graded, appear to be rule rather than exception. Given the scale of the analysis, Campos et al. (2013a) did not resolve this in their study of comparable deposits in the Corinth Rift. Secondly, several homogenite sections of TuHm event deposits actually consist of multiple intervals. This subdivision is different from previously published cases where a homogenite gradually changes upwards from faintly layered to structureless (e.g. Beck et al., 2019). Here, the transition (Hm1/Hm2 on Fig. 6, 7C and D) involves sharp changes in chemical and textural parameters. We briefly discuss these two findings in the following section.

4-2-2 A more complex view from X-ray microtomography images

Although our results concern short portions of selected sedimentary event deposits, both the turbiditic base and the overlying homogenite of a TuHm deposit reveal a distinct complexity when imaged through X-ray microtomography (Figs. 8 and 10).

Concerning the basal parts of TuHm's, we highlight, from base to top: 1) the occurrence of complex basal surfaces. We interpret the curved shapes (Fig. 8b) to be formed by erosion of a dense coarse flow; due to the small size of the U-channel, only part of a groove cast-type surface may have been crossed (Fig. 10a). We interpret the planar subvertical shapes (Fig. 8b) as microfractures in the underlying mud, before the arrival of the basal turbidite (Fig. 10a). Following the criteria in McNeill et al. (2019a), we prefer this interpretation over drilling-induced fractures as they are planar and do not appear influenced by the core liner or core axis orientation. Generally, the upper sections of the boreholes we investigate here are relatively well-preserved with little coring disturbance, as they were

drilled in push mode (McNeill et al., 2019a). In the core sections we studied, we did not observe liquefaction or fluid-escape features (Fig. 10a), as mentioned elsewhere at the turbidite/hemipelagite interface (e.g. Beck et al, 2007). The difference between an irregular and a smooth turbidite base (Fig. 8) may be explained by more friction at the base of the turbid flow (irregular base) *versus* a total decoupling (smooth base), or by variable erosion in relation to energy of the flow. 2) Within the coarser-grained lower part of U-Channel 6 (Fig. 8b), we observe clear low-angle cross-bedding (in 2D and 3D). Classical schematic subdivision of turbidites (e.g. Bouma, 1962) often indicates, in this position, climbing ripples following a unique flow direction. Here, we interpret successive opposite directions as an effect of complex flow patterns similar to previously described to-and-fro intervals (Campos et al., 2013a) or reflected turbidites (Pickering and Hiscott, 1985). Alternatively, amalgamated turbidites originating from different slopes may also show different flow directions (e.g. Wils et al., 2021), but we do not observe clear coarsening between separate pulses (Van Daele et al., 2017) so we do not favour this interpretation; 3) faint turbidite layering, related to progressive grain-size distribution changes, fitting the description of amalgamated turbidites (Van Daele et al., 2017). In two cases (event deposit 2 in U-Channel 4, Fig. 8a and the event deposit in U-Channel 6, Fig. 8b), microfractures are concentrated within the coarser sub-units.

As mentioned in § 3-4 and 4-1, several homogenite sections of TuHm event deposits appear to consist of separate sub-units on split core surface and X-ray images (U-Channel 4 (40.04 and 40.175 m b.s.f., event deposits 2 and 4, Fig. 6); and U-Channel 6 (20.15 m b.s.f., Fig. 7 (as well as U-Channels 2, 5, 7 and 8; Supplementary Figs. 3, 4, and Supplementary Table 1)). The XRF profiles show changes between the homogenite sub-units, but not in a consistent manner in the three examples in U-Channels 4 and 6. X-ray microtomography adds two observations concerning the Hm-subdivision: subtle density differences between the homogenite sub-units in U-Channel 4 (Fig. 6), and faint laminations at the base of the lower homogenite sub-units in U-Channel 6 (Fig. 7). We relate the homogenite subdivision to two settling phases: initial high-density suspension behaviour followed by longer lasting settling from a stable suspension. The observed XRF and structural variations imply that non-uniform settling is guided by the composition of the initial suspension and by slight segregations among suspended particles (Fig. 10b, case B).

Details displayed by X-ray microtomography also question the location of the TuHm transition, especially for event deposit 2 of U-Channel 4 (Fig. 8a) and U-Channel 6 (Fig. 8b). In U-Channel 6, two similar fine-grained sub-units overlie cross-stratified coarser laminations. The lower one may represent a Hm1, overlain by a Hm2, as mentioned above,

and interpreted as a change in settling (intrinsic cause; e.g. evolution from a high-density suspension to lower-density one). We propose a similar interpretation for the faint layering within U-Channel 4 event deposit 4 (Fig. 10b, case B). The soft-sediment deformation within U-Channel 4 (event deposit 2; Fig. 8a), which we interpret as slumping, occurred after the beginning of suspension settling; this disturbed sub-unit may be considered as part of the homogenite (Fig. 10b case C, and Fig. 10c). This feature, as well as microfractures within the turbiditic unit and possibly within a transition interval (Fig. 10c), clearly represents a post-turbidite disturbance. If the initial turbidite was earthquake-related, this post-turbidite disturbance may be related either to ongoing strong oscillations or to new shaking events, possibly aftershocks.

Several authors have described, at the TuHm transition, coarser lamina that they relate to re-mobilization of shallow-water sediments (e.g. Chapron et al., 1999, Moernaut et al., 2017); such surficial remobilization has been clearly demonstrated for major subduction earthquakes and tsunamis, using short-lived radiogenic isotopes (McHugh et al., 2016). For large closed basins, a sharp thermocline may be affected by internal Kelvin waves that erode soft sediments where the thermocline impinges on the slope (e.g. Bouffard and Lemmin, 2013). This process may have played a role as well within the Gulf of Corinth (Fig. 10b, case D), and could explain the complexities observed within the homogenite deposits.

4-2-3 Depositional mechanisms of IODP-381 sedimentary event deposits

The most common triggers of sedimentary event deposits are earthquakes, tsunamis, seiche, coastal/subaqueous landslides and/or floods. For the larger event deposits here studied, like event deposit 2 in U-Channel 4 (~10 cm) and the event deposit in U-Channel 6 (~20 cm), we find seismic or aseismic slope failures followed by a tsunami/seiche the most straightforward interpretation, given the complex turbidite base, microfracturing and evidence for ongoing oscillations (Fig. 10).

Assuming a uniform seismic attenuation relationship for the Corinth region, the earthquakes responsible for triggering mass wasting should be the ones strongest and closest to unstable slopes (e.g. Ambraseys, 1988). The faults and the slopes on the southern basin margin (Fig. 1) therefore seem the most likely source for such events: the faults are the Rift's largest in terms of throw (Fernández-Blanco et al., 2019b) and have the highest late Quaternary slip rates (Nixon et al., 2016). Given the asymmetry of the half-graben (De Gelder et al., 2019) the slopes are also steeper on the S than the N margin. The S margin slopes near

the coring sites extend from ~100 m to ~800 m b.s.l., dipping ~20° in the upper slopes and more than 30° in the lower slopes (Charalampakis et al., 2014), and have been shown to be highly unstable (Ferentinos et al., 1988; Lykousis et al., 2009). High-resolution seismic profiles at the coring sites are lacking, but at the base of the lower slopes along most of the S margin, several mass-transport deposits have been observed on seismic data (Ferentinos et al., 1988; Charalampakis et al., 2014), indicating that gravity reworking was likely the main cause of the event deposits. As mentioned before, gravity reworking/subaqueous landslides in the Corinth Rift can also be triggered aseismically, specifically during the rainy season when high sediment influx is causing slope instabilities near river mouths (Galanopoulos et al., 1964; Heezen et al., 1966). On the basin floor of the W-Corinth Rift, 6 out of 7 sedimentary event deposits were correlated with historical earthquakes, and only 1 to an aseismic submarine landslide (Beckers et al., 2017). As such, we also suspect that most of the sedimentary event deposits in the IODP-381 cores showing evidence for gravity reworking are earthquake triggered. In terms of tsunamis, historical tsunamis in the Corinth Rift have ranged in run-up height from some 10s of cm's to several meters, with 15 out of 17 events (compilation in Kortekaas et al., 2011) related to earthquakes and 2 to aseismic landslides. Even if coastal damage was minor for some of these events, we emphasize that homogenite deposition on the basin floor would mostly result from fine-grained material ending up in suspension during subaqueous slope failures and surficial remobilization (e.g. McHugh et al., 2016). Although it is not straightforward to distinguish these two sources, the preservation potential of basin-floor tsunami deposits seems greater than that of the often-incomplete near-shore and beach environments (Alsop and Marco, 2012). To better resolve the possible link between earthquakes/tsunamis and sedimentary event deposits in the Corinth Rift, future work will focus on a detailed comparison with the paleoseismic and paleotsunami record, supported by radiocarbon dating of event deposits, but this is beyond the scope here.

In contrast to the larger (>10 cm) event deposits mentioned above, for smaller event deposits without complex turbidite base, microfracturing and evidence for ongoing oscillations, like event deposit 3 in U-Channel 4 (~2 cm), we consider other processes than gravity reworking similarly possible. As mentioned before (§ 4-1), the sharp grain-size breaks within the TuHm deposits can also be interpreted as the result of turbidite lofting (Zavala et al., 2011) or fluid mud layers that hinder the settling of non-cohesive grains (Stevenson et al., 2014). In future work, one possible way to help distinguish the depositional mechanism is to look in more detail to organic content within the sedimentary event deposits (Zavala and Arcuri, 2016).

4-2-4 Possible effect of the depositional environments on structure/composition of sedimentary event deposits

All previous remarks on specific layers can also be discussed within the context of two depositional environments; marine and SI. In neighbouring Core MD01-2477, although only covering ~6 ka of the SI interval, Campos et al. (2013a) mention generally thicker sedimentary event deposits within the marine interval compared to the underlying SI interval. They tentatively attribute this tendency to more available detrital material in source areas; the authors consider that erosional products may have been stored at shallow depths during the LGM, and mobilized later during the Holocene. With an average 13 cm for the 9 marine sedimentary event deposits and 12 cm for the 10 SI event deposits we cannot observe such a trend, but our number of samples are too small to draw robust conclusions. Other studies have also focused on differences in sedimentary event frequency during glacial and Holocene times (e.g. Beck et al., 2007), in relation to changes in erosion/sedimentation rates, sea-level and shelf geometry. Such an analysis is beyond the scope of this study, but we note that the hypothesis of thicker and less frequent event deposits during marine periods can be easily tested in a future study on sedimentary event deposit size and frequency over a larger vertical section.

Concerning the combined thickness of sedimentary event deposits and hemipelagic deposition, McNeill et al. (2019b) showed on the longer IODP-381 cores that sedimentation rates and the input of coarse material (sands, silts) are generally lower during marine than in SI intervals. Similar to Collier et al. (2000), they conclude that both reduction and change of vegetation cover led to stronger soil erosion and higher sediment flux into the basin during the SI intervals. In the core portions investigated here, we find two major differences between marine and SI environments: 1) Higher Sr and Sr/Ti concentrations within the SI interval (Fig. 5 and Supplementary Fig. 2), particularly for hemipelagic sedimentation. We relate this to the aragonite needles occurring more frequently within the SI interval than in the marine interval, especially in the transition from marine to SI environments (Campos, 2014; McNeill et al., 2019a,b). Their occurrence is a possible consequence of either *in situ* mixing of marine and fresh water, or precipitation in shallow areas and subsequent remobilization and transport (Moretti et al., 2004; Lykousis et al., 2007); 2) Hemipelagites seem to be more sensitive to environmental changes than homogenites, specifically for Ti/Sr, Zr/Rb, Ti/Rb and Zr/K (Fig. 5). This suggests that similar fine-grained deposits are reworked during both marine and SI conditions, even if *in situ* hemipelagic deposition changes. We envision that differences in

water depth and shelf geometry during marine and SI conditions could affect tsunami/seiche generation and thus homogenite thickness and structure, but in our limited homogenite sample size we cannot observe this.

Both findings mentioned above concern hemipelagic deposition rather than sedimentary event deposits. As such, we consider that to a first order the depositional processes inferred for sedimentary event deposits on the Corinth Rift basin floor are similar in marine and SI environments in terms of thickness, structure and composition.

5. Conclusions and perspectives

The main goal of our present investigation is to improve our understanding of sedimentary event deposits in the Central Gulf of Corinth during the last ~25 ka, using a combination of grainsize, magnetic and chemical parameters with high-resolution X-Ray microtomography. We highlight the following outcomes of our analyses.

1) Grain-size, AMS and XRF measurements provide efficient means to distinguish sedimentary event deposits (turbidite and TuHm deposits) from hemipelagic background sediments for the event deposits recorded within boreholes M0078B and M0079A of IODP Expedition 381. X-Ray microtomography is complementary to those measurements as it provides observations of differences in density and texture down to the clay/silt grain-scale.

2) X-Ray microtomography evidences the complexity of basal turbidites within a sedimentary event deposit. Through 3D imaging we can detect microfractures and erosional features relating to basal surface, and multiple coarse-grained turbiditic sub-units (Fig. 10), which we interpret as expressions of complex gravity flows. Successive cross-bedded sets, dipping in opposite directions, are interpreted as indicative of water mass oscillations typical for tsunamis/seiches or due to turbidite reflection within the enclosed Gulf.

3) X-Ray microtomography helps detecting faint layering (sometimes folded) within homogenites, possibly related to discrete changes in composition and grain-size. We interpret these features as indications of intrinsic settling fluctuations, ongoing water mass displacement during homogenite deposition and/or the intercalation of coarser material during subsequent gravity flows (Fig. 10b).

4) We interpret the larger (>10 cm) event deposits that we studied here as the result of seismic or aseismic slope failures followed by tsunami/seiche waves, given the complex turbidite base, microfracturing and evidence for ongoing oscillations. For

smaller event deposits in which we did not observe this, we also consider other processes like hyperpycnal flows and sediment lofting possible.

5) In terms of environmental influences on sedimentary event deposits, XRF results indicate that turbidites and homogenites are less sensitive to changes between marine and (semi-)isolated conditions than the hemipelagic sedimentation. Within our limited sample size we do not observe major differences in terms of sedimentary event deposit thickness, composition and structure.

In a general sense, X-ray microtomography can document characteristics of all types of sedimentary event deposits to better understand their origins. More specifically, it can provide additional observations that assist in the interpretation of the seismic/tsunami origins, and help achieve a chronicle of regional paleoseismicity, either in the Corinth Rift or elsewhere.

Acknowledgements

All authors declare that there are no conflicts of interest in relation to this article. This research used samples and/or data provided by the International Ocean Discovery Program (IODP). Funding for this research was provided by IODP-France. GdG and CS thank IODP-France for the financial support and postdoctoral scholarship that helped us carry out this research. GC publishes with permission of the Director of the British Geological Survey (United Kingdom Research and Innovation). RLG thanks the VISTA programme of Norwegian Academy of Science and Letters for the award of its VISTA Professorship which also provided support to SP in order to undertake research on IODP Expedition 381, and RLG also acknowledges support from the Research Council of Norway (DeepRift project; number 308805). We thank OSUG@2020 for its contribution to the X-ray microtomography funding and Pierre Lhuissier from the SIMAP laboratory for his help in performing X-Ray tomography acquisition. We thank all IODP-381 expedition members for insightful discussions on a wide spectrum of topics in relation to the Corinth Rift.

Data Availability Statement

Preliminary results of the whole OSP and raw data of IODP Expedition 381 (Expedition Report) are accessible on http://www.ecord.org/expedition381/. Additional data that support the findings of this study are available from the corresponding author upon reasonable request.

REFERENCES

Alsop, G. I., & Marco, S. (2012). Tsunami and seiche-triggered deformation within offshore sediments. *Sedimentary Geology*, *261-262*, 90–107.

Ambraseys, N. N. (1988), Engineering seismology, *Earthquake Eng. Struct. Dyn.,* 17, 1–105.

Armijo, R., Meyer, B., King, G. C. P., Rigo, A., & Papanastassiou, D. (1996). Quaternary evolution of the Corinth Rift and its implications for the Late Cenozoic evolution of the Aegean. *Geophysical Journal International*, *126*(1), 11–53.

Arnaud, F., Lignier, V., Revel, M., Desmet, M., Beck, C., Pourchet, M., Charlet, F., Trentesaux, A., & Tribovillard, N. (2002). Flood and earthquake disturbance of 210Pb geochronology (Lake Anterne, NW Alps). *Terra Nova*, *14*(4), 225–232.

Beck, C. (2009). "Late Quaternary lacustrine paleo-seismic archives in north-western Alps: Examples of earthquake-origin assessment of sedimentary disturbances." *Earth-Science Reviews*, *96*(4), 327–344.

Beck, C., Campos, C., Eriş, K. K., Çağatay, N., Mercier de Lepinay, B., & Jouanne, F. (2015). Estimation of successive coseismic vertical offsets using coeval sedimentary events--application to the southwestern limit of the Sea of Marmara's Central Basin (North Anatolian Fault). *Natural Hazards and Earth System Sciences*, *15*(2), 247–259.

Beck, C., Carrillo, E., Audemard, F., van Welden, A., & Disnar, J.-R. (2019). Tentative integration of paleoseismic data from lake sediments and from nearby trenches: the central section of the Boconó Fault (northern Venezuela). *Journal of South American Earth Sciences*, *92*, 646–657.

Beck, C., Mercier de Lépinay, B., Schneider, J.-L., Cremer, M., Çağatay, N., Wendenbaum, E., Boutareaud, S., Ménot, G., Schmidt, S., Weber, O., Eris, K., Armijo, R., Meyer, B., Pondard, N., Gutscher, M.-A., Turon, J.-L., Labeyrie, L., Cortijo, E., Gallet, Y., … Jaouen, A. (2007). Late Quaternary co-seismic sedimentation in the Sea of Marmara's deep basins. *Sedimentary Geology*, *199*(1), 65–89.

Beck, C., Reyss, J.-L., Leclerc, F., Moreno, E., Feuillet, N., Barrier, L., Beauducel, F., Boudon, G., Clément, V., Deplus, C., & Others. (2012). Identification of deep subaqueous co-seismic scarps through specific coeval sedimentation in Lesser

Antilles: implication for seismic hazard. *Natural Hazards and Earth System Sciences*, *12*(5), 1755–1767.

Beckers, A., Beck, C., Hubert-Ferrari, A., Reyss, J.-L., Mortier, C., Albini, P., Rovida, A., Develle, A.-L., Tripsanas, E., Sakellariou, D., Crouzet, C., & Scotti, O. (2017). Sedimentary impacts of recent moderate earthquakes from the shelves to the basin floor in the western Gulf of Corinth. *Marine Geology*, *384*, 81–102.

Beckers, A., Hubert-Ferrari, A., Beck, C., Papatheodorou, G., Batist, M. de, Sakellariou, D., Tripsanas, E., & Demoulin, A. (2018). Characteristics and frequency of large submarine landslides at the western tip of the Gulf of Corinth. *Natural Hazards and Earth System Sciences*, *18*(5), 1411–1425.

Bell, R. E., McNeill, L. C., Bull, J. M., Henstock, T. J., Collier, R. E. L., & Leeder, M. R. (2009). Fault architecture, basin structure and evolution of the Gulf of Corinth Rift, central Greece. *Basin Research*, *21*(6), 824–855.

Bell, R. E., McNeill, L. C., Henstock, T. J., & Bull, J. M. (2011). Comparing extension on multiple time and depth scales in the Corinth Rift, Central Greece. *Geophysical Journal International*, *186*(2), 463–470.

Bernard, P., Lyon-Caen, H., Briole, P., Deschamps, A., Boudin, F., Makropoulos, K., Papadimitriou, P., Lemeille, F., Patau, G., Billiris, H., Paradissis, D., Papazissi, K., Castarède, H., Charade, O., Nercessian, A., Avallone, A., Pacchiani, F., Zahradnik, J., Sacks, S., & Linde, A. (2006). Seismicity, deformation and seismic hazard in the western rift of Corinth: New insights from the Corinth Rift Laboratory (CRL). *Tectonophysics*, *426*(1), 7–30.

Bouffard, D., & Lemmin, U. (2013). Kelvin waves in Lake Geneva. *Journal of Great Lakes Research*, *39*(4), 637–645.

Bouma, A.H., 1962. Sedimentology of some Flysch Deposits: A Graphic Approach to Facies Interpretation. Elsevier, Amsterdam, 168 pp..

Briole, P., Rigo, A., Lyon-Caen, H., Ruegg, J. C., Papazissi, K., Mitsakaki, C., Balodimou, A., Veis, G., Hatzfeld, D., & Deschamps, A. (2000). Active deformation of the Corinth rift, Greece: Results from repeated Global Positioning System surveys between 1990 and 1995. *Journal of Geophysical Research*, *105*(B11), 25605–25625.

Campos, C. (2014). *Comparative study of co-seismic sedimentation in two tectonically active areas: the Sea of Marmara and the Gulf of Corinth. Methodological developments, implication for seismic hazards assessment*. PhD Thesis Memoir, Grenoble University, 248 pp.

Campos, C., Beck, C., Crouzet, C., Carrillo, E., Van Welden, A., & Tripsanas, E. (2013a). Late Quaternary paleoseismic sedimentary archive from deep central Gulf of Corinth: time distribution of inferred earthquake-induced layers. *Annals of Geophysics*, *56*(6). https://doi.org/10.4401/ag-6226

Campos, C., Beck, C., Crouzet, C., Demory, F., Van Welden, A., & Eris, K. (2013b). Deciphering hemipelagites from homogenites through anisotropy of magnetic susceptibility. Paleoseismic implications (Sea of Marmara and Gulf of Corinth). *Sedimentary Geology*, *292*, 1–14.

Chapron, E., Beck, C., Pourchet, M., & Deconinck, J.-F. (1999). 1822 earthquake-triggered homogenite in Lake Le Bourget (NW Alps). *Terra Nova*, *11*(2-3), 86–92.

Charalampakis, M., Lykousis, V., Sakellariou, D., Papatheodorou, G., & Ferentinos, G. (2014). The tectono-sedimentary evolution of the Lechaion Gulf, the south eastern branch of the Corinth graben, Greece. *Marine Geology*, *351*, 58–75.

Cita, M. B., Camerlenghi, A., & Rimoldi, B. (1996). Deep-sea tsunami deposits in the eastern Mediterranean: New evidence and depositional models. *Sedimentary Geology*, *104*(1), 155–173.

Collier, R. E. L., Leeder, M. R., Trout, M., Ferentinos, G., Lyberis, E., & Papatheodorou, G. (2000). High sediment yields and cool, wet winters: Test of last glacial paleoclimates in the northern Mediterranean. *Geology*, *28*(11), 999–1002.

Cornet, F. H., Doan, M. L., Moretti, I., & Borm, G. (2004). Drilling through the active Aigion Fault: the AIG10 well observatory. *Comptes Rendus: Geoscience*, *336*(4), 395–406.

Croudace, I. W., Rindby, A., & Guy Rothwell, R. (2006). ITRAX: description and evaluation of a new multi-function X-ray core scanner. *Geological Society, London, Special Publications*, *267*(1), 51–63.

de Gelder, G., Fernández-Blanco, D., Melnick, D., Duclaux, G., Bell, R. E., Jara-Muñoz, J., Armijo, R., & Lacassin, R. (2019). Lithospheric flexure and rheology determined by climate cycle markers in the Corinth Rift. *Scientific Reports*, *9*(1), 4260.

de Gelder, G., Jara-Muñoz, J., Melnick, D., Fernández-Blanco, D., Rouby, H., Pedoja, K., Husson, L., Armijo, R., & Lacassin, R. (2020). How do sea-level curves influence modeled marine terrace sequences? *Quaternary Science Reviews*, *229*, 106132.

Ferentinos, G., Papatheodorou, G., & Collins, M. B. (1988). Sediment Transport processes on an active submarine fault escarpment: Gulf of Corinth, Greece. *Marine Geology*, *83*(1), 43–61.

Fernández-Blanco, D., de Gelder, G., Lacassin, R., & Armijo, R. (2019a). Geometry of flexural uplift by continental rifting in Corinth, Greece. *Tectonics.* https://doi.org/10.1029/2019TC005685

Fernández-Blanco, D., de Gelder, G., Lacassin, R., & Armijo, R. (2019b). A new crustal fault formed the modern Corinth Rift. *Earth Science Reviews,* Vol. 199, 102919

Galanopoulos, A., Delimbasis, N. D., & Comninakis, P. E. (1964). A tsunami generated by a slide without a seismic shock. *Geological Chronicles of Greece*, *16*, 93–110.

Gawthorpe, R., Leeder, M., Kranis, H., Skourtsos, E., Andrews, J., Henstra, G., Mack, G., Muravchik, M., Turner, J., & Stamatakis, M. (2018). Tectono-sedimentary evolution of the Plio-Pleistocene Corinth rift, Greece. *Basin Research*. http://onlinelibrary.wiley.com/doi/10.1111/bre.12260/full

Gladstone, C., & Sparks, R. S. J. (2002). The significance of grain-size breaks in turbidites and pyroclastic density current deposits. *Journal of Sedimentary Research*, *72*(1), 182–191.

Goldfinger, C., Morey, A. E., Nelson, C. H., Gutiérrez-Pastor, J., Johnson, J. E., Karabanov, E., Chaytor, J., & Eriksson, A. (2007). Rupture lengths and temporal history of significant earthquakes on the offshore and north coast segments of the Northern San Andreas Fault based on turbidite stratigraphy. *Earth and Planetary Science Letters*, *254*(1), 9–27.

Gràcia, E., Vizcaino, A., Escutia, C., Asioli, A., Rodés, Á., Pallàs, R., Garcia-Orellana, J., Lebreiro, S., & Goldfinger, C. (2010). Holocene earthquake record offshore Portugal (SW Iberia): testing turbidite paleoseismology in a slow-convergence margin. *Quaternary Science Reviews*, *29*(9), 1156–1172.

Hage, S., Cartigny, M. J. B., Sumner, E. J., Clare, M. A., Hughes Clarke, J. E., Talling, P. J., Lintern, D. G., Simmons, S. M., Silva Jacinto, R., Vellinga, A. J., Allin, J. R., Azpiroz-Zabala, M., Gales, J. A., Hizzett, J. L., Hunt, J. E., Mozzato, A., Parsons, D.

R., Pope, E. L., Stacey, C. D., … Watts, C. (2019). Direct Monitoring Reveals Initiation of Turbidity Currents From Extremely Dilute River Plumes. *Geophysical Research Letters*, *46*(20), 11310–11320.

Heezen, B. C., Ewing, M., & Johnson, G. L. (1966). The Gulf of Corinth floor. *Deep Sea Research and Oceanographic Abstracts*, *13*(3), 381–411.

Hizzett, J. L., Hughes Clarke, J. E., Sumner, E. J., Cartigny, M. J. B., Talling, P. J., & Clare, M. A. (2018). Which triggers produce the most erosive, frequent, and longest runout turbidity currents on deltas? *Geophysical Research Letters*, *45*(2), 855–863.

Ichinose, G. A., Anderson, J. G., Satake, K., Schweickert, R. A., & Lahren, M. M. (2000). The potential hazard from tsunami and Seiche waves generated by large earthquakes within Lake Tahoe, California-Nevada. *Geophysical Research Letters*, *27*(8), 1203–1206.

Jelinek, V. (1981). Characterization of the magnetic fabric of rocks. *Tectonophysics*, *79*(3), T63–T67.

Jolivet, L., Labrousse, L., Agard, P., Lacombe, O., Bailly, V., Lecomte, E., Mouthereau, F., & Mehl, C. (2010). Rifting and shallow-dipping detachments, clues from the Corinth Rift and the Aegean. *Tectonophysics*, *483*(3), 287–304.

Kane, I. A., Kneller, B. C., Dykstra, M., Kassem, A., & McCaffrey, W. D. (2007). Anatomy of a submarine channel–levee: An example from Upper Cretaceous slope sediments, Rosario Formation, Baja California, Mexico. *Marine and Petroleum Geology*, *24*(6), 540–563.

Kastens, K. A., & Cita, M. B. (1981). Tsunami-induced sediment transport in the abyssal Mediterranean Sea. *GSA Bulletin*, *92*(11), 845–857.

Kneller, B. C., & McCaffrey, W. D. (2003). The Interpretation of Vertical Sequences in Turbidite Beds: The Influence of Longitudinal Flow Structure. *Journal of Sedimentary Research*, *73*(5), 706–713.

Konfirst, M. A., Kuhn, G., Monien, D., & Scherer, R. P. (2011). Correlation of Early Pliocene diatomite to low amplitude Milankovitch cycles in the ANDRILL AND-1B drill core. *Marine Micropaleontology*, *80*(3), 114–124.

Kontopoulos, N., & Avramidis, P. (2003). A late Holocene record of environmental changes from the Aliki lagoon, Egion, North Peloponnesus, Greece. *Quaternary International: The Journal of the International Union for Quaternary Research*, *111*(1), 75–90.

Kortekaas, S., Papadopoulos, G. A., Ganas, A., Cundy, A. B., & Diakantoni, A. (2011). Geological identification of historical tsunamis in the Gulf of Corinth, Central Greece. *Natural Hazards and Earth System Sciences*, *11*(7), 2029–2041.

Koukouvelas, I. K., Katsonopoulou, D., Soter, S., & Xypolias, P. (2005). Slip rates on the Helike Fault, Gulf of Corinth, Greece: new evidence from geoarchaeology. *Terra Nova*, *17*(2), 158–164.

Leeder, M. R., Portman, C., Andrews, J. E., Collier, R. E. L., Finch, E., Gawthorpe, R. L., McNeill, L. C., Pérez-Arlucea, M., & Rowe, P. (2005). Normal faulting and crustal deformation, Alkyonides Gulf and Perachora peninsula, eastern Gulf of Corinth rift, Greece. *Journal of the Geological Society*, *162*(3), 549–561.

Lemeille, F., Chatoupis, F., Foumelis, M., Rettenmaier, D., Unkel, I., Micarelli, L., Moretti, I., Bourdillon, C., Guernet, C., & Müller, C. (2004). Recent syn-rift deposits in the hangingwall of the Aigion Fault (Gulf of Corinth, Greece). *Comptes Rendus: Geoscience*, *336*(4), 425–434.

Lorenzoni, L., Benitez-Nelson, C. R., Thunell, R. C., Hollander, D., Varela, R., Astor, Y., Audemard, F. A., & Muller-Karger, F. E. (2012). Potential role of event-driven sediment transport on sediment accumulation in the Cariaco Basin, Venezuela. *Marine Geology*, *307-310*, 105–110.

Lowe, D. R. (1982). Sediment gravity flows; II, Depositional models with special reference to the deposits of high-density turbidity currents. *Journal of Sedimentary Research*, *52*(1), 279–297.

Lykousis, V., Roussakis, G., & Sakellariou, D. (2009). Slope failures and stability analysis of shallow water prodeltas in the active margins of Western Greece, northeastern Mediterranean Sea. *Geologische Rundschau: Zeitschrift Fur Allgemeine Geologie*, *98*(4), 807–822.

Lykousis, V., Sakellariou, D., Moretti, I., & Kaberi, H. (2007). Late Quaternary basin evolution of the Gulf of Corinth: Sequence stratigraphy, sedimentation, fault–slip and subsidence rates. *Tectonophysics*, *440*(1), 29–51.

Maffione, M., & Morris, A. (2017). The onset of fabric development in deep marine sediments. *Earth and Planetary Science Letters*, *474*, 32–39.

Marco, S., & Agnon, A. (1995). Prehistoric earthquake deformations near Masada, Dead Sea graben. *Geology*, *23*(8), 695–698.

McCalpin, J., 2009. Paleoseismology. 2nd Edition. *International Geophysics Series*, Elsevier, 95:1-613.

McHugh, C. M. G., Seeber, L., Cormier, M.-H., Dutton, J., Cagatay, N., Polonia, A., Ryan, W. B. F., & Gorur, N. (2006). Submarine earthquake geology along the North Anatolia Fault in the Marmara Sea, Turkey: A model for transform basin sedimentation. *Earth and Planetary Science Letters*, *248*(3), 661–684.

McHugh, C. M., Seeber, L., Braudy, N., Cormier, M.-H., Davis, M. B., Diebold, J. B., Dieudonne, N., Douilly, R., Gulick, S. P. S., Hornbach, M. J., Johnson, H. E., Mishkin, K. R., Sorlien, C. C., Steckler, M. S., Symithe, S. J., & Templeton, J. (2011). Offshore sedimentary effects of the 12 January 2010 Haiti earthquake. *Geology*, *39*(8), 723–726.

McHugh, C. M. G., Braudy, N., Çağatay, M. N., Sorlien, C., Cormier, M.-H., Seeber, L., & Henry, P. (2014). Seafloor fault ruptures along the North Anatolia Fault in the Marmara Sea, Turkey: Link with the adjacent basin turbidite record. *Marine Geology*, *353*, 65–83.

McHugh, C. M., Kanamatsu, T., Seeber, L., Bopp, R., Cormier, M.-H., & Usami, K. (2016). Remobilization of surficial slope sediment triggered by the A.D. 2011 Mw 9 Tohoku-Oki earthquake and tsunami along the Japan Trench. *Geology*, *44*(5), 391–394.

McNeill, L.C., Cotterill, C.J., Bull, J.M., Henstock, T.J., Bell, R., Stefatos, A., 2007. Geometry and slip rate of the Aigion fault, a young normal fault system in the western Gulf of Corinth. *Geology*, 35:355. doi.org/10.1130/G23281A.1.

McNeill, L. C., Shillington, D. J., & Carter, G. D. O. (2019a). Corinth Active Rift Development. *Proceedings of the International Ocean Discovery Program*, *381*. https://par.nsf.gov/biblio/10224878

McNeill, L. C., Shillington, D. J., Carter, G. D. O., Everest, J. D., Gawthorpe, R. L., Miller, C., Phillips, M. P., Collier, R. E. L., Cvetkoska, A., De Gelder, G., Diz, P., Doan, M.-L., Ford, M., Geraga, M., Gillespie, J., Hemelsdaël, R., Herrero-Bervera, E., Ismaiel, M., Janikian, L., … Green, S. (2019b). High-resolution record reveals climate-driven

environmental and sedimentary changes in an active rift. *Scientific Reports*, *9*(1), 6519.

Migeon, S., Weber, O., Faugeres, J.-C., & Saint-Paul, J. (1998). SCOPIX: A new X-ray imaging system for core analysis. *Geo-Marine Letters*, *18*(3), 251–255.

Moernaut, J., Van Daele, M., Strasser, M., Clare, M. A., Heirman, K., Viel, M., Cardenas, J., Kilian, R., Ladrón de Guevara, B., Pino, M., Urrutia, R., & De Batist, M. (2017). Lacustrine turbidites produced by surficial slope sediment remobilization: A mechanism for continuous and sensitive turbidite paleoseismic records. *Marine Geology*, *384*, 159–176.

Moretti, I., Lykousis, V., Sakellariou, D., Reynaud, J.-Y., Benziane, B., & Prinzhoffer, A. (2004). Sedimentation and subsidence rate in the Gulf of Corinth: what we learn from the Marion Dufresne's long-piston coring. *Comptes Rendus: Geoscience*, *336*(4), 291–299.

Mulder, T., & Syvitski, J. P. M. (1995). Turbidity Currents Generated at River Mouths during Exceptional Discharges to the World Oceans. *The Journal of Geology*, *103*(3), 285–299.

Mulder, T., Zaragosi, S., Razin, P., Grelaud, C., Lanfumey, V., & Bavoil, F. (2009). A new conceptual model for the deposition process of homogenite: Application to a cretaceous megaturbidite of the western Pyrenees (Basque region, SW France). *Sedimentary Geology*, *222*(3), 263–273.

Pallikarakis, A., Papanikolaou, I., Reicherter, K., Triantaphyllou, M., Dimiza, M., & Koukousioura, O. (2019). Constraining the regional uplift rate of the Corinth Isthmus area (Greece), through biostratigraphic and tectonic data. *Zeitschrift Für Geomorphologie Supplementary Issues*, *62*(2), 127–142.

Pantosti, D., De Martini, P. M., Koukouvelas, I., Stamatopoulos, L., Palyvos, N., Pucci, S., Lemeille, F., & Pavlides, S. (2004). Palaeoseismological investigations of the Aigion Fault (Gulf of Corinth, Greece). *Comptes Rendus: Geoscience*, *336*(4), 335–342.

Papadopoulos, G. A. (2000). *Historical earthquakes and tsunamis in the Corinth Rift, Central Greece*. Institute of Geodynamics.

Papadopoulos, G. A. (2003). Tsunami hazard in the Eastern Mediterranean: strong earthquakes and tsunamis in the Corinth Gulf, Central Greece. *Natural Hazards*, *29*(3), 437–464.

Papatheodorou, G., & Ferentinos, G. (1997). Submarine and coastal sediment failure triggered by the 1995, Ms = 6.1 R Aegion earthquake, Gulf of Corinth, Greece. *Marine Geology*, *137*(3-4), 287–304.

Papazachos, B. C., Comninakis, P. E., Karakaisis, G. F., Karakostas, B. G., Papaioannou, C. A., Papazachos, C. B., & Scordilis, E. M. (2000). A catalogue of earthquakes in Greece and surrounding area for the period 550BC-1999. *Publ. Geoph. Lab. , Univ. of Thessaloniki*, *1*, 333.

Passega, R. (1964). Grain size representation by CM patterns as a geologic tool. *Journal of Sedimentary Research*, *34*(4), 830–847.

Pechlivanidou, S., Cowie, P. A., Duclaux, G., Nixon, C. W., Gawthorpe, R. L., & Salles, T. (2019). Tipping the balance: Shifts in sediment production in an active rift setting. *Geology*, *47*(3), 259–262.

Pérouse, E., Chamot-Rooke, N., Rabaute, A., Briole, P., Jouanne, F., Georgiev, I., & Dimitrov, D. (2012). Bridging onshore and offshore present-day kinematics of central and eastern Mediterranean: Implications for crustal dynamics and mantle flow. *Geochemistry, Geophysics, Geosystems*, *13*(9). https://doi.org/10.1029/2012gc004289

Pickering, K. T., & Hiscott, R. N. (1985). Contained (reflected) turbidity currents from the Middle Ordovician Cloridorme Formation, Quebec, Canada: an alternative to the antidune hypothesis. *Sedimentology*, *32*(3), 373–394.

Polonia, A., Bonatti, E., Camerlenghi, A., Lucchi, R. G., Panieri, G., & Gasperini, L. (2013). Mediterranean megaturbidite triggered by the AD 365 Crete earthquake and tsunami. *Scientific Reports*, *3*, 1285.

Polonia, A., Nelson, C. H., Romano, S., Vaiani, S. C., Colizza, E., Gasparotto, G., & Gasperini, L. (2017). A depositional model for seismo-turbidites in confined basins based on Ionian Sea deposits. *Marine Geology*, *384*, 177–198.

Ratzov, G., Cattaneo, A., Babonneau, N., Deverchère, J., Yelles, K., Bracene, R., Courboulex, F., 2015. Holocene turbidites record earthquake supercycles at a slow-rate plate boundary. *Geology*, 43:331–334. doi.org/10.1130/G36170.1

Rigo, A., Lyon-Caen, H., Armijo, R., Deschamps, A., Hatzfeld, D., Makropoulos, K., Papadimitriou, P., & Kassaras, I. (1996). A microseismic study in the western part of the Gulf of Corinth (Greece): implications for large-scale normal faulting mechanisms. *Geophysical Journal International*, *126*(3), 663–688.

Rodríguez-Pascua, M. A., Calvo, J. P., De Vicente, G., & Gómez-Gras, D. (2000). Soft-sediment deformation structures interpreted as seismites in lacustrine sediments of the Prebetic Zone, SE Spain, and their potential use as indicators of earthquake magnitudes during the Late Miocene. *Sedimentary Geology*, *135*(1-4), 117–135.

Rothwell, R. G., & Croudace, I. w. (2015). Twenty Years of XRF Core Scanning Marine Sediments: What Do Geochemical Proxies Tell Us? In I. W. Croudace & R. G. Rothwell (Eds.), *Micro-XRF Studies of Sediment Cores: Applications of a non-destructive tool for the environmental sciences* (pp. 25–102). Springer Netherlands.

Rothwell, R. G., Hoogakker, B., Thomson, J., Croudace, I. W., & Frenz, M. (2006). Turbidite emplacement on the southern Balearic Abyssal Plain (western Mediterranean Sea) during Marine Isotope Stages 1--3: an application of ITRAX XRF scanning of sediment cores to lithostratigraphic analysis. *Geological Society, London, Special Publications*, *267*(1), 79–98.

San Pedro, L., Babonneau, N., Gutscher, M.-A., & Cattaneo, A. (2017). Origin and chronology of the Augias deposit in the Ionian Sea (Central Mediterranean Sea), based on new regional sedimentological data. *Marine Geology*, *384*, 199–213.

Siegenthaler, C., Finger, W., Kelts, K., & Wang, S. (1987). Earthquake and seiche deposits in Lake Lucerne, Switzerland. *Eclogae Geologicae Helvetiae*, *80*(1), 241–260.

Sinclair, H. D., & Cowie, P. A. (2003). Basin-floor topography and the scaling of turbidites. *The Journal of Geology*, *111*(3), 277–299.

Stanley, D. J. (1981). Unifites: structureless muds of gravity-flow origin in Mediterranean basins. *Geo-Marine Letters*, *1*(2), 77–83.

Stefatos, A., Charalambakis, M., Papatheodorou, G., & Ferentinos, G. (2006). Tsunamigenic sources in an active European half-graben (Gulf of Corinth, Central Greece). *Marine Geology*, *232*(1), 35–47.

Stevenson, C. J., Talling, P. J., Masson, D. G., Sumner, E. J., Frenz, M., & Wynn, R. B. (2014). The spatial and temporal distribution of grain-size breaks in turbidites. *Sedimentology*, *61*(4), 1120–1156.

Stow, D.A.V. (Ed.), 1992. Deep-water turbidite systems. *International Associations of Sedimentologists, Reprint Series* 3, Blackwell Sc. Publ., 473 pp.

Stow, D. A. V. & Wetzel, A., (1990). Hemiturbidite: a new type of deep-water sediment. *Proceedings of the Ocean Drilling Program, Scientific Results*, *116*, 25–34.

Sturm, M., Siegenthaler, C., & Pickrill, R. A. (1995). Turbidites and "homogenites"--a conceptual model of flood and slide deposits. *Publication of IAS-16th Regional Meeting Sedimentology, Paris*, *22*, 140.

Talling, P. J., Masson, D. G., Sumner, E. J., & Malgesini, G. (2012). Subaqueous sediment density flows: Depositional processes and deposit types. *Sedimentology*, *59*(7), 1937–2003.

Taylor, B., Weiss, J. R., Goodliffe, A. M., Sachpazi, M., Laigle, M., & Hirn, A. (2011). The structures, stratigraphy and evolution of the Gulf of Corinth rift, Greece. *Geophysical Journal International*, *185*(3), 1189–1219.

Thunell, R., Tappa, E., Varela, R., Llano, M., Astor, Y., Muller-Karger, F., & Bohrer, R. (1999). Increased marine sediment suspension and fluxes following an earthquake. *Nature*, *398*(6724), 233–236.

Van Daele, M., Moernaut, J., Doom, L., Boes, E., Fontijn, K., Heirman, K., Vandoorne, W., Hebbeln, D., Pino, M., Urrutia, R., Brümmer, R., & De Batist, M. (2015). A comparison of the sedimentary records of the 1960 and 2010 great Chilean earthquakes in 17 lakes: Implications for quantitative lacustrine palaeoseismology. *Sedimentology*, *62*(5), 1466–1496.

Van Daele, M., Meyer, I., Moernaut, J., De Decker, S., Verschuren, D., & De Batist, M. (2017). A revised classification and terminology for stacked and amalgamated turbidites in environments dominated by (hemi)pelagic sedimentation. *Sedimentary Geology*, *357*, 72–82.

Van Daele, M., Araya-Cornejo, M.C., Pille, T., Vanneste, K., Moernaut, J., Schmidt, S.,

Kempf, P., Meyer, I., and Cisternas, M., 2019. Distinguishing intraplate from megathrust earthquakes using lacustrine turbidites. *Geology*, v. 47, p. 127–130, doi.org/10.1130/G45662.1.

Vött, A., Hadler, H., & Koster, B. (2018). Returning to the facts: Response to the refusal of tsunami traces in the ancient harbour of Lechaion (Gulf of Corinth, Greece) by "non-catastrophists"–Reaffirmed …. *Zeitschrift Für Geomorphologie*. p. 275-302. DOI: 10.1127/zfg/2018/0519

Watkins, S.E., Whittaker, A.C., Bell, R.E., McNeill, L.C., Gawthorpe, R.L., Brooke, S.A.S., and Casey W. Nixon, C.W., 2019. Are landscapes buffered to high-frequency climate change? A comparison of sediment fluxes and depositional volumes in the Corinth Rift, central Greece, over the past 130 k.y. *Geological Society of America Bulletin*,131 (3-4): 372–388. https://doi.org/10.1130/B31953.1

Wils, K., Deprez, M., Kissel, C., Vervoort, M., Van Daele, M., Daryono, M. R., ... & De Batist, M. (2021). Earthquake doublet revealed by multiple pulses in lacustrine seismo-turbidites. *Geology*, *49*(11), 1301-1306.

Zavala, C., & Arcuri, M. (2016). Intrabasinal and extrabasinal turbidites: Origin and distinctive characteristics. *Sedimentary Geology*, *337*, 36–54.

Zavala, C., Arcuri, M., Di Meglio, M., Diaz, H. G., & Contreras, C. (2011). *A genetic facies tract for the analysis of sustained hyperpycnal flow deposits*. 31–51.

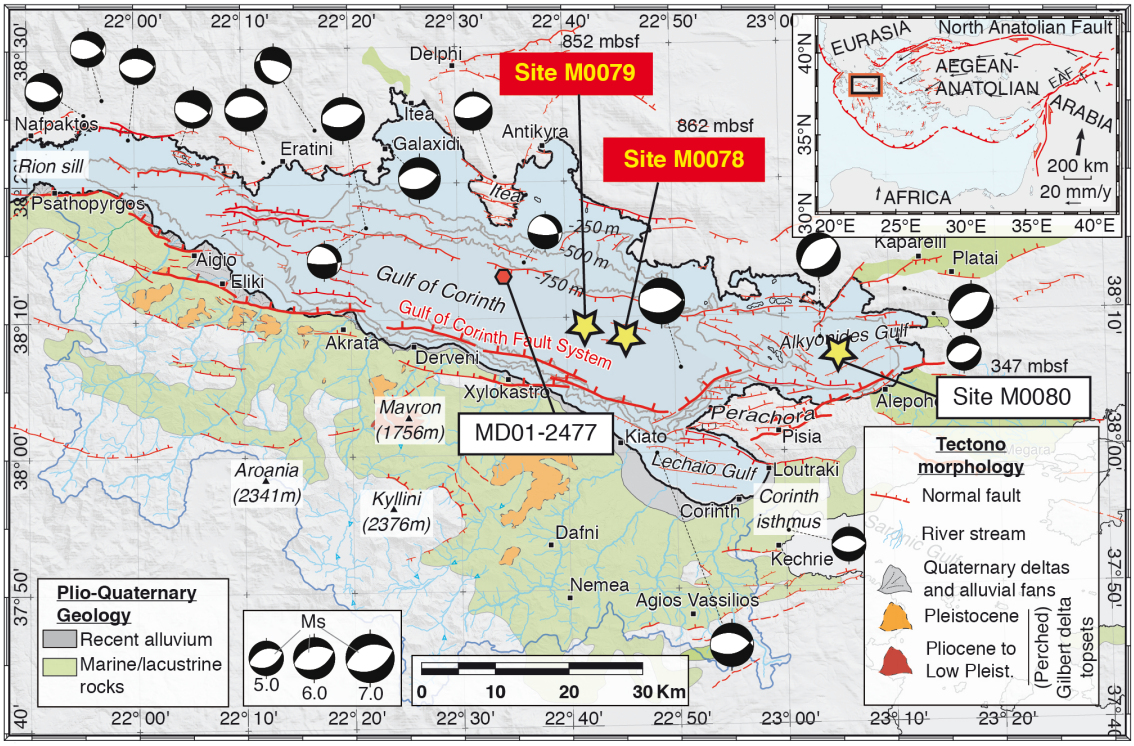

Figure 1: Location of studied coring sites in the Gulf of Corinth. Stars indicate IODP-381 coring sites, with samples from red sites used in this study. Bathymetry is shown with contours every 250 m, and faults are the major onshore and offshore active faults bounding the Corinth Rift. Fault thickness indicates relative fault importance, and inset shows tectonic setting. After Fernandez-Blanco et al. (2019a) and references therein.

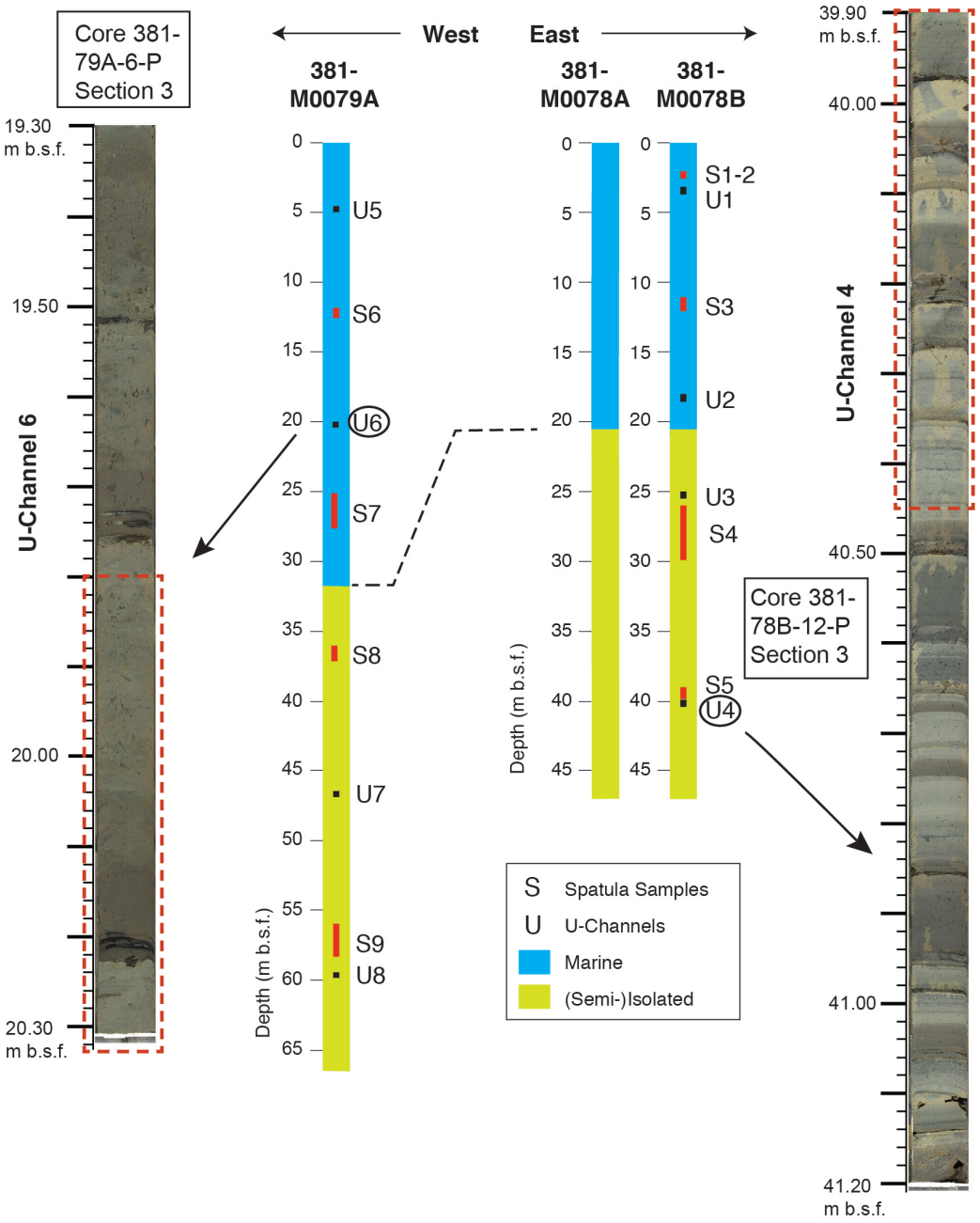

Figure 2: Location of different sampling within the last ~25 ka interval. View of split core sections that are presented in detail within the manuscript (Figs. 6 and 7).

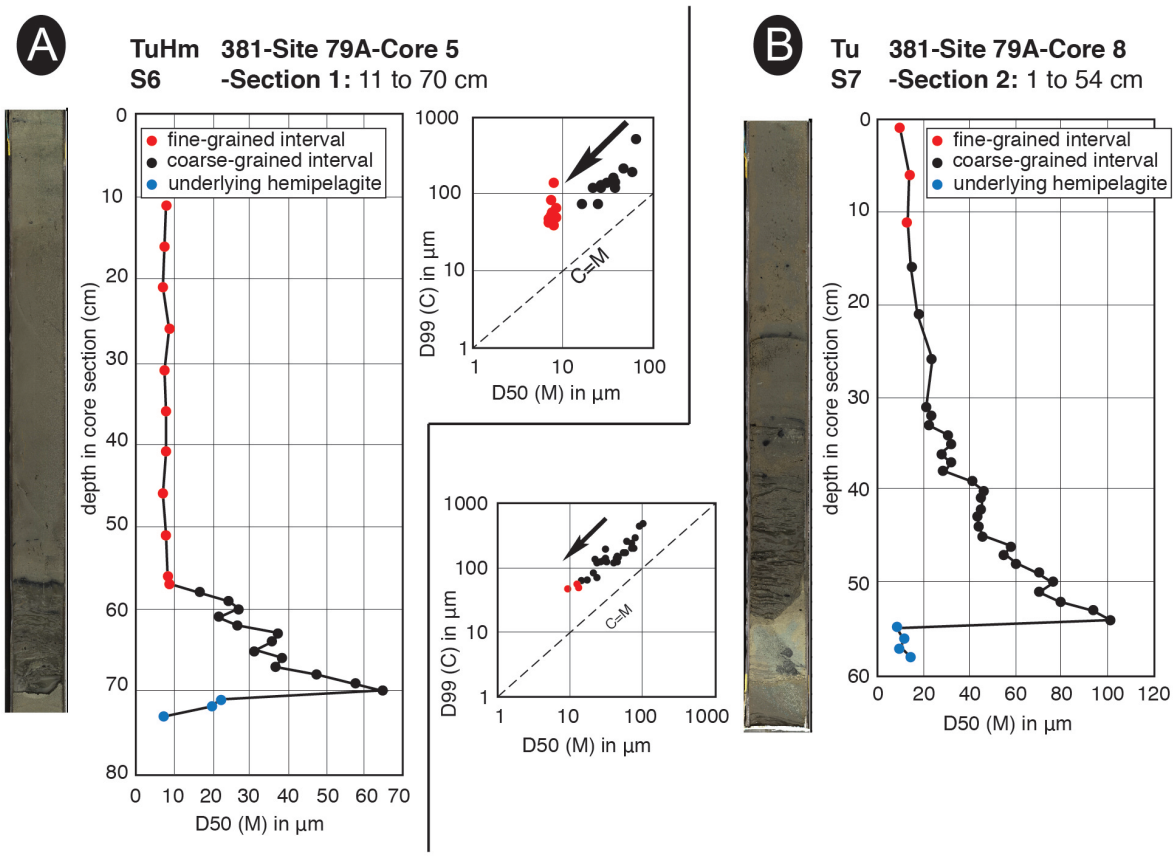

Figure 3: Selected examples of a single turbidite+homogenite (TuHm; left) and a "classical" turbidite (Tu; right). Base-to-top grain-size evolution is shown with D50 (Median or M), and Passega (1964)'s CM diagram combining the D50 (M) and the D99 (C) in logarithmic coordinates. Location of samples S6 and S7 is shown on Figure 2.

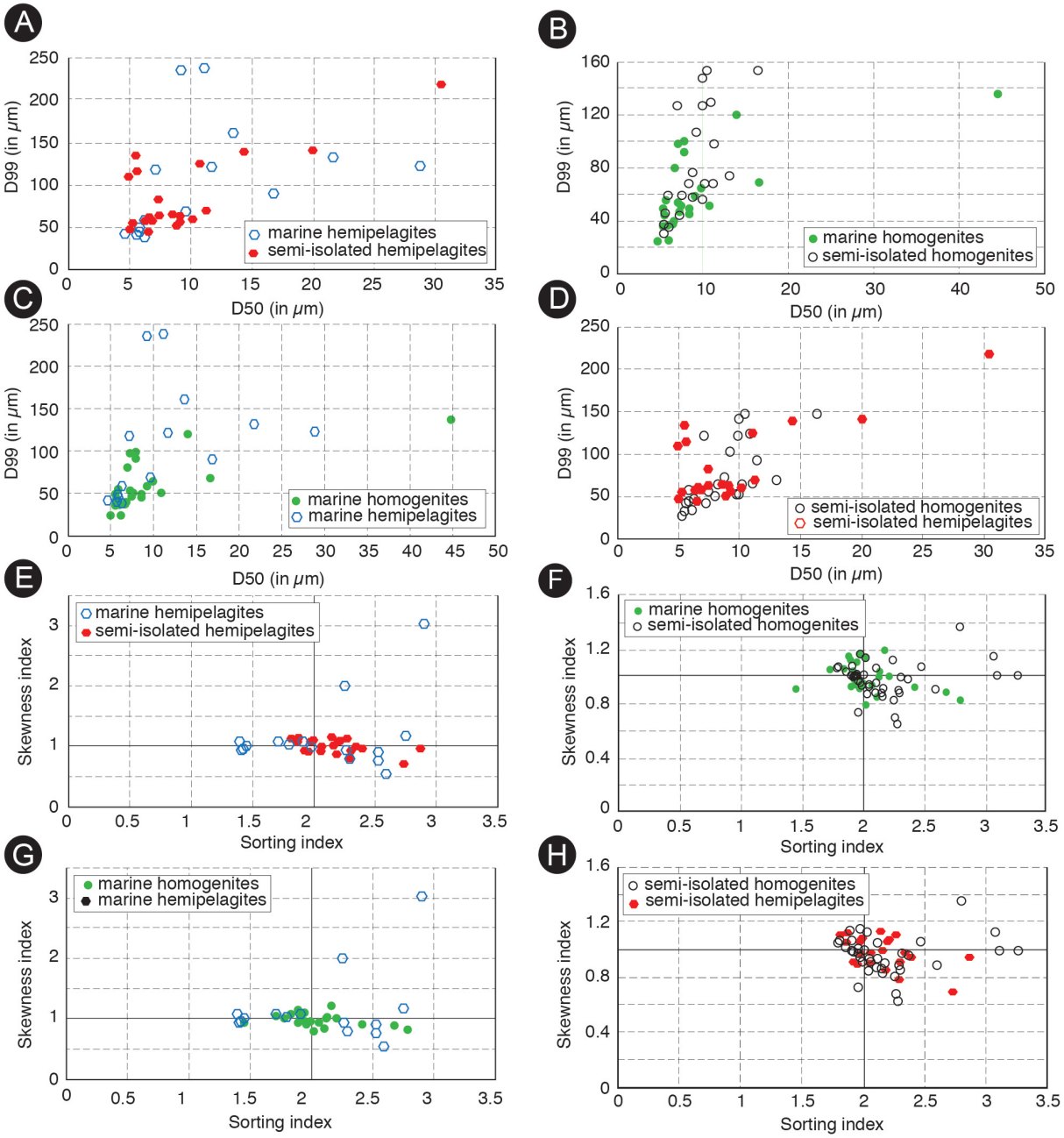

Figure 4: Binary cross-plots of grain-size parameters of hemipelagites and homogenites in marine and (semi-)isolated (SI) environments. Marine samples from U-channels 2, 5, and 6 (15 hemipelagite and 24 homogenite samples), SI samples from U-channels 3, 4, 7 and 8 (22 hemipelagite and 35 homogenite samples). Diagrams A to D display a general characterization through D50 (Median) and D99 (coarsest particles). Diagrams E to F are show depositional processes through classical Sorting and Skewness indices. Location of U-channels is shown on Figure 2.

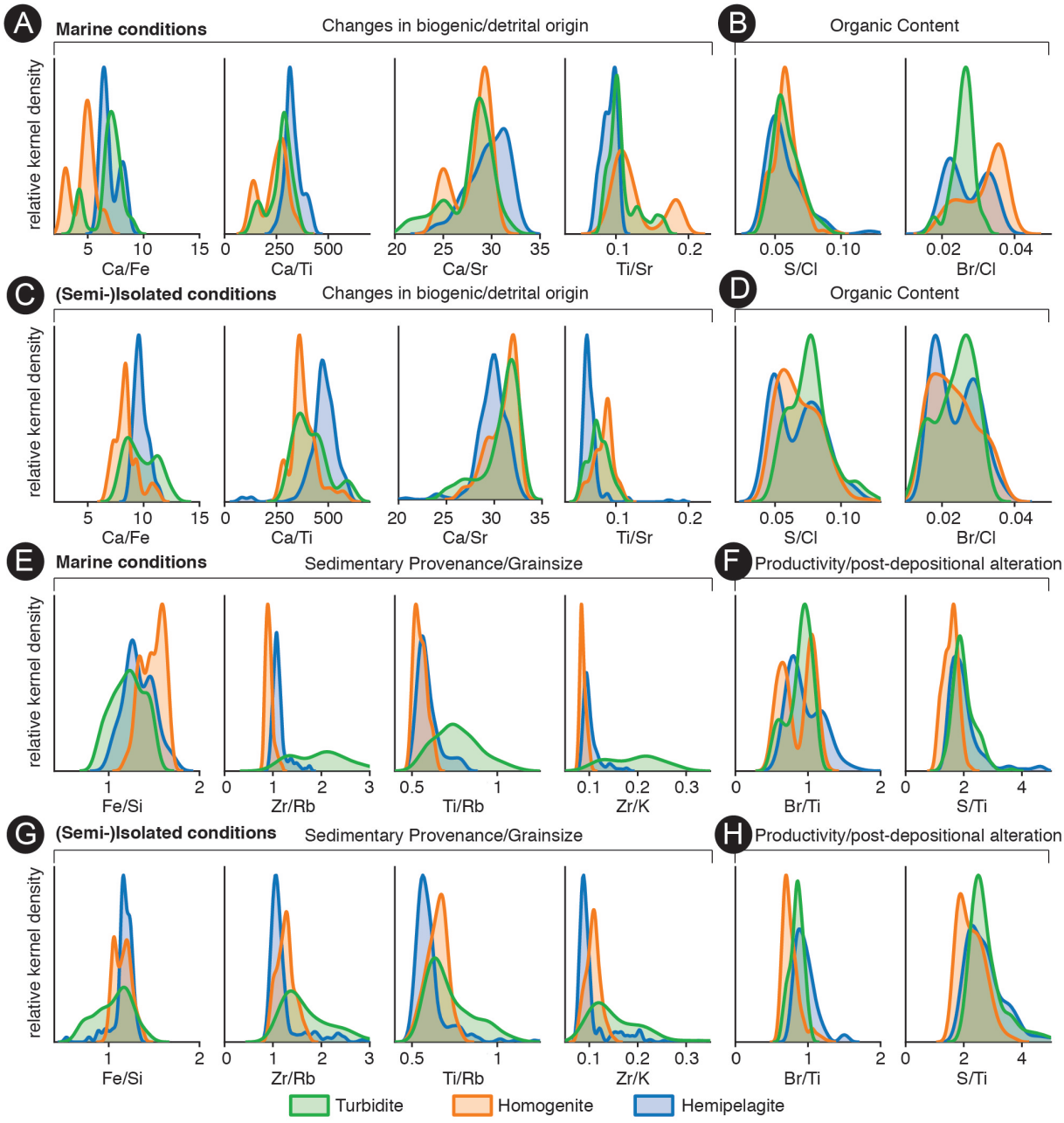

Figure 5: X-Ray Fluorescence (XRF) ratios for marine vs. (semi-)isolated (SI) conditions. Selection of 12 XRF ratios, distinguishing between Turbidites, Homogenites and Hemipelagites. Measurements come from all ten U-channels; values referred as "turbidites" come from classical turbidites (single Tu) and coarse bases of turbidites+homogenites (Tu term of TuHm).

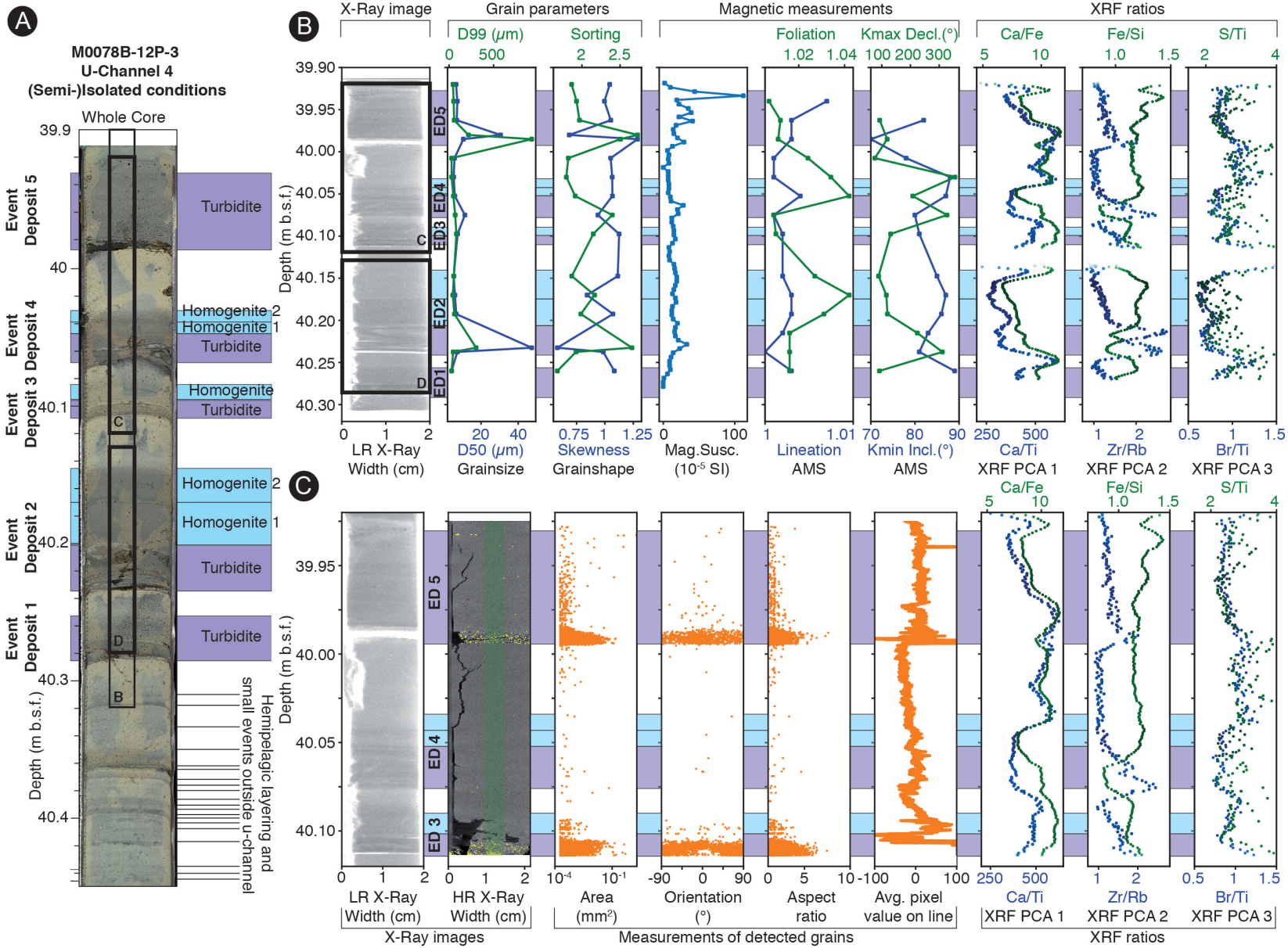
A
M0078B-12P-3
U-Channel 4
(Semi-)Isolated conditions
Whole Core
Depth (m b.s.f.)
Event Deposit 5
Event Deposit 4
Event Deposit 3
Event Deposit 2
Event Deposit 1
Turbidite
Homogenite 2
Homogenite 1
Homogenite
Hemipelagic layering and small events outside u-channel
B
X-Ray image
Grain parameters
Magnetic measurements
XRF ratios
D99 (μm)
Sorting
Foliation
Kmax Decl.(°)
Ca/Fe
Fe/Si
S/Ti
ED5
ED4
ED3
ED2
ED1
LR X-Ray Width (cm)
D50 (μm) Grainsize
Skewness Grainshape
Mag.Susc. (10-5 SI)
Lineation AMS
Kmin Incl.(°) AMS
Ca/Ti XRF PCA 1
Zr/Rb XRF PCA 2
Br/Ti XRF PCA 3
C
ED 5
ED 4
ED 3
HR X-Ray Width (cm)
Area (mm2)
Orientation (°)
Aspect ratio
Avg. pixel value on line
X-Ray images
Measurements of detected grains
XRF ratios

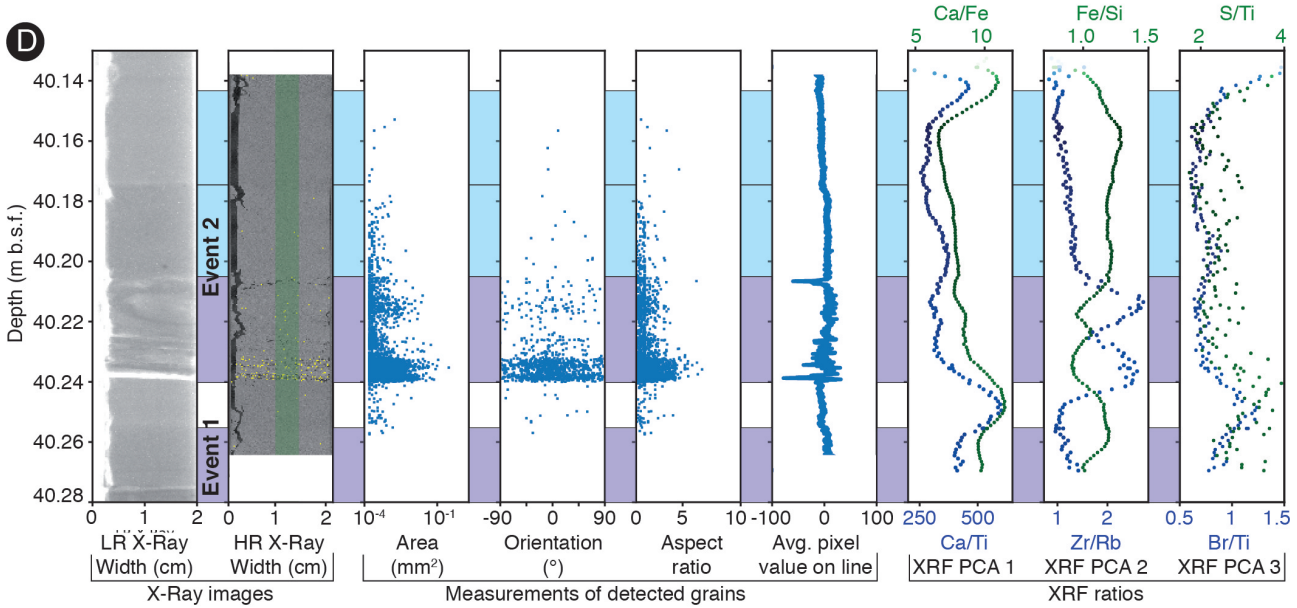

Figure 6: Overview of U-Channel 4 a) Whole core overview including position of u-channel and different event deposits. b) Low Resolution (LR) X-Ray image and measurements of U-Channel 4, including grainsize, grain shape, magnetic susceptibility, Anisotropy of Magnetic Susceptibility (AMS) and selected X-Ray Fluorescence (XRF) ratios for each of the three strongest Principal Components (see Fig. 5). c) Zoom-in on upper portion of U-Channel 4, including Low Resolution (LR) and High Resolution (HR) X-Ray images and measurements of area, orientation, and aspect of visible grains in HR X-Ray, average pixel value in HR X-Ray, and the same XRF ratios as in b. d) Same as in c, but for the lower portion of U-Channel 4.

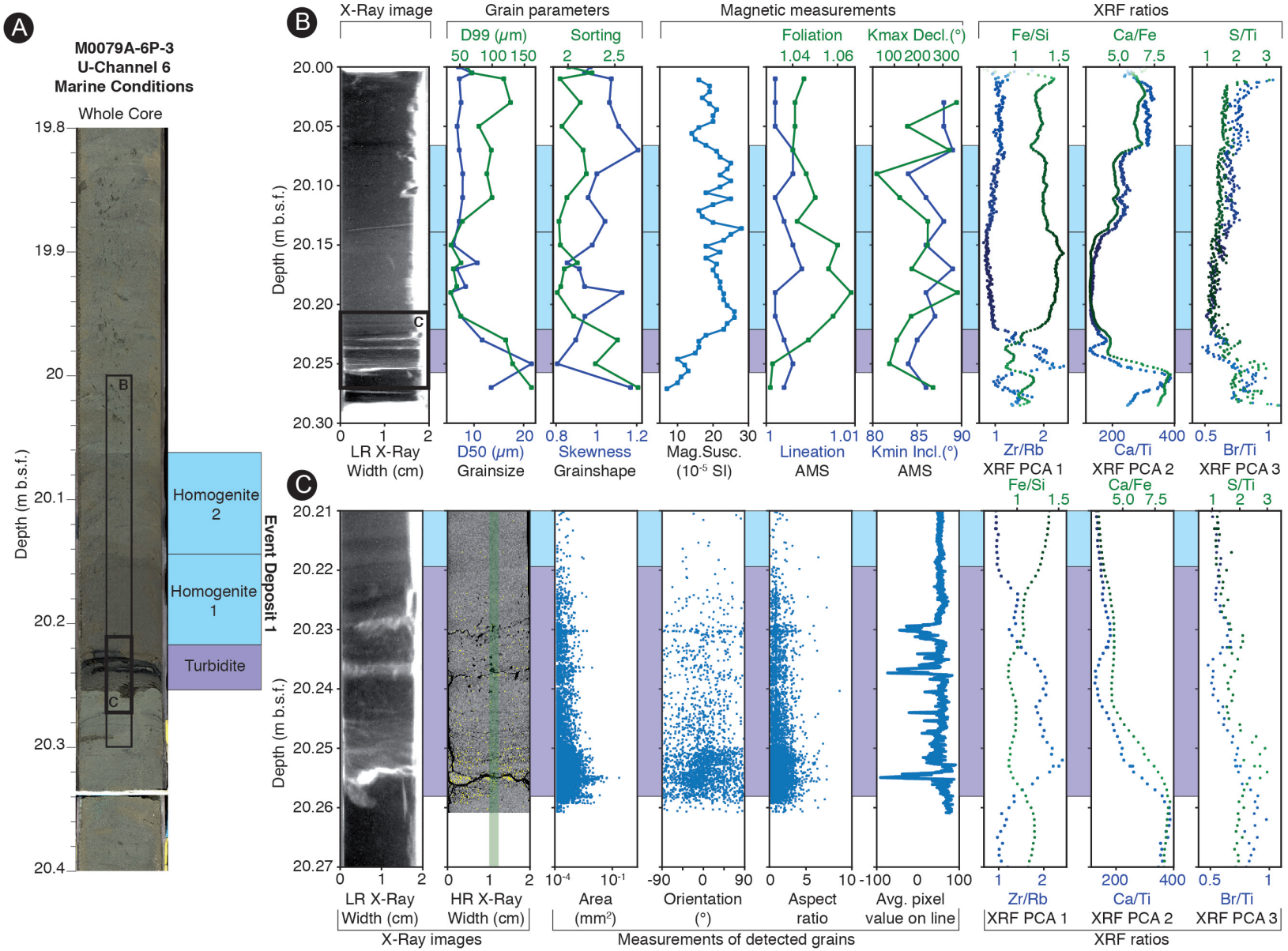

Figure 7: Overview of U-Channel 6. a) Whole core overview including position of U-channel 6 and different event deposits. b) Low Resolution (LR) X-Ray image and measurements of U-Channel 6, including grainsize, grain shape, magnetic susceptibility, Anisotropy of Magnetic Susceptibility (AMS) and selected X-Ray Fluorescence (XRF) ratios for each of the three strongest Principal Components (see Fig. 5). c) Zoom-in on turbidite interval of U-Channel 6, including Low Resolution (LR) and High Resolution (HR) X-Ray images and measurements of area, orientation, and aspect of visible grains in HR X-Ray, average pixel value in HR X-Ray, and the same XRF ratios as in b.

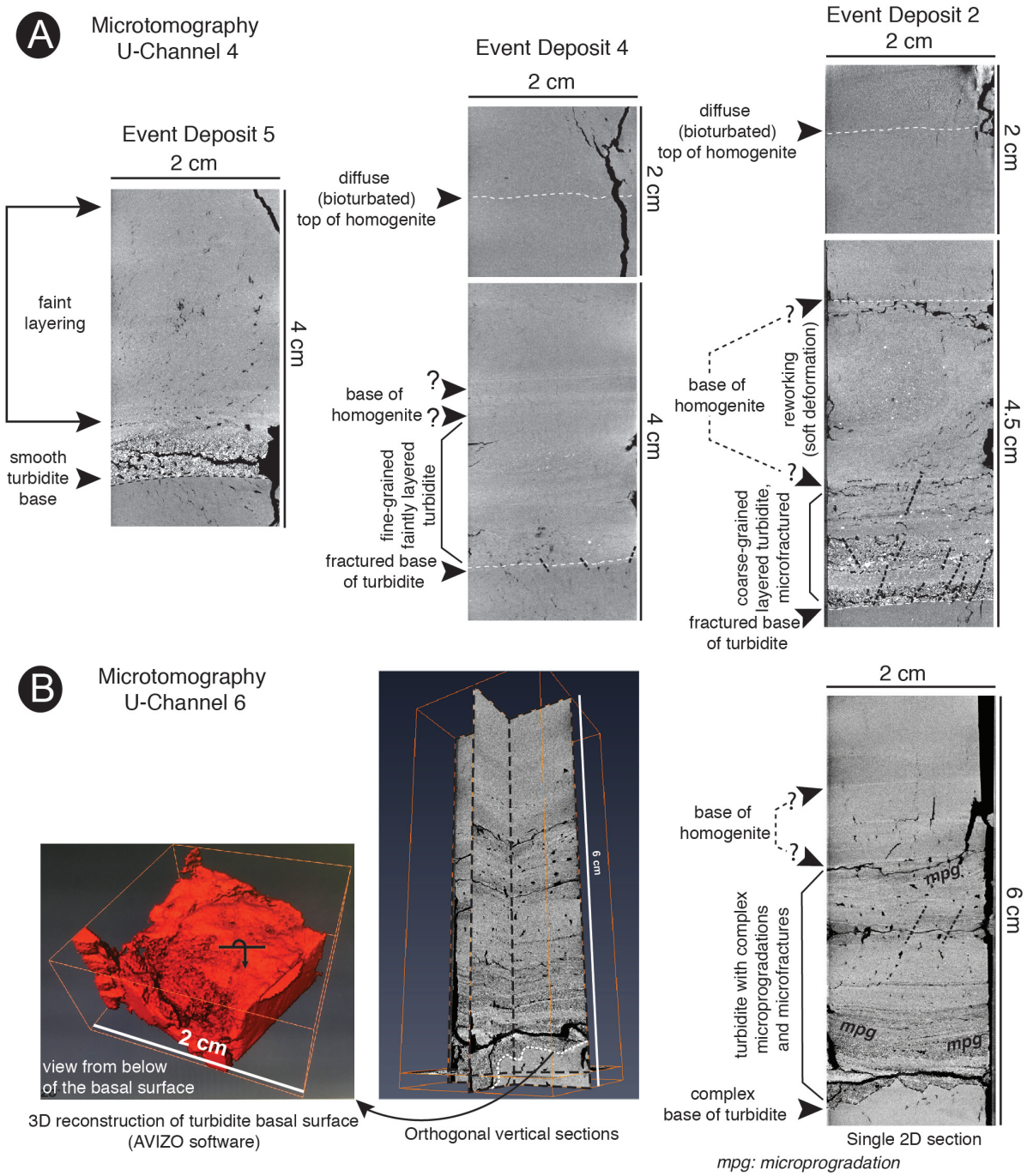

Figure 8: X-Ray Microtomography examples for U-Channels 4 and 6 a) 2D images of three sedimentary event deposits in U-Channel 4 (see position in Fig. 6). b) Images of the sedimentary event deposit in U-Channel 6 (same interval as Fig. 7c), including the 3D view of the basal turbidite surface (left), orthogonal sections of the imaged interval (middle) and a single 2D section (right). Microprograding (mpg) features are displayed in 2D; additional microtomographic data on U-channel 6 indicate they display opposite senses.

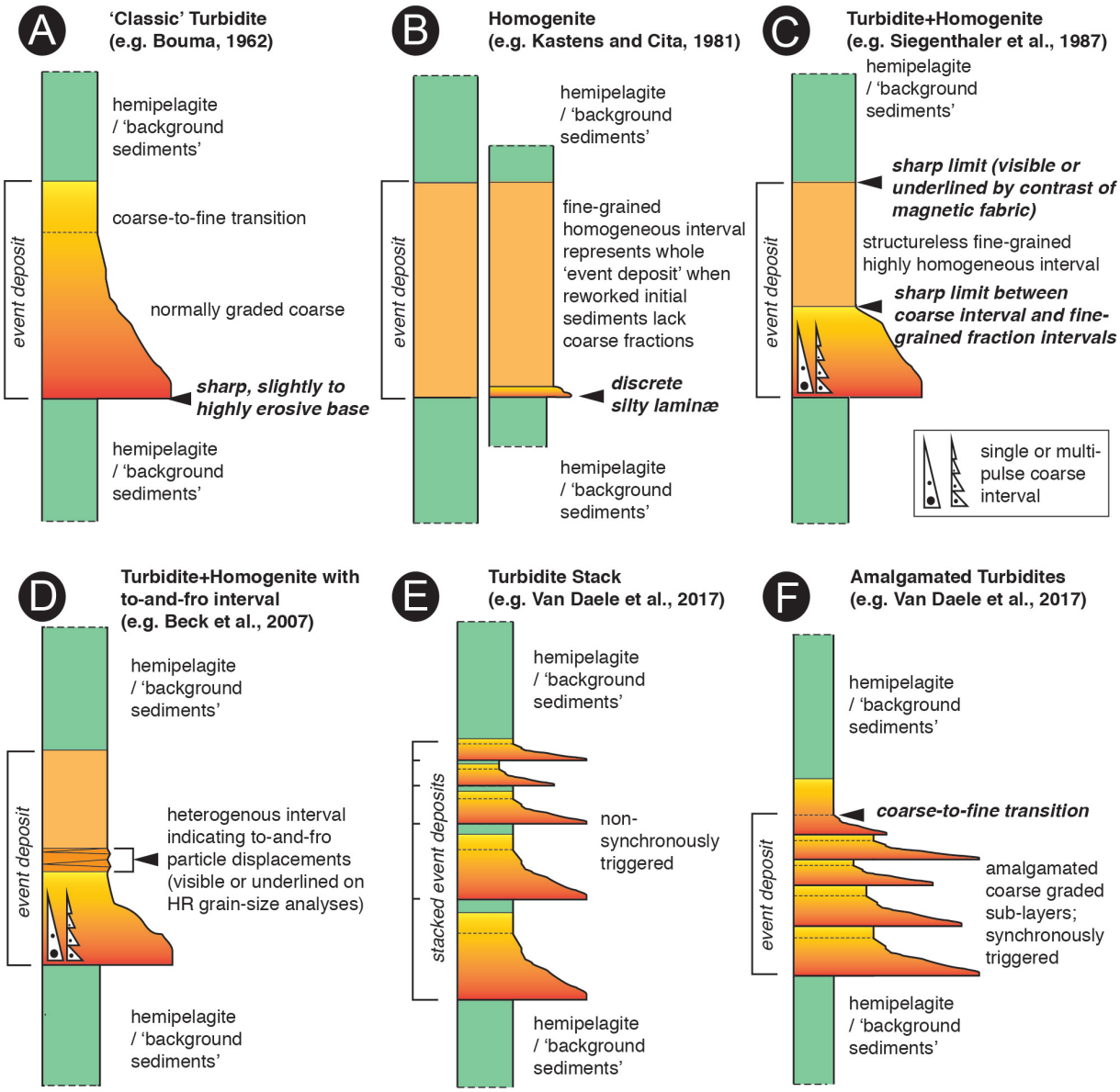

Figure 9: Schematic examples of sedimentary event deposits a) "classic" turbidites; b) homogenites; c) turbidite+homogenite; d) turbidite+homogenite with a to-and-fro interval; e) turbidite stack and f) amalgamated turbidites.

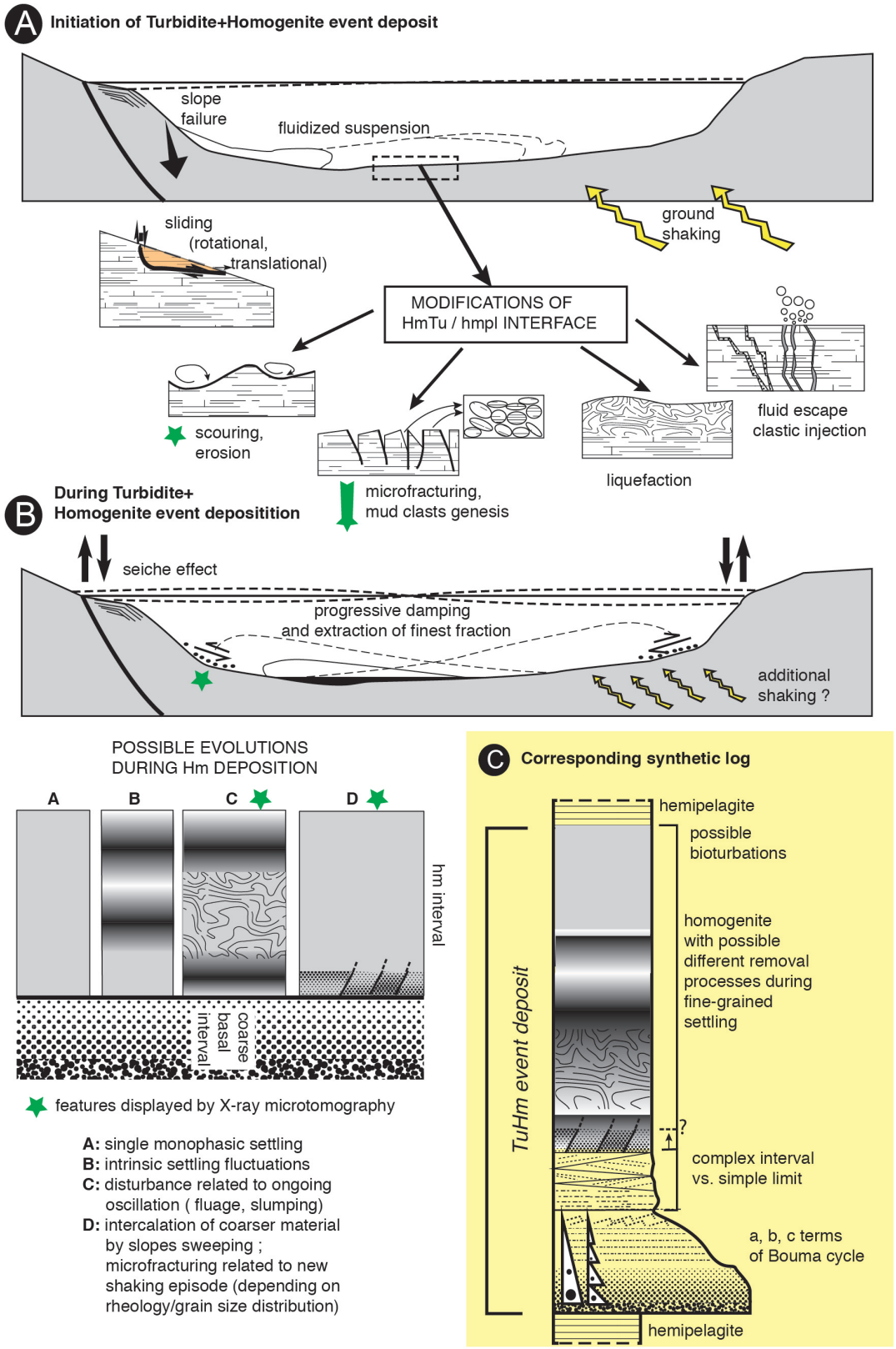

Figure 10: Explanatory model for TuHm event deposits from U-channels 4 and 6. a) initial triggering and different possible consequences: gravity reworking, water mass movement, and water/sediment interface disturbance; b) possible additional effects on settling due to internal (a-A and a-B cases) or external factors (a-C and a-D cases); c): conceptual model integrating the different inferred mechanisms. Green stars marks particularly well imaged features through X-ray microtomography. To simplify, only one gravity reworking site is represented, but several ones may occur simultaneously from different areas. Adapted from Chapron et al. (1999), Beck et al. (2007), Beck (2009), and completed.

Supporting Information for

Multi-scale and multi-parametric analysis of Late Quaternary event deposits within the active Corinth Rift (Greece)

Gino De Gelder[1,2], Mai Linh Doan[1], Christian Beck[3], Julie Carlut[2], Chloé Seibert[2], Nathalie Feuillet[2], Gareth D.O. Carter[4], Sofia Pechlivanidou[5], Robert L. Gawthorpe[5]

[1]ISTerre, Université Grenoble-Alpes, 1381 rue de la Piscine, 38400 Saint Martin d'Hères, France, [2]Université de Paris, Institut de Physique du Globe de Paris, CNRS, F-75005 Paris, France, [3]ISTerre, Université Savoie-Mont-Blanc, Campus Scientifique, 73376 Le Bourget-du-Lac Cedex, France, [4]British Geological Survey, The Lyell Centre, Research Avenue South, Edinburgh, EH14 4AP, United Kingdom, [5]Department of Earth Science, University of Bergen, Postboks 7803 NO-5020 Bergen, Norway

Contents of this file

Introduction

Supplementary Fig. 1 shows Principal Component Analysis results of 24 selected XRF ratios (see Methods), whereas Supplementary Fig. 2 shows XRF counts of specific elements. Supplementary Fig. 3 and 4 show XRF, grainsize/-shape, magnetic and microtomography analyses of U-channels not presented in the main paper, and Supplementary Fig. 5 additional microtomographic images of U-channels 2 and 8. Supplementary Fig. 6 gives all microtomographic images without any interpretation. Supplementary Table 1 gives an overview of observations and interpretations of the sedimentary events in all u-channels.

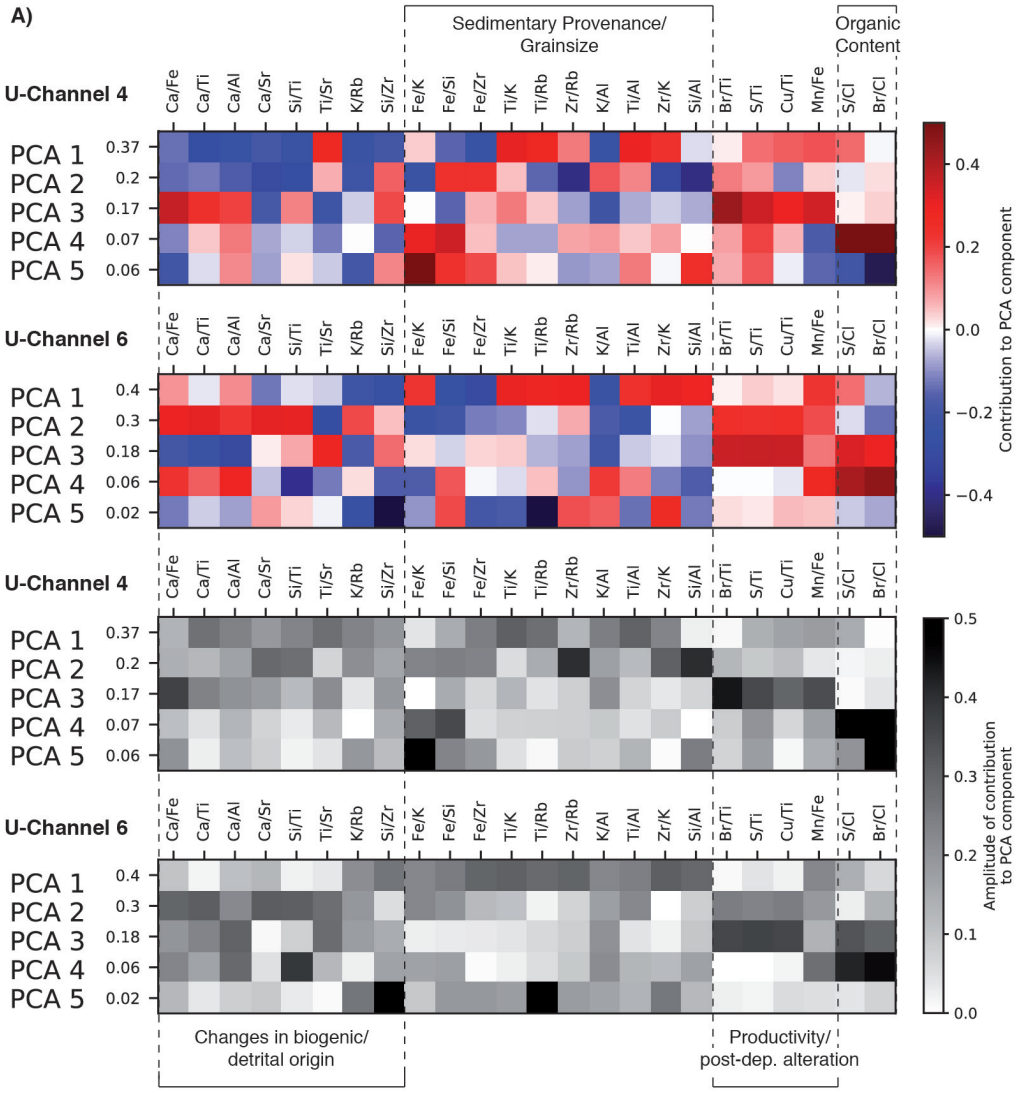

Supplementary Figure 1: X-Ray Fluorescence (XRF) Principal Component Analysis of U-Channels. Showing the first 5 Principal Components and the normalized weight of each component for 24 XRF ratios, for **a)** U-Channels 4 and 6, both in color code and black/white **b)** U-Channels 1, 2, 3, 7, 8 in color code and **c)** in black/white

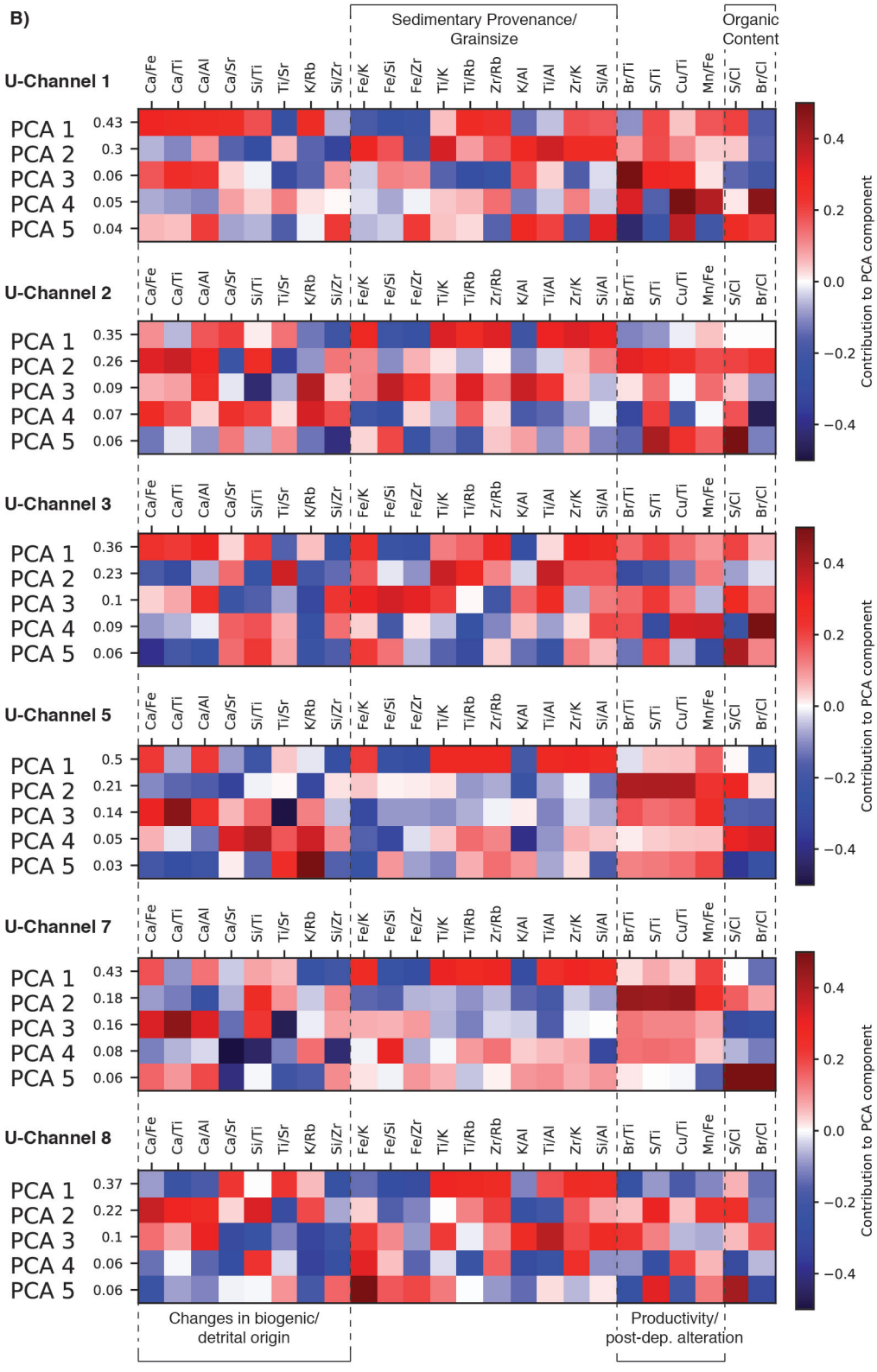
B)
Sedimentary Provenance/ Grainsize
Organic Content
Ca/Fe
Ca/Ti
Ca/Al
Ca/Sr
Si/Ti
Ti/Sr
K/Rb
Si/Zr
Fe/K
Fe/Si
Fe/Zr
Ti/K
Ti/Rb
Zr/Rb
K/Al
Ti/Al
Zr/K
Si/Al
Br/Ti
S/Ti
Cu/Ti
Mn/Fe
S/Cl
Br/Cl
U-Channel 1
PCA 1 0.43
PCA 2 0.3
PCA 3 0.06
PCA 4 0.05
PCA 5 0.04
U-Channel 2
PCA 1 0.35
PCA 2 0.26
PCA 3 0.09
PCA 4 0.07
PCA 5 0.06
U-Channel 3
PCA 1 0.36
PCA 2 0.23
PCA 3 0.1
PCA 4 0.09
PCA 5 0.06
U-Channel 5
PCA 1 0.5
PCA 2 0.21
PCA 3 0.14
PCA 4 0.05
PCA 5 0.03
U-Channel 7
PCA 1 0.43
PCA 2 0.18
PCA 3 0.16
PCA 4 0.08
PCA 5 0.06
U-Channel 8
PCA 1 0.37
PCA 2 0.22
PCA 3 0.1
PCA 4 0.06
PCA 5 0.06
0.4
0.2
0.0
−0.2
−0.4
Contribution to PCA component
Changes in biogenic/ detrital origin
Productivity/ post-dep. alteration

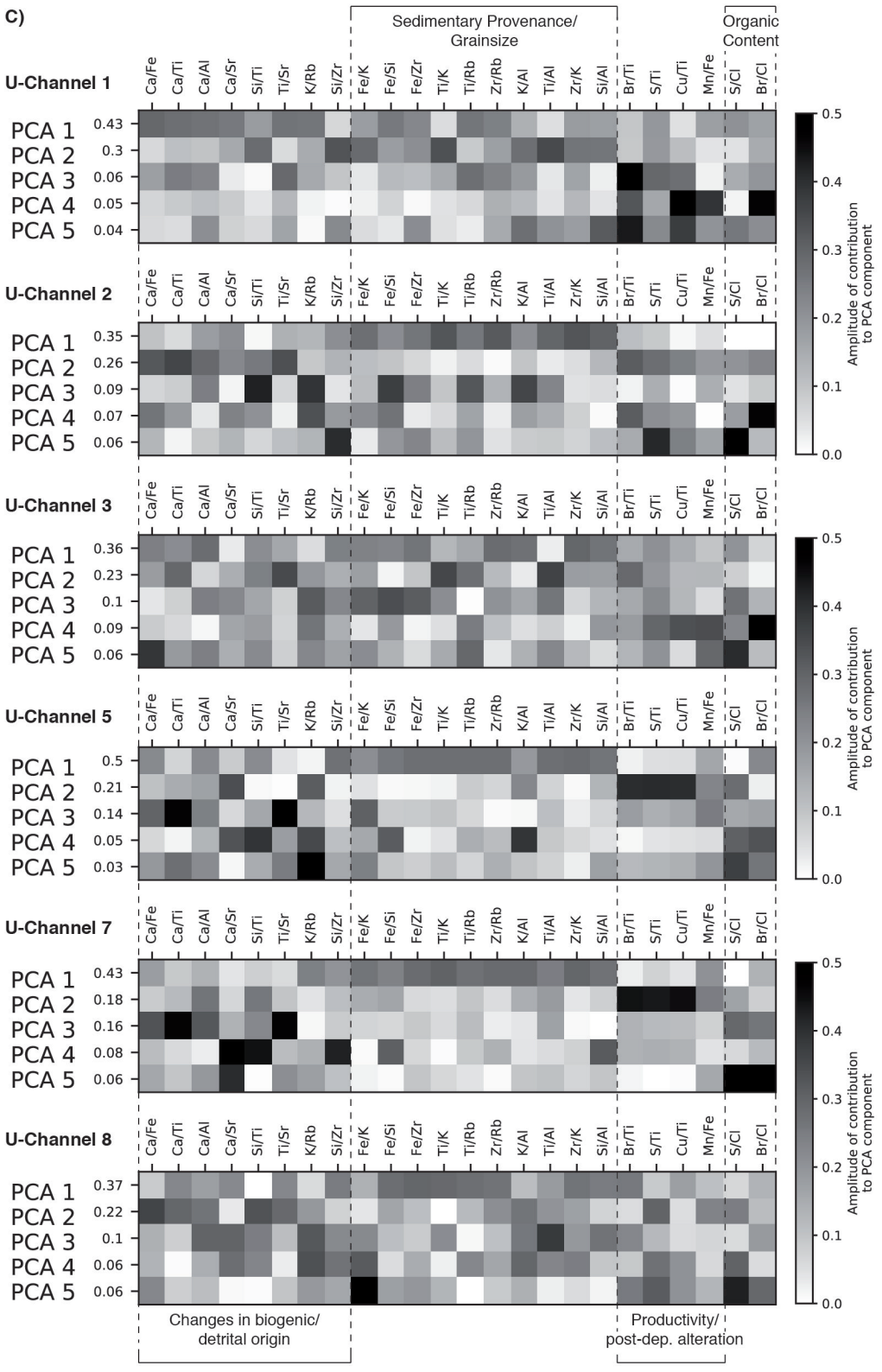
C)
Sedimentary Provenance/ Grainsize
Organic Content
Ca/Fe
Ca/Ti
Ca/Al
Ca/Sr
Si/Ti
Ti/Sr
K/Rb
Si/Zr
Fe/K
Fe/Si
Fe/Zr
Ti/K
Ti/Rb
Zr/Rb
K/Al
Ti/Al
Zr/K
Si/Al
Br/Ti
S/Ti
Cu/Ti
Mn/Fe
S/Cl
Br/Cl
U-Channel 1
PCA 1 0.43
PCA 2 0.3
PCA 3 0.06
PCA 4 0.05
PCA 5 0.04
U-Channel 2
PCA 1 0.35
PCA 2 0.26
PCA 3 0.09
PCA 4 0.07
PCA 5 0.06
U-Channel 3
PCA 1 0.36
PCA 2 0.23
PCA 3 0.1
PCA 4 0.09
PCA 5 0.06
U-Channel 5
PCA 1 0.5
PCA 2 0.21
PCA 3 0.14
PCA 4 0.05
PCA 5 0.03
U-Channel 7
PCA 1 0.43
PCA 2 0.18
PCA 3 0.16
PCA 4 0.08
PCA 5 0.06
U-Channel 8
PCA 1 0.37
PCA 2 0.22
PCA 3 0.1
PCA 4 0.06
PCA 5 0.06
Amplitude of contribution to PCA component
0.0
0.1
0.2
0.3
0.4
0.5
Changes in biogenic/ detrital origin
Productivity/ post-dep. alteration

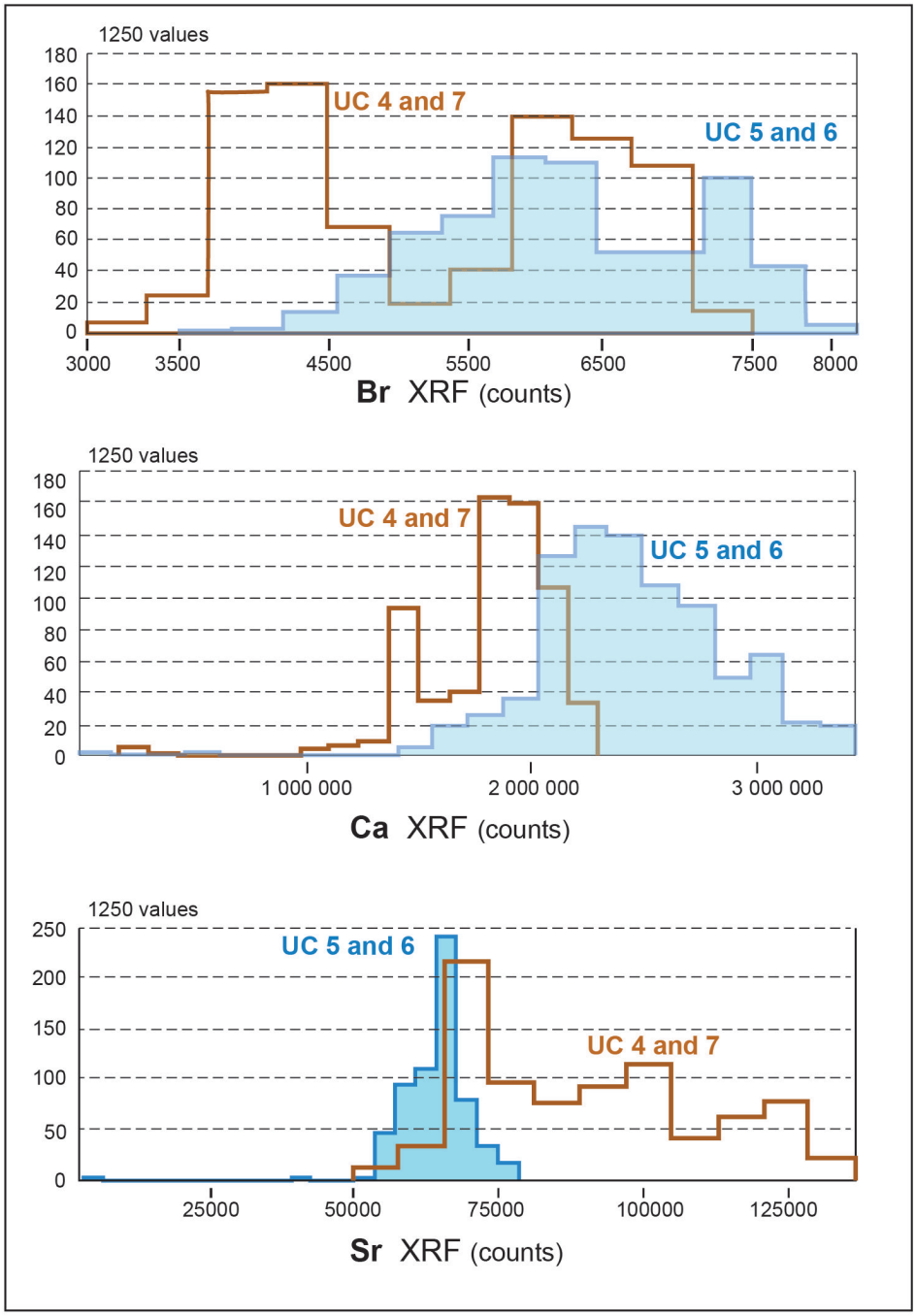

Supplementary Figure 2: Compared distribution of XRF Ca, Br, Sr counts within marine and (semi-)isolated U-channels. U-channels 5 and 6 representing marine conditions, and U-channels 4 and 7 representing (semi-)isolated conditions.

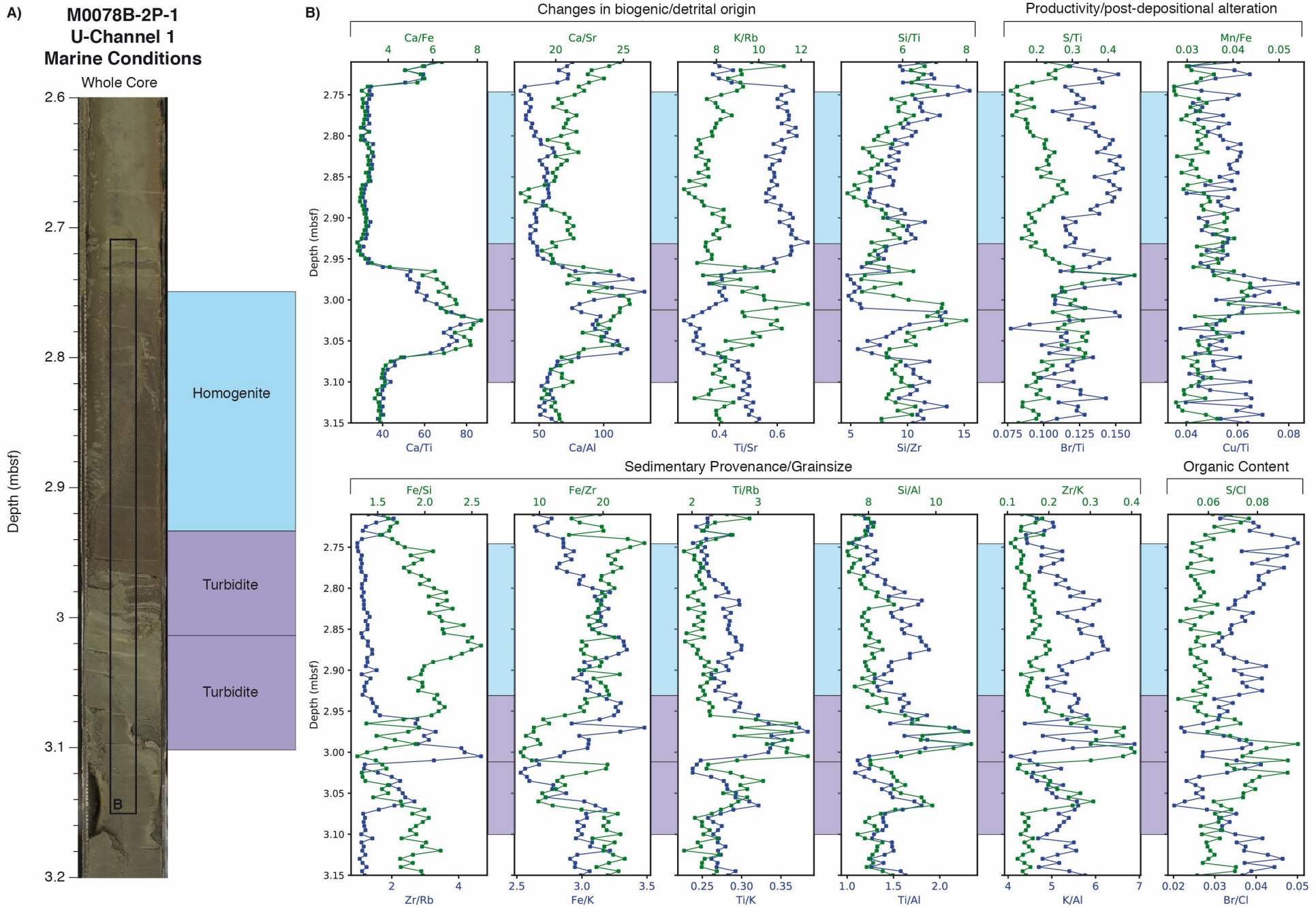

Supplementary Figure 3: X-Ray Fluorescence (XRF) ratios for all U-Channels (8 pages). Selection of 24 XRF ratios, measured on the whole core at 5 mm resolution for U-Channels 1, 2, 3, 8 and measured on the u-channel at 1 mm resolution for U-Channels 4, 5, 6 and 7

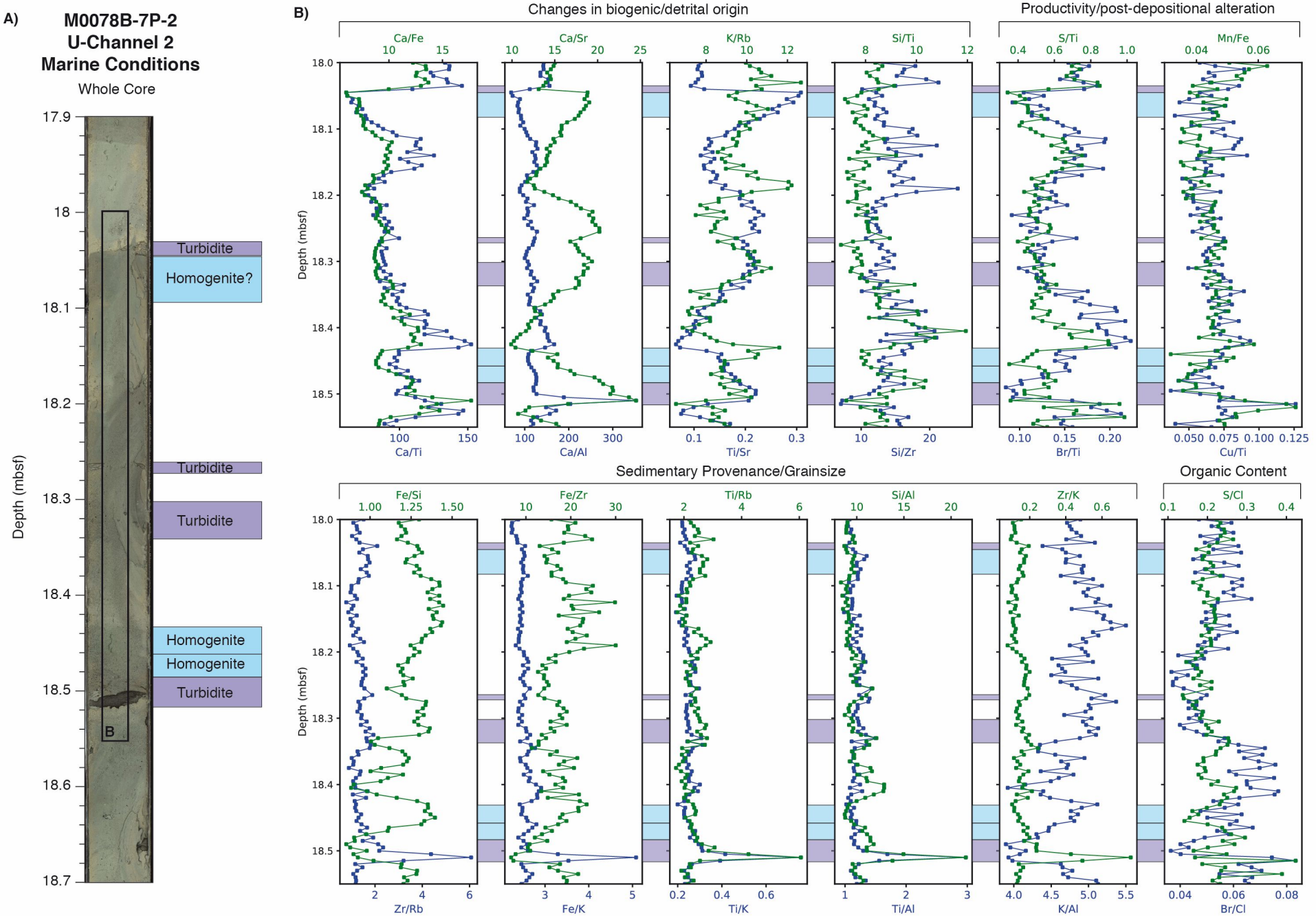
A)
M0078B-7P-2
U-Channel 2
Marine Conditions
Whole Core
Depth (mbsf)
17.9
18
18.1
18.2
18.3
18.4
18.5
18.6
18.7
Turbidite
Homogenite?
Turbidite
Turbidite
Homogenite
Homogenite
Turbidite
B
B)
Changes in biogenic/detrital origin
Productivity/post-depositional alteration
Ca/Fe
Ca/Sr
K/Rb
Si/Ti
S/Ti
Mn/Fe
Ca/Ti
Ca/Al
Ti/Sr
Si/Zr
Br/Ti
Cu/Ti
Sedimentary Provenance/Grainsize
Organic Content
Fe/Si
Fe/Zr
Ti/Rb
Si/Al
Zr/K
S/Cl
Zr/Rb
Fe/K
Ti/K
Ti/Al
K/Al
Br/Cl

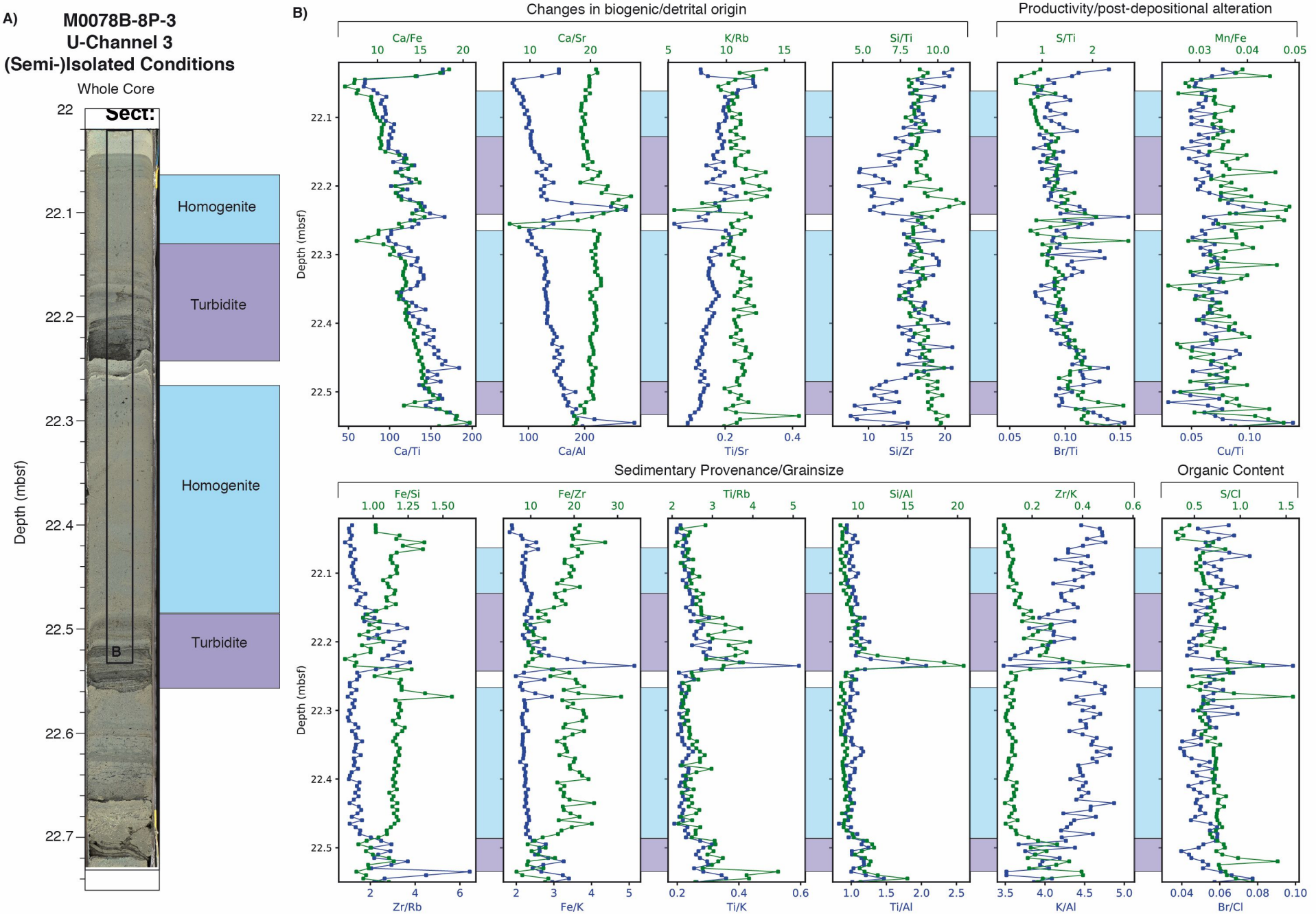
A)
M0078B-8P-3
U-Channel 3
(Semi-)Isolated Conditions
Whole Core
Sect:
Homogenite
Turbidite
Homogenite
Turbidite
B
Depth (mbsf)
B)
Changes in biogenic/detrital origin
Productivity/post-depositional alteration
Ca/Fe
Ca/Sr
K/Rb
Si/Ti
S/Ti
Mn/Fe
Ca/Ti
Ca/Al
Ti/Sr
Si/Zr
Br/Ti
Cu/Ti
Sedimentary Provenance/Grainsize
Organic Content
Fe/Si
Fe/Zr
Ti/Rb
Si/Al
Zr/K
S/Cl
Zr/Rb
Fe/K
Ti/K
Ti/Al
K/Al
Br/Cl

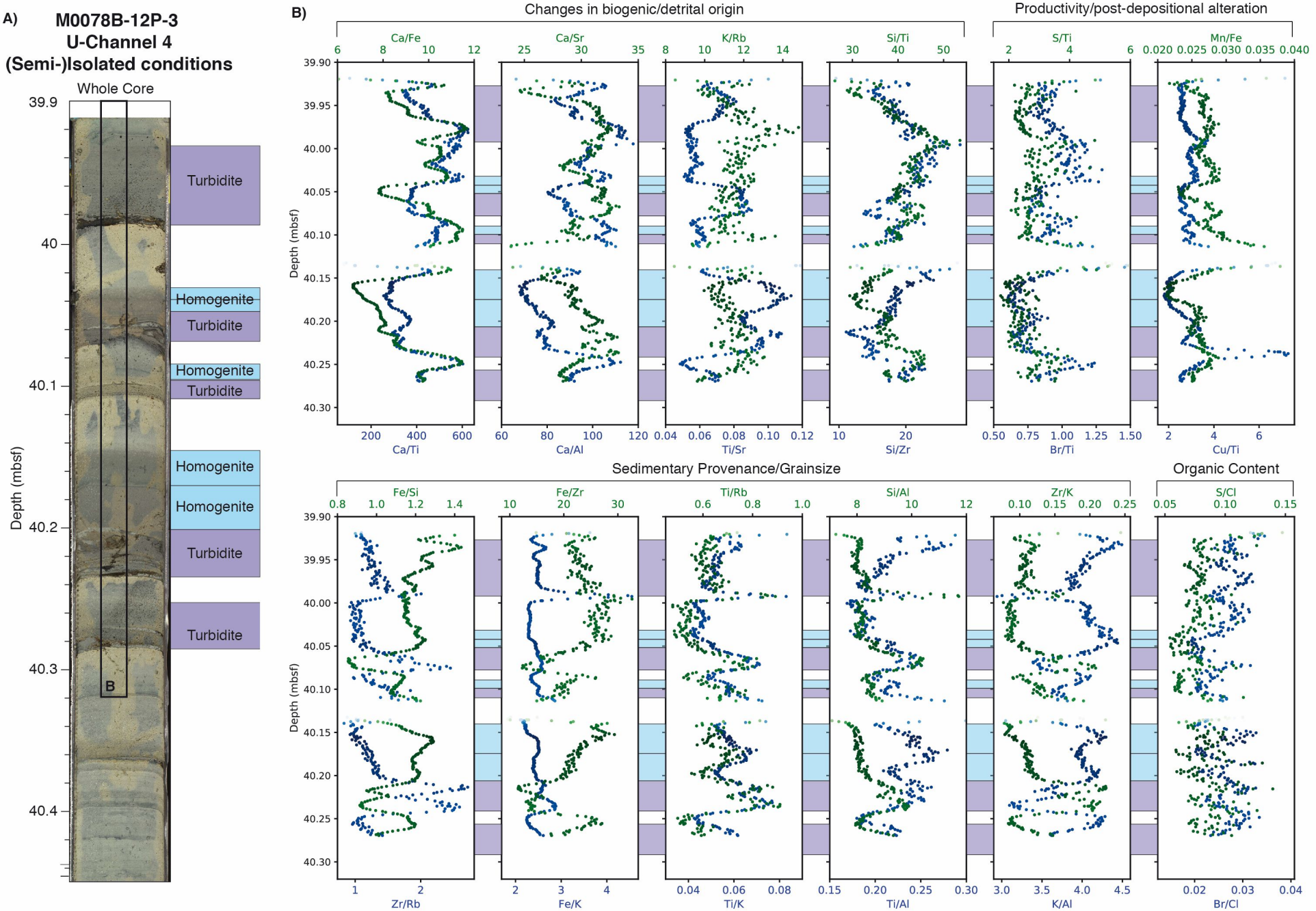
A)
M0078B-12P-3
U-Channel 4
(Semi-)Isolated conditions
Whole Core
Depth (mbsf)
39.9
40
40.1
40.2
40.3
40.4
Turbidite
Homogenite
Turbidite
Homogenite
Turbidite
Homogenite
Homogenite
Turbidite
Turbidite
B
B)
Changes in biogenic/detrital origin
Productivity/post-depositional alteration
Ca/Fe
Ca/Sr
K/Rb
Si/Ti
S/Ti
Mn/Fe
Ca/Ti
Ca/Al
Ti/Sr
Si/Zr
Br/Ti
Cu/Ti
Sedimentary Provenance/Grainsize
Organic Content
Fe/Si
Fe/Zr
Ti/Rb
Si/Al
Zr/K
S/Cl
Zr/Rb
Fe/K
Ti/K
Ti/Al
K/Al
Br/Cl

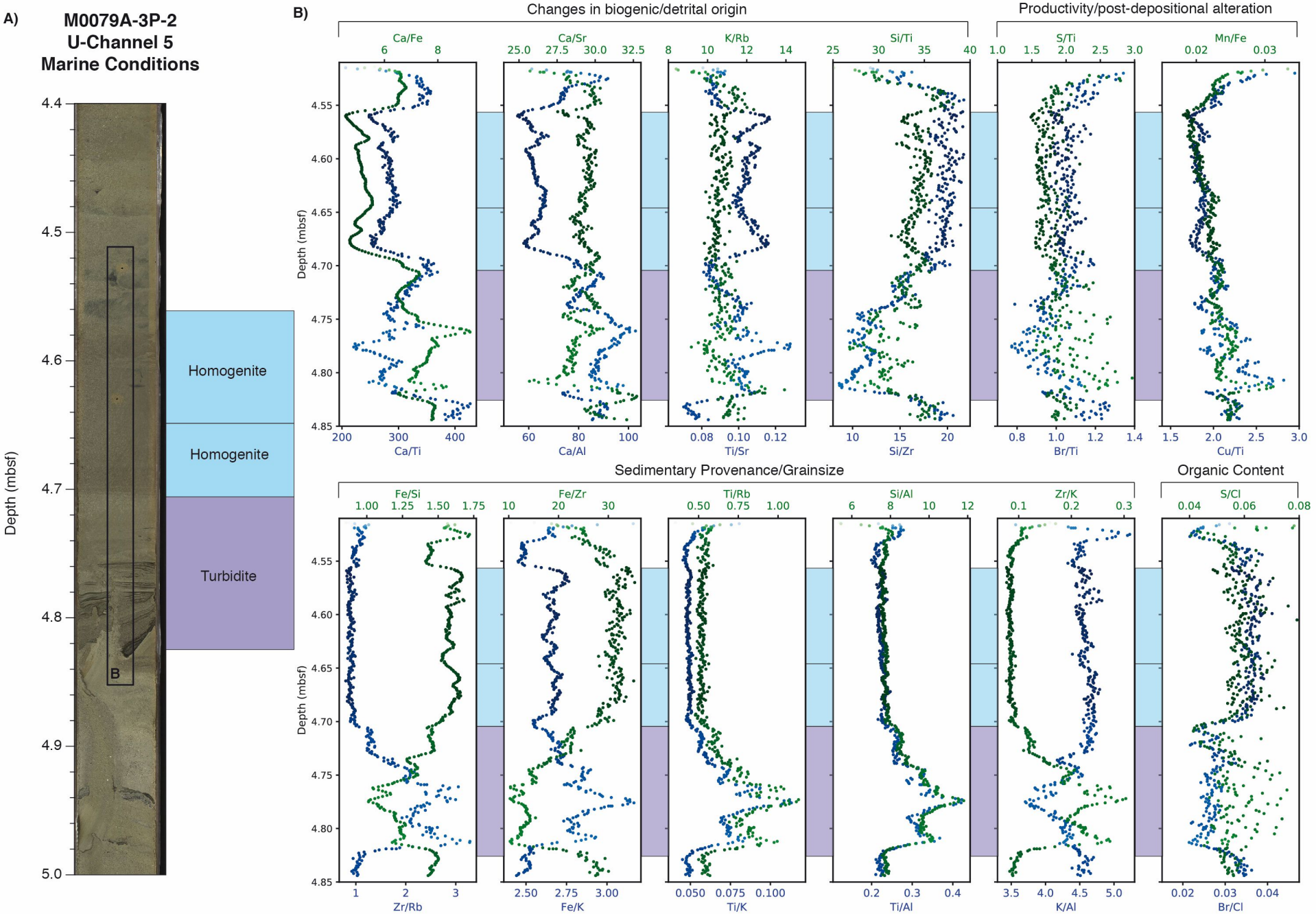
A)
M0079A-3P-2
U-Channel 5
Marine Conditions
Depth (mbsf)
4.4
4.5
4.6
4.7
4.8
4.9
5.0
B
Homogenite
Homogenite
Turbidite
B)
Changes in biogenic/detrital origin
Productivity/post-depositional alteration
Ca/Fe
Ca/Sr
K/Rb
Si/Ti
S/Ti
Mn/Fe
Ca/Ti
Ca/Al
Ti/Sr
Si/Zr
Br/Ti
Cu/Ti
Sedimentary Provenance/Grainsize
Organic Content
Fe/Si
Fe/Zr
Ti/Rb
Si/Al
Zr/K
S/Cl
Zr/Rb
Fe/K
Ti/K
Ti/Al
K/Al
Br/Cl

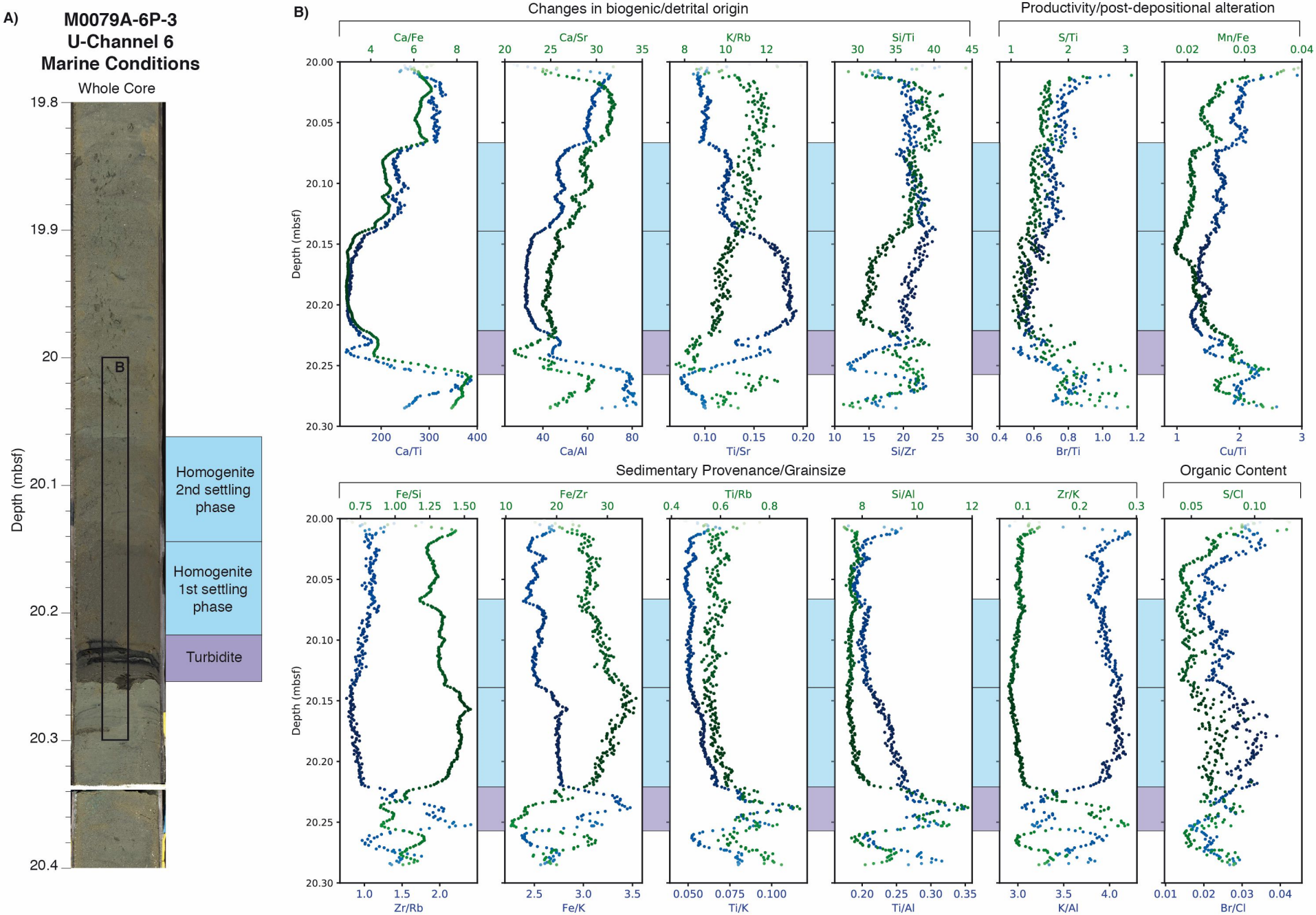
A)
M0079A-6P-3
U-Channel 6
Marine Conditions
Whole Core
Depth (mbsf)
19.8
19.9
20
20.1
20.2
20.3
20.4
B
Homogenite 2nd settling phase
Homogenite 1st settling phase
Turbidite
B)
Changes in biogenic/detrital origin
Productivity/post-depositional alteration
Ca/Fe
Ca/Sr
K/Rb
Si/Ti
S/Ti
Mn/Fe
Ca/Ti
Ca/Al
Ti/Sr
Si/Zr
Br/Ti
Cu/Ti
Sedimentary Provenance/Grainsize
Organic Content
Fe/Si
Fe/Zr
Ti/Rb
Si/Al
Zr/K
S/Cl
Zr/Rb
Fe/K
Ti/K
Ti/Al
K/Al
Br/Cl

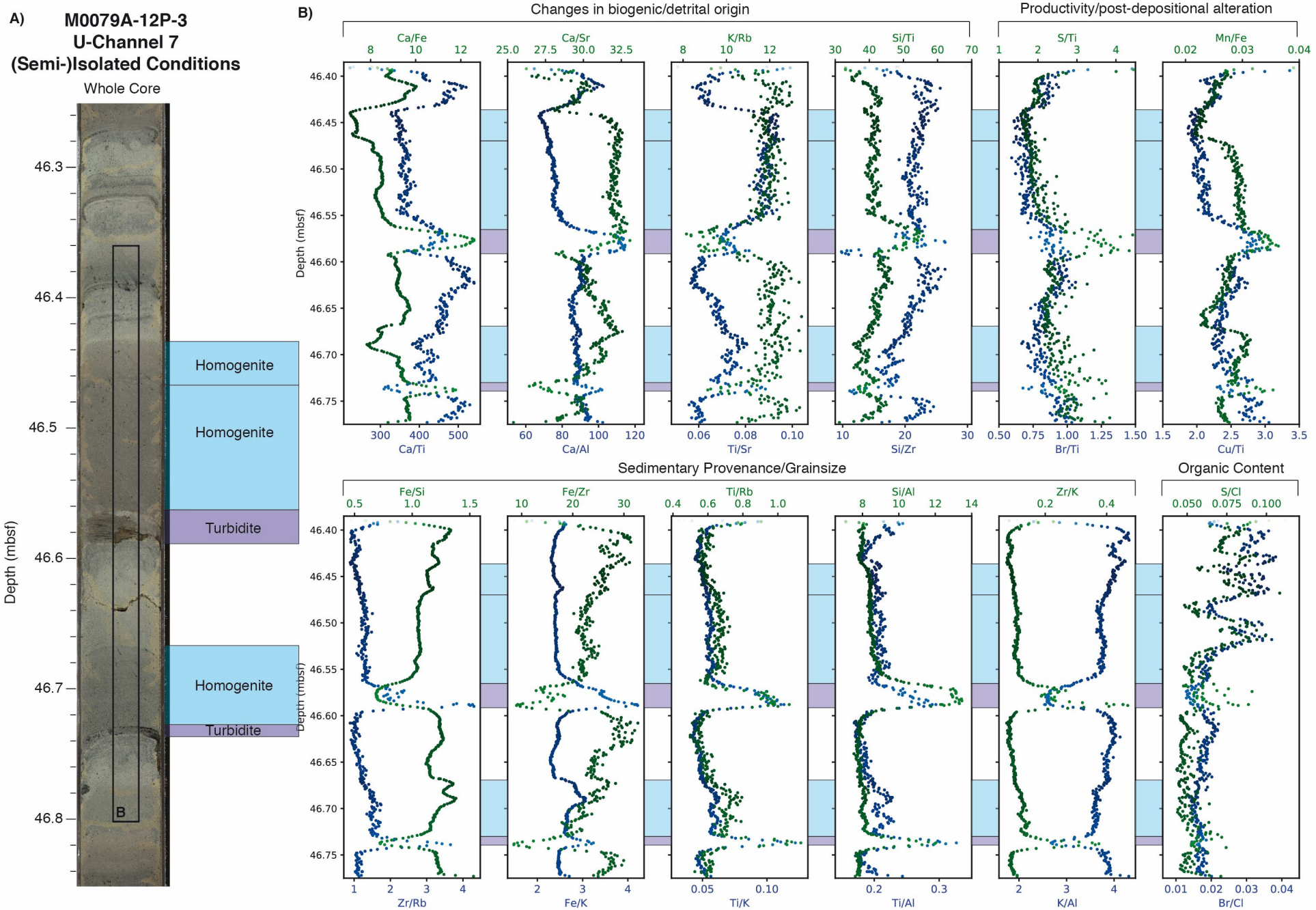
A)
M0079A-12P-3
U-Channel 7
(Semi-)Isolated Conditions
Whole Core
Depth (mbsf)
46.3
46.4
46.5
46.6
46.7
46.8
B
Homogenite
Homogenite
Turbidite
Homogenite
Turbidite
B)
Changes in biogenic/detrital origin
Productivity/post-depositional alteration
Ca/Fe
Ca/Sr
K/Rb
Si/Ti
S/Ti
Mn/Fe
Ca/Ti
Ca/Al
Ti/Sr
Si/Zr
Br/Ti
Cu/Ti
Sedimentary Provenance/Grainsize
Organic Content
Fe/Si
Fe/Zr
Ti/Rb
Si/Al
Zr/K
S/Cl
Zr/Rb
Fe/K
Ti/K
Ti/Al
K/Al
Br/Cl

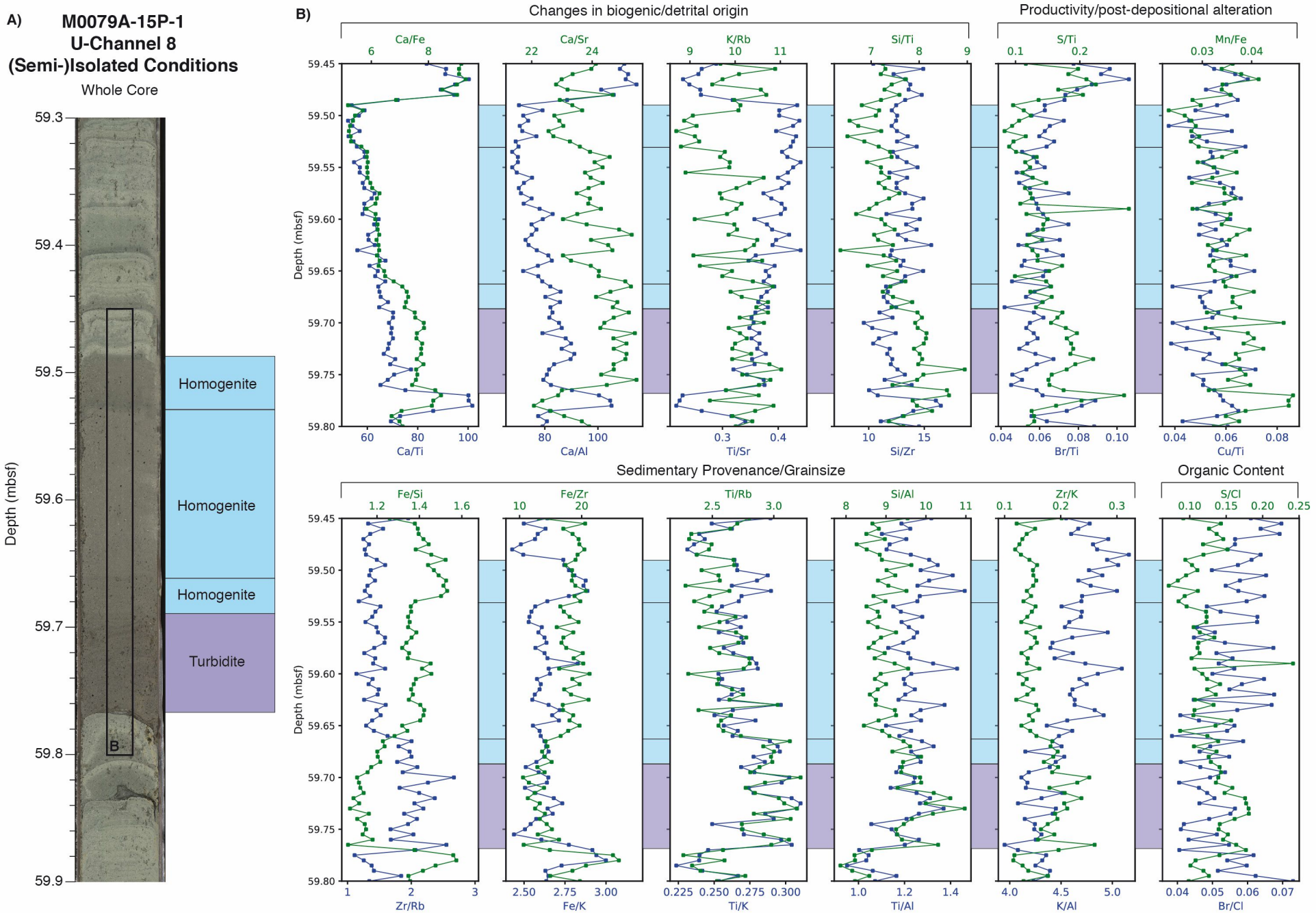
A)
M0079A-15P-1
U-Channel 8
(Semi-)Isolated Conditions
Whole Core
Depth (mbsf)
59.3
59.4
59.5
59.6
59.7
59.8
59.9
B
Homogenite
Homogenite
Homogenite
Turbidite
B)
Changes in biogenic/detrital origin
Productivity/post-depositional alteration
Ca/Fe
Ca/Sr
K/Rb
Si/Ti
S/Ti
Mn/Fe
Ca/Ti
Ca/Al
Ti/Sr
Si/Zr
Br/Ti
Cu/Ti
Sedimentary Provenance/Grainsize
Organic Content
Fe/Si
Fe/Zr
Ti/Rb
Si/Al
Zr/K
S/Cl
Zr/Rb
Fe/K
Ti/K
Ti/Al
K/Al
Br/Cl

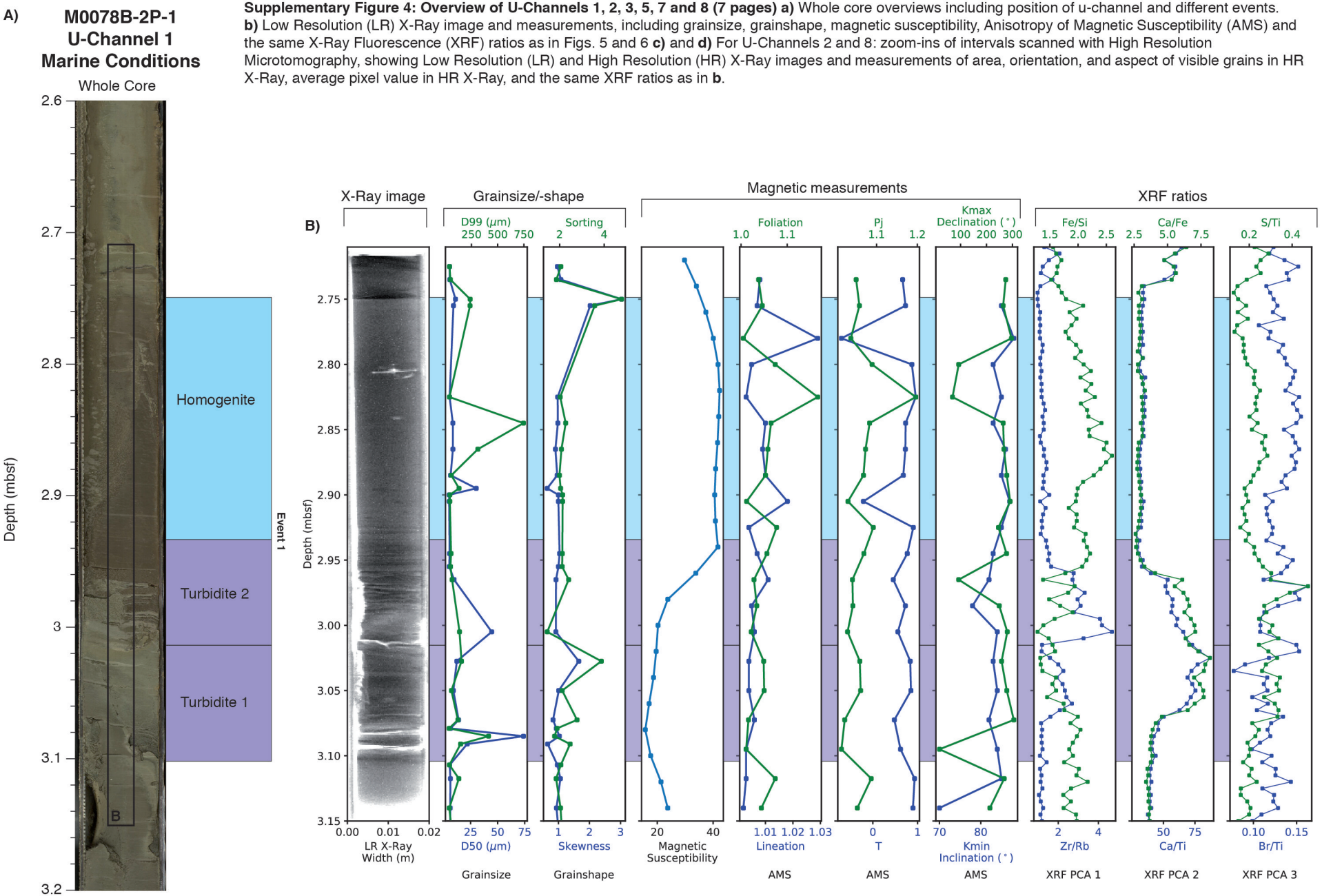

Supplementary Figure 4: Overview of U-Channels 1, 2, 3, 5, 7 and 8 (7 pages) a) Whole core overviews including position of u-channel and different events. **b)** Low Resolution (LR) X-Ray image and measurements, including grainsize, grainshape, magnetic susceptibility, Anisotropy of Magnetic Susceptibility (AMS) and the same X-Ray Fluorescence (XRF) ratios as in Figs. 5 and 6 **c)** and **d)** For U-Channels 2 and 8: zoom-ins of intervals scanned with High Resolution Microtomography, showing Low Resolution (LR) and High Resolution (HR) X-Ray images and measurements of area, orientation, and aspect of visible grains in HR X-Ray, average pixel value in HR X-Ray, and the same XRF ratios as in **b**.

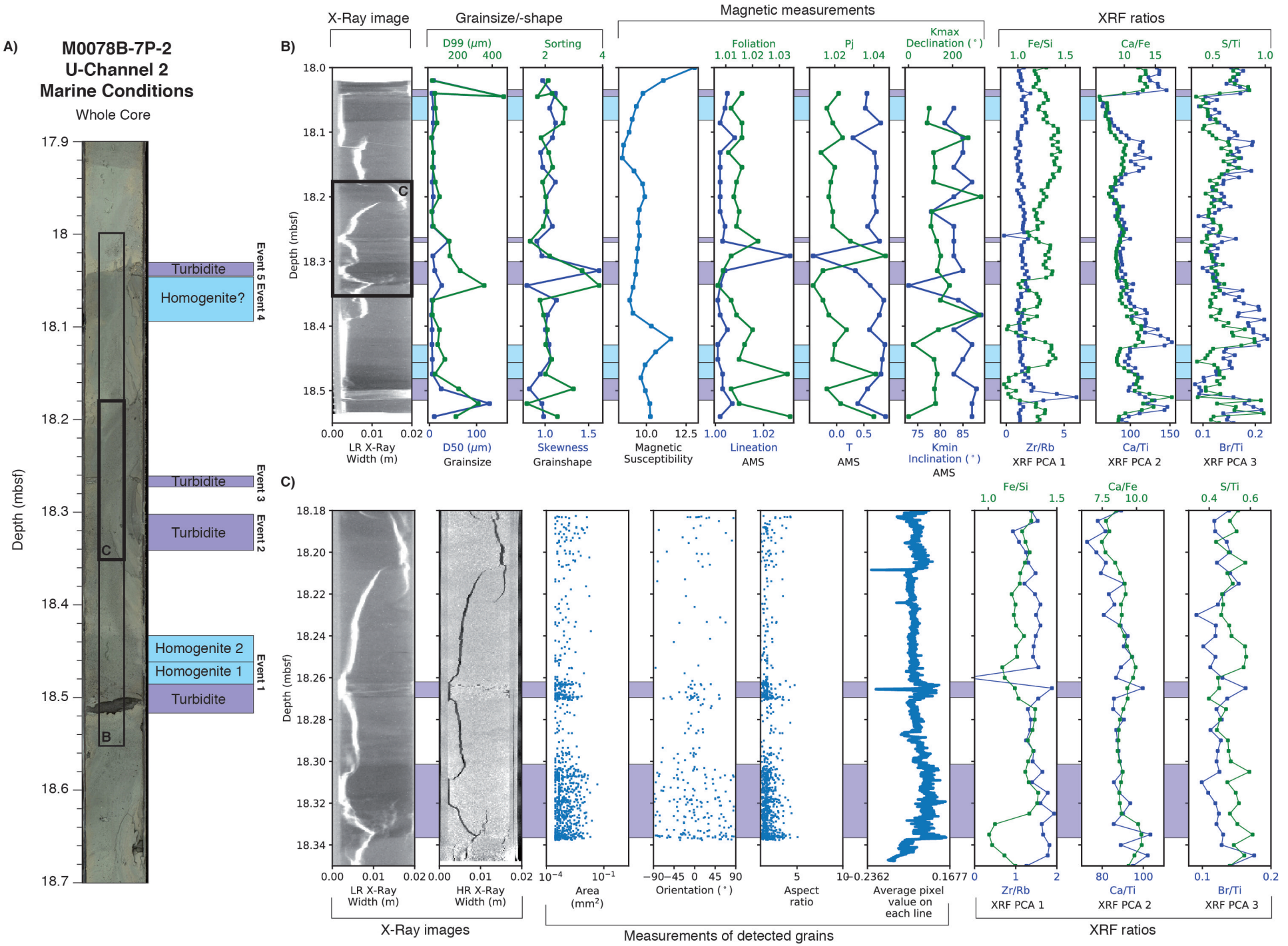
A)
M0078B-7P-2
U-Channel 2
Marine Conditions
Whole Core
Depth (mbsf)
Turbidite
Homogenite?
Event 5
Event 4
Turbidite
Event 3
Turbidite
Event 2
Homogenite 2
Homogenite 1
Turbidite
Event 1
B)
X-Ray image
Grainsize/-shape
Magnetic measurements
XRF ratios
D99 (μm)
Sorting
Foliation
Pj
Kmax Declination (°)
Fe/Si
Ca/Fe
S/Ti
LR X-Ray Width (m)
D50 (μm) Grainsize
Skewness Grainshape
Magnetic Susceptibility
Lineation AMS
T AMS
Kmin Inclination (°) AMS
Zr/Rb XRF PCA 1
Ca/Ti XRF PCA 2
Br/Ti XRF PCA 3
C)
LR X-Ray Width (m)
HR X-Ray Width (m)
Area (mm²)
Orientation (°)
Aspect ratio
Average pixel value on each line
X-Ray images
Measurements of detected grains
XRF ratios

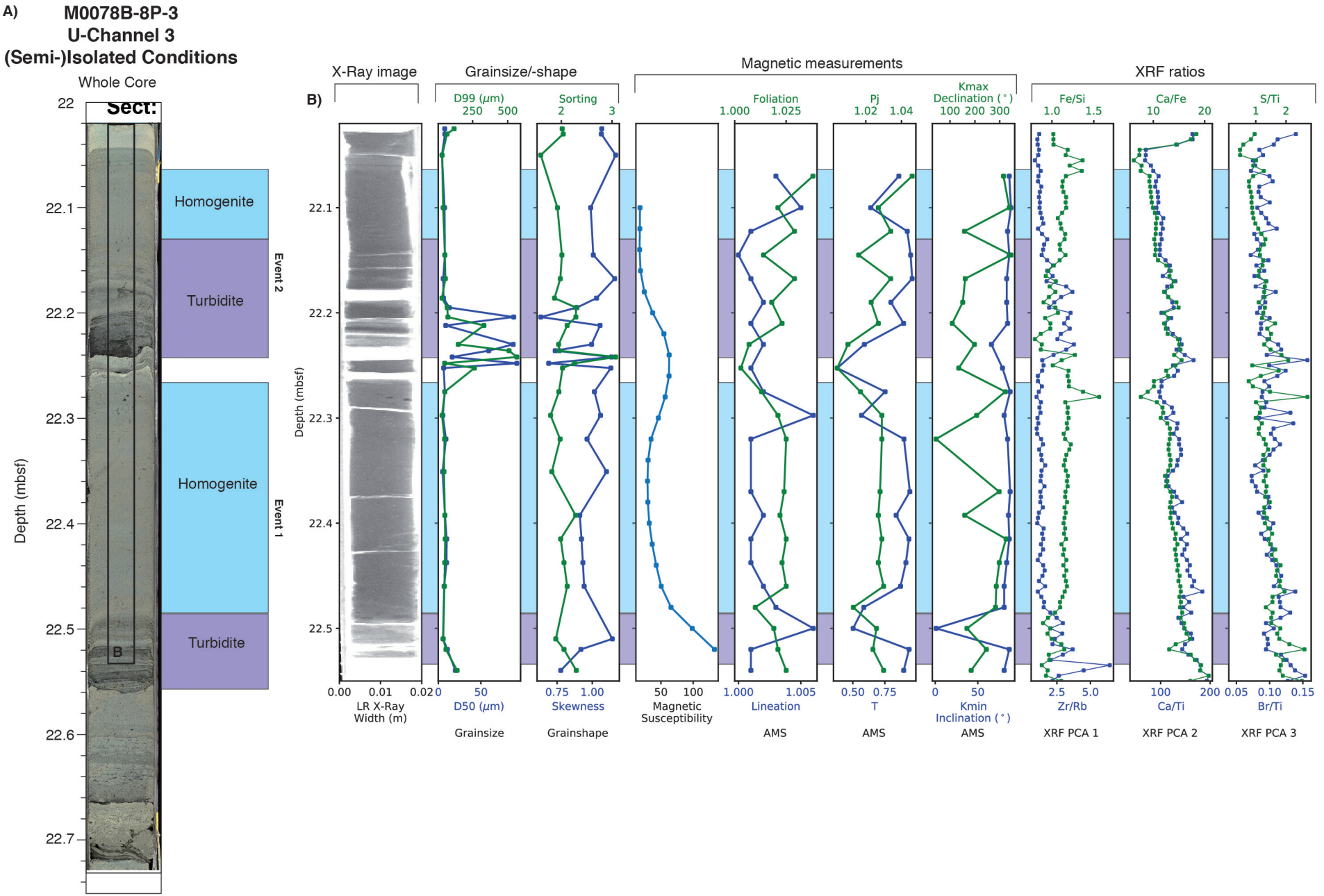
A)
M0078B-8P-3
U-Channel 3
(Semi-)Isolated Conditions
Whole Core
Depth (mbsf)
Homogenite
Turbidite
Event 2
Homogenite
Turbidite
Event 1
B
B)
X-Ray image
Grainsize/-shape
Magnetic measurements
XRF ratios
D99 (μm)
Sorting
Foliation
Pj
Kmax Declination (°)
Fe/Si
Ca/Fe
S/Ti
LR X-Ray Width (m)
D50 (μm)
Skewness
Magnetic Susceptibility
Lineation
T
Kmin Inclination (°)
Zr/Rb
Ca/Ti
Br/Ti
Grainsize
Grainshape
AMS
AMS
AMS
XRF PCA 1
XRF PCA 2
XRF PCA 3

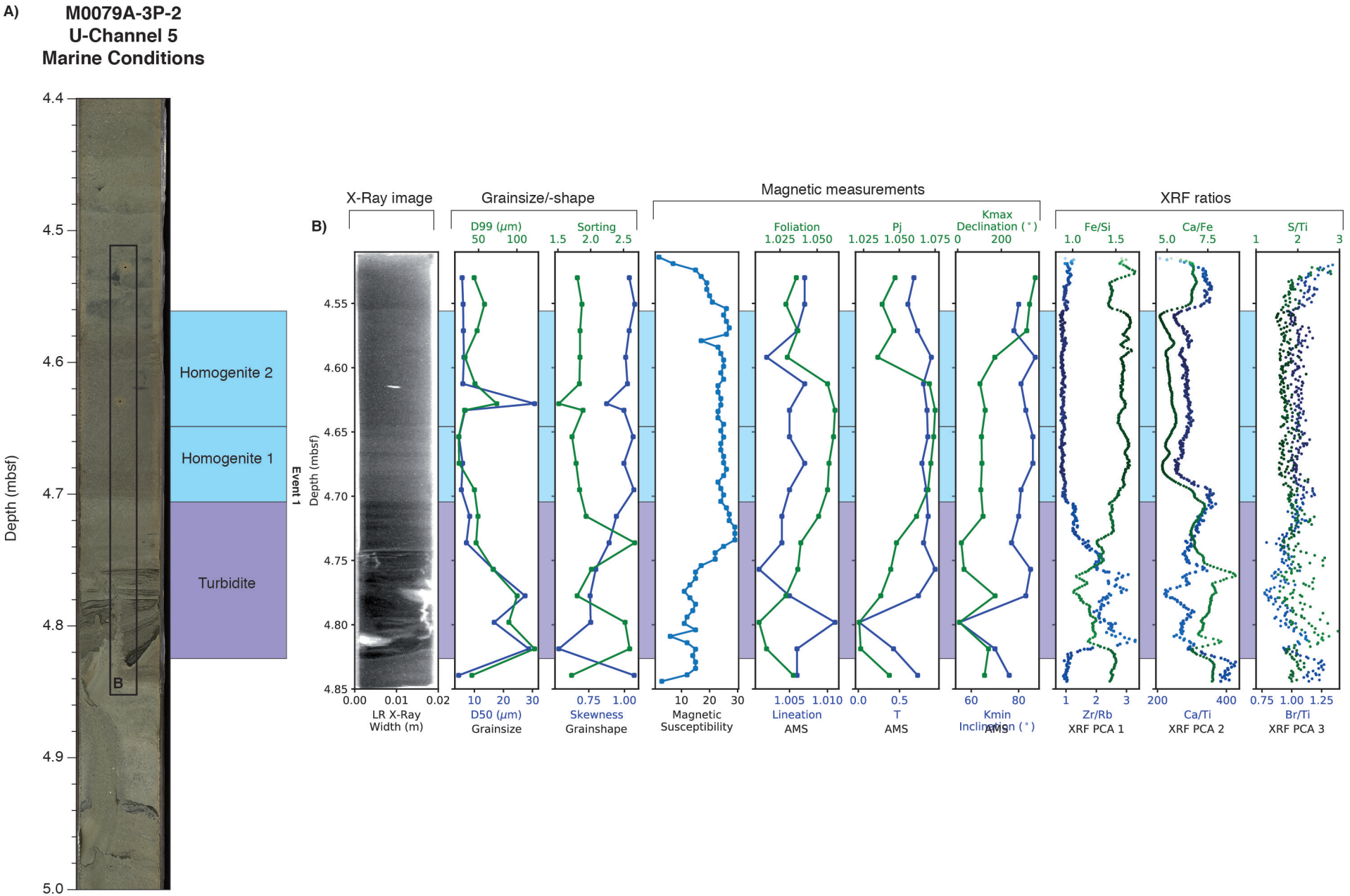
A)
M0079A-3P-2
U-Channel 5
Marine Conditions
Depth (mbsf)
4.4
4.5
4.6
4.7
4.8
4.9
5.0
Homogenite 2
Homogenite 1
Turbidite
B
Event 1
B)
X-Ray image
Grainsize/-shape
Magnetic measurements
XRF ratios
D99 (μm)
Sorting
Foliation
Pj
Kmax Declination (°)
Fe/Si
Ca/Fe
S/Ti
LR X-Ray Width (m)
D50 (μm) Grainsize
Skewness Grainshape
Magnetic Susceptibility
Lineation AMS
T AMS
Kmin Inclination (°) AMS
Zr/Rb XRF PCA 1
Ca/Ti XRF PCA 2
Br/Ti XRF PCA 3

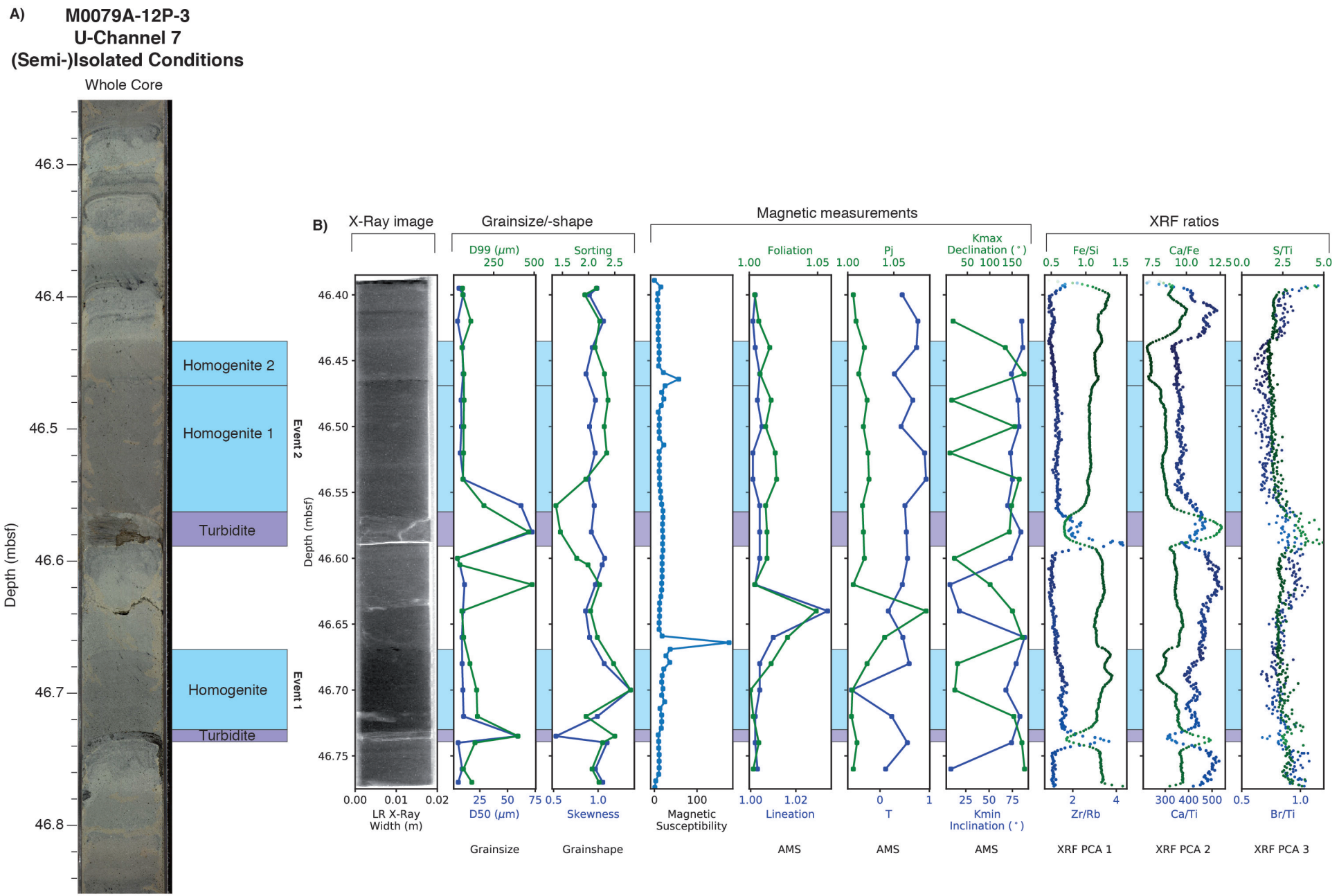
A)
M0079A-12P-3
U-Channel 7
(Semi-)Isolated Conditions
Whole Core
Depth (mbsf)
46.3
46.4
46.5
46.6
46.7
46.8
Homogenite 2
Homogenite 1
Turbidite
Homogenite
Turbidite
Event 2
Event 1
B)
X-Ray image
Grainsize/-shape
Magnetic measurements
XRF ratios
D99 (μm)
Sorting
Foliation
Pj
Kmax Declination (°)
Fe/Si
Ca/Fe
S/Ti
LR X-Ray Width (m)
D50 (μm)
Skewness
Magnetic Susceptibility
Lineation
T
Kmin Inclination (°)
Zr/Rb
Ca/Ti
Br/Ti
Grainsize
Grainshape
AMS
AMS
AMS
XRF PCA 1
XRF PCA 2
XRF PCA 3

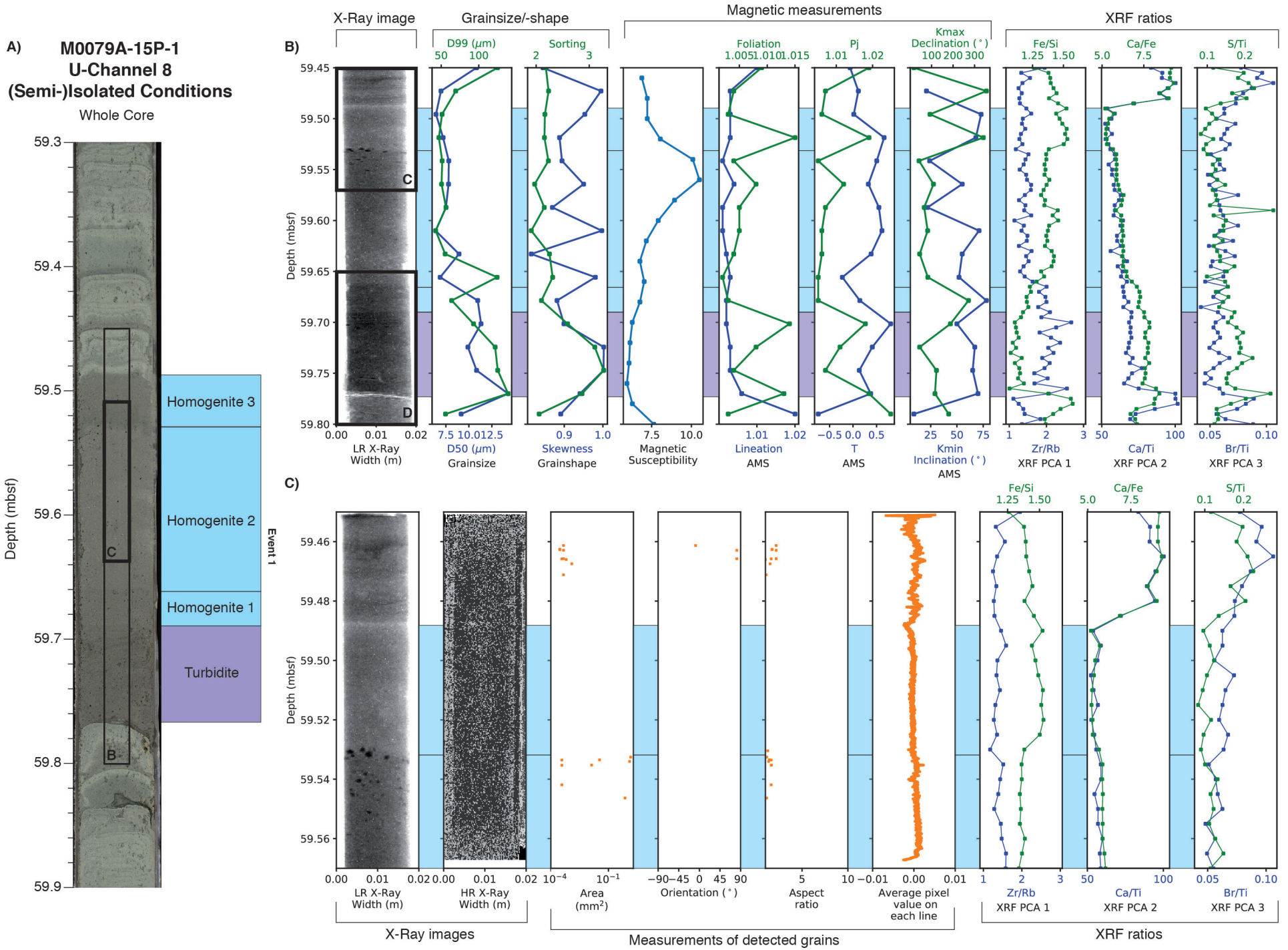
A)
M0079A-15P-1
U-Channel 8
(Semi-)Isolated Conditions
Whole Core
Depth (mbsf)
Homogenite 3
Homogenite 2
Homogenite 1
Turbidite
Event 1
B)
X-Ray image
Grainsize/-shape
Magnetic measurements
XRF ratios
D99 (μm)
Sorting
Foliation
Pj
Kmax Declination (°)
Fe/Si
Ca/Fe
S/Ti
LR X-Ray Width (m)
D50 (μm) Grainsize
Skewness Grainshape
Magnetic Susceptibility
Lineation AMS
T AMS
Kmin Inclination (°) AMS
Zr/Rb XRF PCA 1
Ca/Ti XRF PCA 2
Br/Ti XRF PCA 3
C)
LR X-Ray Width (m)
HR X-Ray Width (m)
Area (mm²)
Orientation (°)
Aspect ratio
Average pixel value on each line
X-Ray images
Measurements of detected grains
XRF ratios

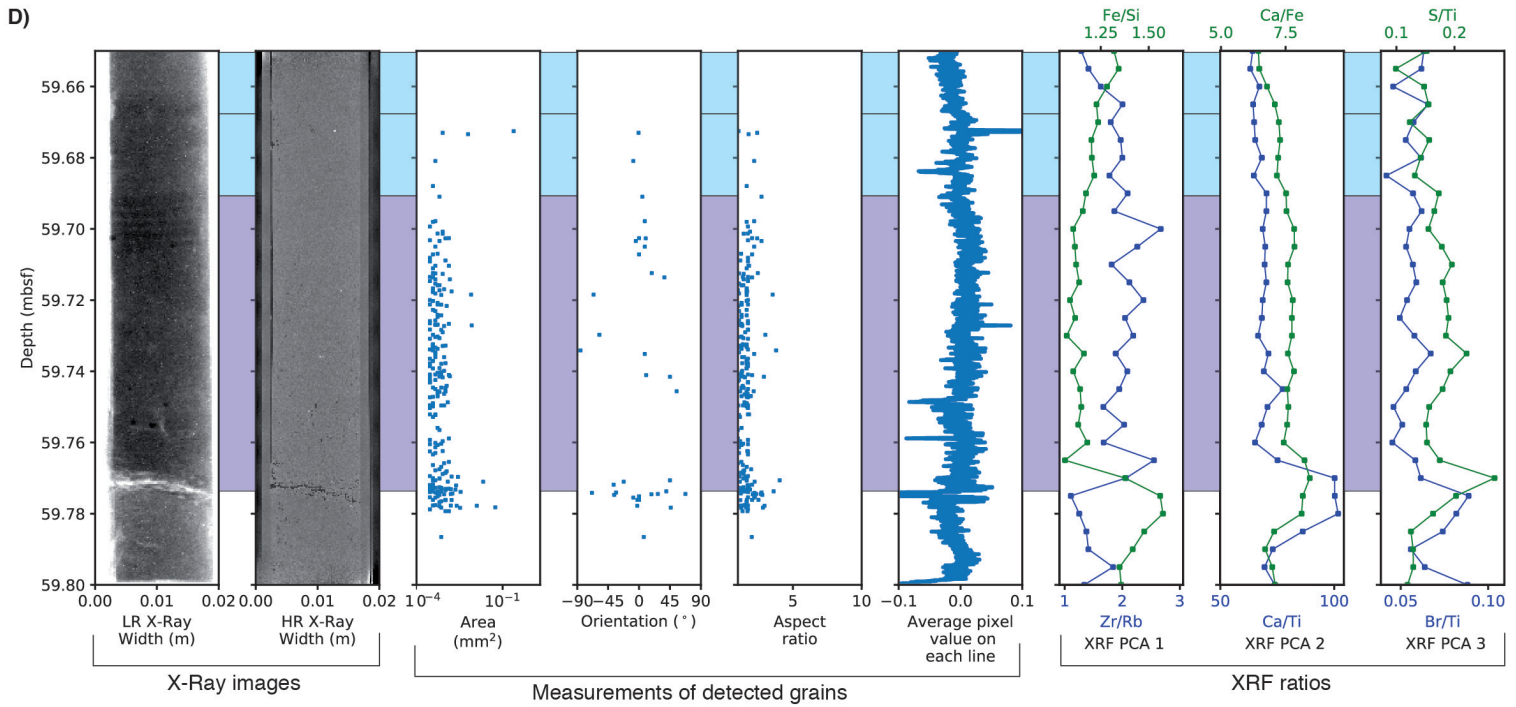
D)
Depth (mbsf)
59.66
59.68
59.70
59.72
59.74
59.76
59.78
59.80
0.00
0.01
0.02
LR X-Ray Width (m)
HR X-Ray Width (m)
10^{-4}
10^{-1}
Area (mm^2)
−90 −45 0 45 90
Orientation (°)
5
10
Aspect ratio
−0.1
0.0
0.1
Average pixel value on each line
Fe/Si
1.25
1.50
Zr/Rb
XRF PCA 1
Ca/Fe
5.0
7.5
Ca/Ti
XRF PCA 2
S/Ti
0.1
0.2
Br/Ti
XRF PCA 3
X-Ray images
Measurements of detected grains
XRF ratios

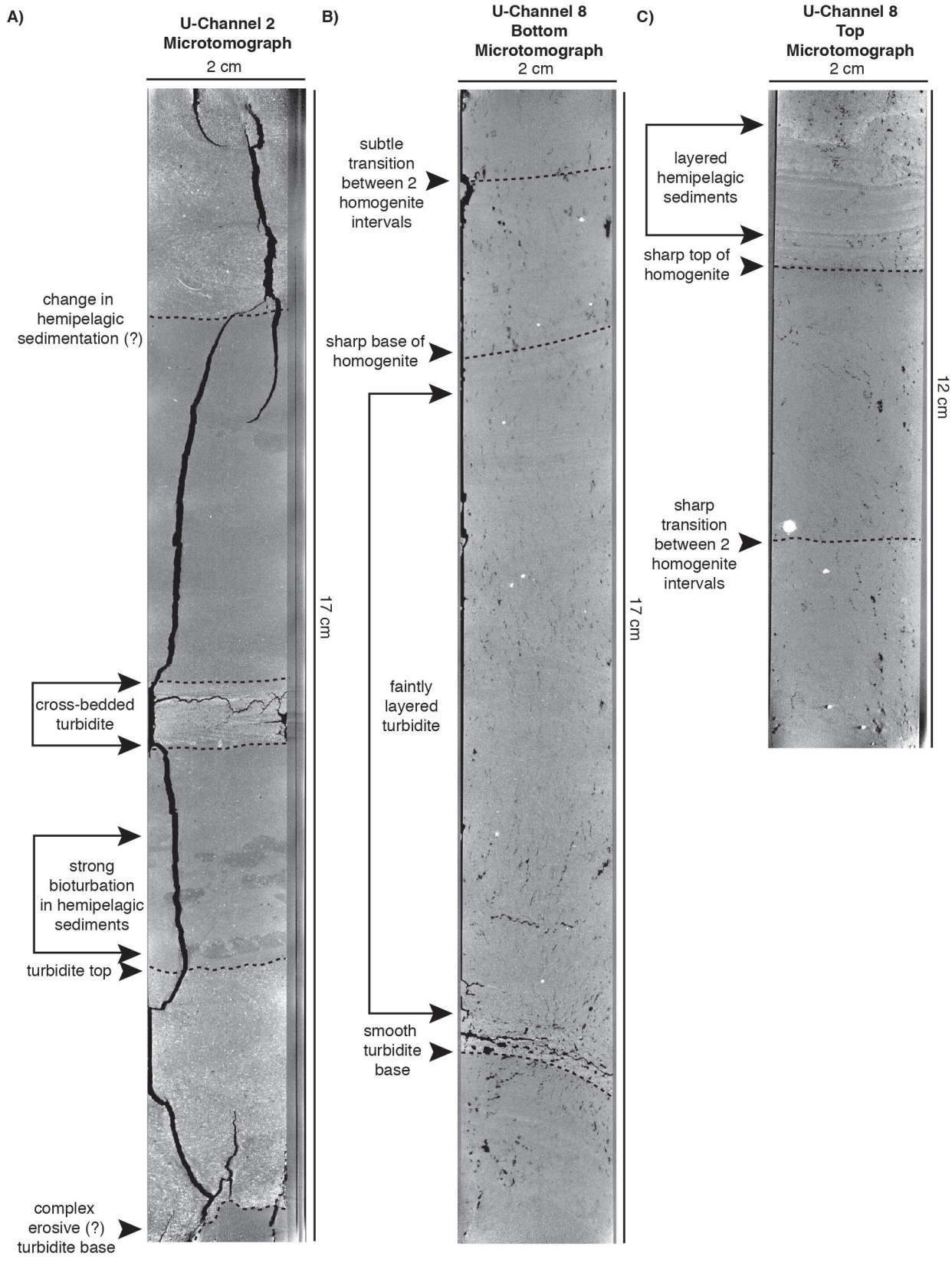

Supplementary Figure 5: X-Ray Microtomography examples for U-Channels 2 and 8. See positions in Sup. Fig. 3 **a)** 2D image of sedimentary events in U-Channel 2 **b)** 2D image of bottom of U-Channel 8 **c)** 2D images of top of U-Channel 8.

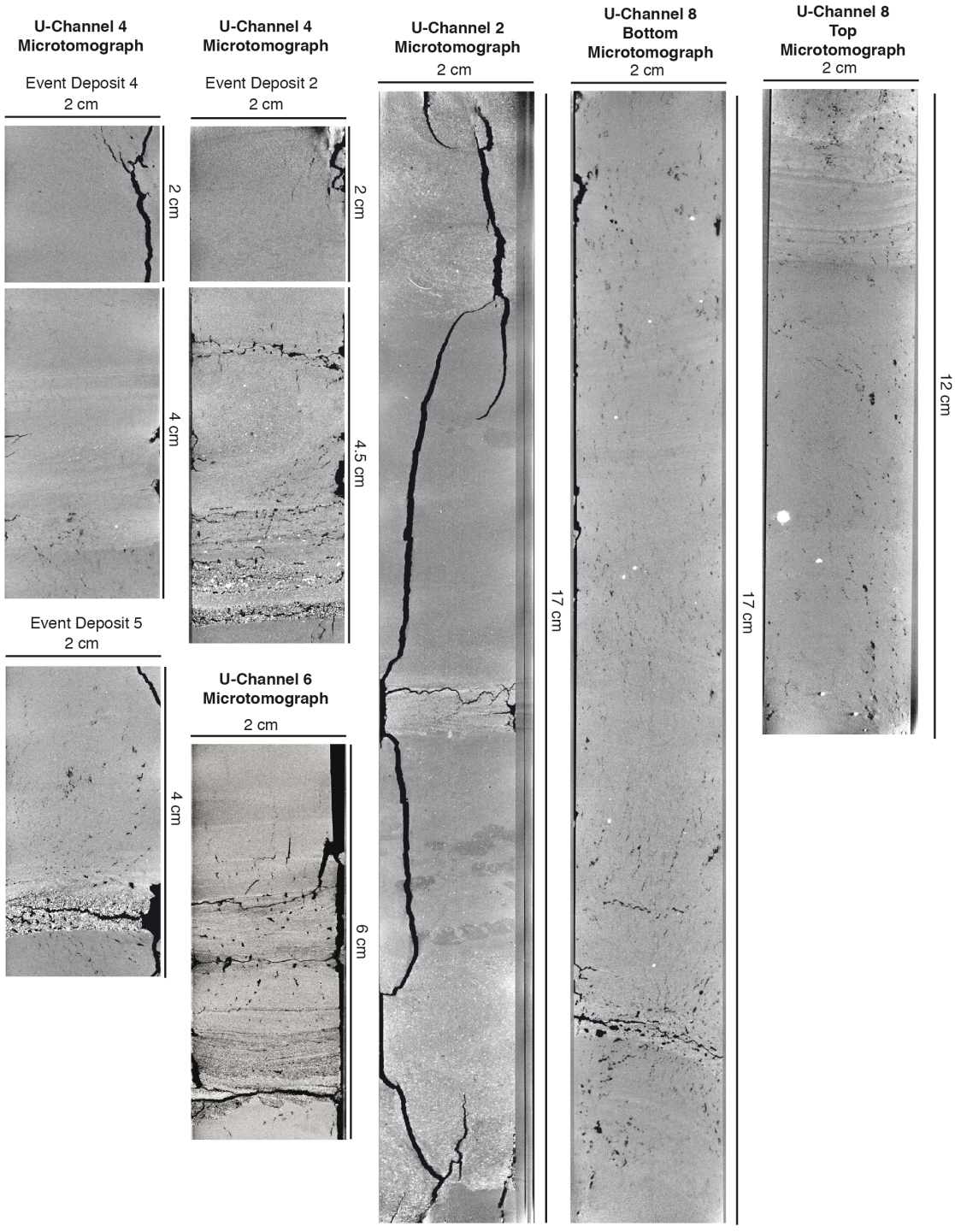

Supplementary Figure 6: X-Ray Microtomography images without interpretation. For interpretation of these images, see Figure 8 and Supplementary Figure 5.

Supplementary Table 1: Overview of sedimentary events in U-Channels. Describing observations on grainsize/-shape, (anisotropy of) magnetic susceptibility, X-Ray Fluorescence ratios, X-Ray images and an overall interpretation of the sedimentary event in relation to the proposed types (Fig. 2)

U-Channel	Event	Size (mm)	Grainsize/-shape	AMS/Mag. Sus	XRF	X-ray tomography	Interpretation
UC-1 (mar)	1 (Tu1+ Tu2+ Hm)	352	Two major fining upwards pulses in Tu, similar grainsize Hm and hemipelagic deposits	Higher Magnetic Susceptibility, average AMS foliation and corrected anisotropy degree Pj in Hm	Higher Zr/Rb in Tu, especially Tu2, also higher Ca/Ti and Ca/Fe in Tu's, increasing within Tu1 and decreasing within Tu2. Low Ca/Fe and Ca/Ti in Hm	Low-resolution only. Irregular Tu base, clear layering within Tu's. Sharp boundary between Tu and Hm, faint layering in lowermost part of Hm. Sharp boundary Hm and overlying hemipelagite.	Complex TuHm sedimentary event with multiple turbiditic pulses. Possibly of seismic origin
UC-2 (mar)	1 (Tu+ Hm1+ Hm2)	80	Fining upwards Tu, too small event for details	Higher Magnetic Susceptibility, average AMS foliation and corrected anisotropy degree Pj in Hm	Higher Zr/Rb in Tu, lower Ca/Fe, Ca/Ti and higher Fe/Si in Hm's, especially Hm2. S/Ti and Br/Ti low in both Tu and Hm	Sharp but very irregular Tu base, sharp transitions from Tu to Hm1, Hm1 to Hm2 and Hm2 to - overlying hemipelagite	Complex TuHm sedimentary event with two Hm settling phases, possibly of seismic origin
	2 (Tu)	40	Fining upwards Tu, too small event for details	Low AMS foliation and corrected anisotropy degree Pj	Strong increase in Fe/Si at base of Tu, gradual decrease in Ca/Ti and Ca/Fe upwards	Irregular, erosive Tu base, no clear layering within Tu and sharp top of Tu	Small 'classic' turbidite of unknown origin
	3 (Tu)	12	Relatively high grainsize compared to hemipelagic deposits	High AMS foliation	Small peak in Br/Ti and Ca/Ti	Relatively smooth Tu base, cross-bedded layering within Tu	Small 'classic' turbidite of unknown origin
	4 (Hm)	50	Similar grainsize to hemipelagic deposits	No clear trends	Low Ca/Fe and Ca/Ti ratios	Sharp transitions at both bottom and top, with possibly a thin, darker (coarser?) layer at the bottom of Hm	Homogenite with possibly a small silt turbidite at base. Cut off at the top by overlying turbidite. Possibly of seismic origin
	5 (Tu)	14	Relatively high grainsize compared to hemipelagic deposits	No clear trends	Sharp changes in Ca/Fe, Ca/Ti, S/Ti and Br/Ti ratios between underlying and overlying deposits	Too thin for observations on low-resolution X-ray tomography	Small 'classic' turbidite, associated with a change in hemipelagic sedimentation, possibly changing environmental conditions
UC-3 (ISI)	1 (Tu+ Hm)	295	Fining upwards Tu, uniform grainsize throughout Hm	Peaks in Magnetic Susceptibility and AMS lineation at both Tu and top of Hm	Peak in Zr/Rb at base of Tu, peaks in Fe/Si and S/Ti at top of Hm. Ca/Ti and Ca/Fe gradually decreasing upwards in Tu and Hm	Strong layering within Tu, faint layering in Hm. Big grains near the top of the Hm. Sharp limit between Tu and Hm	TuHm sedimentary event, possibly of seismic origin. Grains near top probably result from post-depositional alteration.
	2 (Tu+ Hm)	175	Strongly fluctuating at base of Tu, uniformly small grainsize at top	Within Tu/Hm, general decrease in in Magnetic Susceptibility upwards	Peak in Zr/Rb at base of Tu, peak in Fe/Si at top of Hm. Ca/Ti and Ca/Fe irregularly decreasing	Strong layering within Tu, faint layering in Hm.	TuHm sedimentary event, possibly of seismic origin.

			of Tu and Hm	and increase in AMS foliation, lineation, Pj and T	upwards in Tu and gradually decreasing upwards in Hm		
UC-4 (ISI)	1 (Tu)	27	Not sufficient data	Not sufficient data	Relatively low Ca/Fe and Ca/Ti, decreasing upwards Zr/Rb and increasing upwards Fe/Si, Br/Ti and S/Ti	Sharp transition between Tu and overlying Hemipelagic sediments	Small 'classic' turbidite of unknown origin
	2 (Tu+ Hm1+ Hm2)	94	Few data, but larger grainsize in Tu	Higher Magnetic Susceptibility in Tu, peak in AMS foliation and corrected anisotropy degree Pj in Hm's	Relatively low Ca/Fe, Ca/Ti, Br/Ti and S/Ti in Tu/Hm event. Two peaks within Tu for Fe/Si and Zr/Rb	Microfractured base of Tu, and several microfractures within ~4 turbiditic pulses near the base, neat base of Hm and sharp transition to upper Hm. Diffuse (bioturbated) top of Hm.	Complex TuHm sedimentary event of seismic origin. Microfractures at Tu base and two settling phases for Hm1 and Hm2
	3 (Tu+ Hm)	25	Not sufficient data	Not sufficient data	Gradual decrease in Zr/Rb within Tu/Hm, sharp increase in Ca/Ti at Hm-Hemipelagic transition	Sharp base of Tu and diffuse top of Hm.	TuHm sedimentary event possibly of seismic origin.
	4 (Tu+ Hm1+ Hm2)	40	Few data, but larger grainsize in Tu	Higher Magnetic Susceptibility in Tu, peak in AMS foliation and corrected anisotropy degree Pj in Hm's	Relatively low Ca/Fe, Ca/Ti, Br/Ti and S/Ti in Tu/Hm event. Zr/Rb decreasing and Fe/Si increasing upwards within Tu.	Microfractured base of Tu, faint layering within Tu and a neat base of Hm. Diffuse (bioturbated) top of Hm.	Complex TuHm sedimentary event of seismic origin. Microfractures at Tu base and two settling phases for Hm1 and Hm2
	5 (Tu)	55	Few data, but larger grainsize at base of Tu	Relatively high Magnetic Susceptibility, peak near top of Tu. Relatively high AMS lineation and low foliation, T and Pj	Overall increase in Fe/Si and decrease in Ca/Ti, Ca/Fe and Zr/Rb upwards. Br/Ti and S/Ti decrease upwards at base of Tu, peak in S/Ti near the top of Tu.	Smooth Tu base, well-sorted in the basal interval below fainter Tu layering. Big grains near the top of the Hm.	'Classic' turbidite of unknown origin. Grains near top probably result from post-depositional alteration.
UC-5 (mar)	1 (Tu+ Hm1+ Hm2)	280	Fining upwards Tu, similar grainsize Hm and hemipelagic deposits	Higher Magnetic Susceptibility, AMS foliation and corrected anisotropy degree Pj in Hm's, both slightly lower in Hm2 than Hm1	Higher Zr/Rb, lower Fe/Si in Tu, lower Ca/Ti, Ca/Fe, Br/Ti and S/Ti in Hm's, slightly more variable in Hm1 than Hm2	Non-horizontal, sharp turbidite base. Clear layering in turbidite and faint layering in Hm1. Bioturbated top of Hm2.	Complex TuHm sedimentary event, possibly of seismic origin, with two settling phases for Hm1 and Hm2
UC-6 (mar)	1 (Tu+ Hm1+ Hm2)	193	Fining upwards Tu, similar grainsize Hm2 and hemipelagic deposits, slightly more variable in Hm1	Higher Magnetic Susceptibility, AMS foliation and corrected anisotropy degree Pj in Hm's, both slightly lower in Hm2 than Hm1	Higher Zr/Rb, lower Fe/Si in Tu, lower Ca/Ti, Ca/Fe, Br/Ti and S/Ti in Hm's, slightly higher in Hm2 than Hm1	Tu erosive base displays both rounded zones and linear features. Within several coarse turbiditic pulses, complex microprogradations and microfractures. Sharp limit between Tu and Hm1, and between Hm1 and Hm2.	Complex TuHm sedimentary event of seismic origin. Evidence of liquefaction and microfractures at Tu base, to-and fro-displacements and coeval shaking within Tu, and two settling phases for Hm1 and Hm2
UC-7 (ISI)	1 (Tu+ Hm)	70	Few data, but larger grainsize at base of Tu	Peak in Magnetic Susceptibility at top of	Higher Zr/Rb and Ca/Fe + lower Fe/Si and Ca/Ti in Tu, Upwards	Sharp Tu base and transition to Hm. Top of Hm contains big	Tu/Hm sedimentary event, possibly of seismic origin. Grains

			and smaller grainsize Hm's and hemipelagic deposits	Hm	increasing Fe/Si and upwards decreasing Ca/Fe in Hm.	grains around transition to hemipelagic sediments.	near top probably result from post-depositional alteration.
	2 (Tu+ Hm1+ Hm2)	160	Few data, but larger grainsize at base of Tu and smaller grainsize Hm's and hemipelagic deposits	Peak in Magnetic Susceptibility at the Hm1 to Hm2 transition	Higher Zr/Rb, Ca/Fe, Ca/Ti S/Ti and Br/Ti + lower Fe/Si in Tu. Relatively low Ca/Fe and Ca/Ti in Hm's, lower in Hm2 than Hm1.	Sharp Tu base and transitions Tu-Hm1 and Hm1-Hm2. Clear layering in Tu, faint layering in Hm1 and. Big grains around Hm1-Hm2 sediments. Bioturbated top of Hm2.	Tu/Hm sedimentary event, possibly of seismic origin, with two settling phases for Hm1 and Hm2. Grains near Hm1-Hm2 transition probably result from post-depositional alteration.
UC-8 (ISI)	1 (Tu+ Hm1+ Hm2+ Hm3)	280	Few data, but generally fining upwards within Tu/Hm sedimentary event	Peak in Magnetic Susceptibility near top of Hm2. Relatively high AMS foliation and corrected anisotropy degree Pj in Tu and Hm3	Relatively high Zr/Rb and low Fe/Si in Tu. Sharp increases in Fe/Si and decreases in Ca/Fe upwards for Hm1-Hm2 and Hm2-Hm3 transitions. Overall lower S/Ti and Br/Ti within Tu/Hm compared to hemipelagic sediments.	Smooth turbidite base and faint layering within turbidite. Sharp base of Hm1 and more subtle transitions between Hm1-Hm2 and Hm2-Hm3. Big grains around Hm2-Hm3 transition. Sharp top of Hm3 and clear contrast with layered hemipelagic sediments.	Tu/Hm sedimentary event, possibly of seismic origin, with three settling phases for Hm1, Hm2 and Hm3. Grains near Hm2-Hm3 transition probably result from post-depositional alteration.